

University of New Mexico

## UNM Digital Repository

---

Mechanical Engineering ETDs

Engineering ETDs

---

Summer 7-15-2022

### FIESTA and Shock-Driven Flows

Brian E. Romero

*University of New Mexico - Main Campus*

Follow this and additional works at: [https://digitalrepository.unm.edu/me\\_etds](https://digitalrepository.unm.edu/me_etds)



Part of the [Fluid Dynamics Commons](#), [Mechanical Engineering Commons](#), and the [Numerical Analysis and Scientific Computing Commons](#)

---

#### Recommended Citation

Romero, Brian E.. "FIESTA and Shock-Driven Flows." (2022). [https://digitalrepository.unm.edu/me\\_etds/199](https://digitalrepository.unm.edu/me_etds/199)

This Dissertation is brought to you for free and open access by the Engineering ETDs at UNM Digital Repository. It has been accepted for inclusion in Mechanical Engineering ETDs by an authorized administrator of UNM Digital Repository. For more information, please contact [disc@unm.edu](mailto:disc@unm.edu).



# FIESTA and Shock-Driven Flows

by

**Brian Estevan Romero**

B.S., Mechanical Engineering,  
University of New Mexico, 2016

DISSERTATION

Submitted in Partial Fulfillment of the  
Requirements for the Degree of

Doctor of Philosophy  
Engineering

The University of New Mexico

Albuquerque, New Mexico

July, 2022

# Dedication

*To my mother and father.*

# Acknowledgments

This work is partially supported by subcontract 594693 “Development of a hydrodynamic code for large-scale atmospheric event simulations on modern and future computational platform” from Los Alamos National Laboratory to the University of New Mexico, DTRA grant HDTRA-18-1-0022, the New Mexico Consortium, and the New Mexico Space Grant Consortium, National Aeronautics and Space Administration Cooperative Agreement Number 80NSSC20M0034.

Computational resources were provided by the Los Alamos National Laboratory Institutional Computing Program supported by the U.S. Department of Energy National Nuclear Security Administration under contract No. 89233218CNA000001, by the UNM Center for Advanced Research Computing, supported in part by the National Science Foundation, and by NNSA under the Predictive Science Academic Alliance Program, award #DE-NA00003966.

# FIESTA and Shock-Driven Flows

by

**Brian Estevan Romero**

B.S., Mechanical Engineering,  
University of New Mexico, 2016

Ph.D., Engineering (Mechanical), University of New Mexico, 2022

## **Abstract**

In this study, the interaction of a shock with various gas and particle interfaces is analyzed through simulations using a new, GPU capable, multi-species flow solver, FIESTA (Fast, Interface Evolution, Shocks, and Transport in the Atmosphere), developed for this research. The cases studied include the interaction between a shock and i) a two-dimensional (2D), circular cloud of a dense gas; ii) a 2D curtain of a dense gas; iii) a three-dimensional (3D) cylinder of a dense gas, and iv) a 3D curtain of solid particles.

In simulations of a 2D gas curtain and a 3D gas column, the curtain and column were inclined with respect to the shock. In such flow geometries a shock-driven Kelvin-Helmholtz instability (SDKHI) develops on the curtain/column surface as observed in experiments. Additionally a perturbation develops near the foot and head of the curtain/column. In this study, these phenomena, observed in experiments, are confirmed numerically for the first time.

Using simulation data, the effects of varying Mach number, initial angle and curtain/column width are explored in detail for 2D flows with inclined curtains and

3D flows with inclined columns. This work also examines the effect of SDKHI on various mixing characteristics for 3D flows with an inclined column. FIESTA is then extended to include Lagrangian particle transport capabilities and the particle mechanism is validated against experimental data.

Performance characteristics of FIESTA are also compared on several computational platforms utilizing CPU and GPU architectures. Exceptional performance is demonstrated on GPU clusters with speedups over  $77\times$ .

# Contents

<b>List of Figures</b>	<b>xi</b>
<b>List of Tables</b>	<b>xvii</b>
<b>Glossary</b>	<b>xviii</b>
<b>1 Introduction</b>	<b>1</b>
1.1 Background . . . . .	1
1.2 Objectives . . . . .	6
<b>2 FIESTA</b>	<b>8</b>
2.1 Code Description . . . . .	8
2.2 FIESTA Capabilities . . . . .	9
2.2.1 2D Genaralized Coordinates. . . . .	10
2.2.2 3D Terrain Following Coordinates . . . . .	11
2.2.3 2D Buoyant Plume . . . . .	11

## Contents

2.2.4	2D Particle Extension . . . . .	12
2.3	FIESTA Verification . . . . .	13
2.4	FIESTA Performance . . . . .	15
<b>3</b>	<b>Reference Data</b>	<b>16</b>
<b>4</b>	<b>2D SDKHI Cases</b>	<b>21</b>
4.1	Introduction . . . . .	21
4.2	2D Governing Equations . . . . .	22
4.3	2D Circular Gas Cloud . . . . .	26
4.3.1	Simulation Setup . . . . .	26
4.3.2	Results . . . . .	28
4.4	2D Gas Curtain . . . . .	29
4.4.1	Simulation Setup . . . . .	29
4.4.2	Results . . . . .	32
4.5	Conclusions . . . . .	41
<b>5</b>	<b>3D SDKHI Cases</b>	<b>44</b>
5.1	Introduction . . . . .	44
5.2	Inviscid Simulations . . . . .	45
5.2.1	Numerical Setup . . . . .	45
5.2.2	Domain and Discretization . . . . .	47

## Contents

5.2.3	Initial Conditions . . . . .	48
5.2.4	Boundary Conditions . . . . .	49
5.2.5	Results . . . . .	50
5.2.6	Conclusions . . . . .	54
5.3	Viscous Simulation . . . . .	55
5.3.1	Numerical Setup . . . . .	55
5.3.2	Domain and Discretization . . . . .	58
5.3.3	Initial Conditions . . . . .	59
5.3.4	Boundary Conditions . . . . .	60
5.3.5	Results . . . . .	61
5.3.6	Conclusions . . . . .	70
<b>6</b>	<b>The FIESTA Particle Extension</b>	<b>71</b>
6.1	Introduction . . . . .	71
6.2	Numerical Setup . . . . .	73
6.2.1	Domain . . . . .	73
6.2.2	Spatial and Temporal Discretization . . . . .	74
6.2.3	Initial Conditions . . . . .	74
6.3	Governing Equations . . . . .	76
6.3.1	Fluid Phase Euler Solver . . . . .	76
6.3.2	Particle Phase Lagrangian Solver . . . . .	78

*Contents*

6.4	Code Description . . . . .	80
6.5	Validation Results . . . . .	80
6.6	Computational Performance . . . . .	82
6.7	Conclusions . . . . .	84
<b>7</b>	<b>Conclusions</b>	<b>85</b>

# List of Figures

1.1	Orientation of the centerline and vertical planes in relation to the shock and inclined gas column before interaction. . . . .	6
2.1	2D idealized expansion over a corrugated surface. . . . .	10
2.2	3D idealized expansion over terrain. . . . .	11
2.3	2D rising plume. . . . .	12
2.4	Idealized expansion in a particle laden gas. . . . .	13
2.5	Comparison of simulation data with the analytical solution of a 1D Sod problem. . . . .	14
2.6	Speedups for a $512^3$ ideal expansion problem on various devices. . .	15
3.1	The experimental setup for studies of shock interaction with an inclined cylindrical density interface as in Olmstead et al. (2017a,b). .	17

*List of Figures*

3.2	Representative experimental image sequence showing shock acceleration of a gas cylinder at a tilt angle $\alpha_1 = 20^\circ$ , $M = 2$ , $A = 0.6$ (Olmstead et al., 2017a). $\tau$ is dimensionless time (refer to text). The top image for each $\tau$ shows the centerline plane, the bottom image – the vertical plane. Figure reproduced from Olmstead et al. (2017a) with the permission from the authors. . . . .	18
3.3	Mach 2.0, $\alpha_1 = 30^\circ$ . Figure reproduced from Olmstead et al. (2017b) with the permission from the authors. . . . .	19
3.4	Shock-driven Kelvin-Helmholtz instability. Figure reproduced from Olmstead et al. (2017b) with the permission from the authors. . . .	20
4.1	Plot comparing the experimental $\text{SF}_6$ concentration across the gas cloud and curtain with the distribution used in simulations. . . . .	26
4.2	Dimensions and boundary conditions for the circular gas cloud simulations. . . . .	27
4.3	Computational grid (every eighth gridline shown) at $\tau = 0$ for the shock as it passes through a circular gas cloud . . . . .	27
4.4	Initial conditions used in the simulation of a shock passing through a circular gas cloud. . . . .	28
4.5	Interaction of a shock with a gas cloud at different times. . . . .	30
4.6	Normalized cloud width over time compared to experiment. . . . .	31
4.7	Dimensions and boundary conditions for gas curtain simulations. . .	31
4.8	Computational grid (every eighth gridline shown) at $\tau = 0$ for the shock as it passes through an inclined gas curtain. . . . .	32

*List of Figures*

4.9	Initial conditions used in the simulation of a shock passing through an inclined gas curtain. . . . .	33
4.10	Gas curtain concentration at various $\tau$ with density plots at $y = 0.25L_x$ and $y = 0.75L_x$ . . . . .	35
4.11	Vorticity field at different times with respect to 2D gas curtain evolution. . . . .	36
4.12	Diagram showing the location of (a) The Kelvin-Helmholtz wavelength and (b) the curtain foot wavelength. . . . .	37
4.13	Instability wavelength with respect to initial curtain angle for (a) the Kelvin-Helmholtz instability and (b) the instability at the foot of the curtain . . . . .	37
4.14	Ratio of the wavelength ( $\lambda$ ) to the initial column width ( $\delta_1$ ) with respect to Mach number for (a) the Kelvin-Helmholtz instability and (b) the perturbation at the foot of the curtain. Experimental data in (a) is from Olmstead et al. (2017b). . . . .	39
4.15	Bounding box showing perturbed curtain width at various times for the curtain simulation at $M_1 = 2.0$ , $\alpha_1 = 30^\circ$ : a) the initial uncompressed curtain, b) the compressed curtain after the shock passage, c) perturbations on the curtain surface. . . . .	40
4.16	SDKHI-induced perturbation width over time for various Mach numbers. . . . .	40
4.17	Instability wavelength with respect to initial curtain width for (a) the Kelvin-Helmholtz instability and (b) the instability at the foot of the curtain. . . . .	42

*List of Figures*

4.18	Instability width over time for various initial curtain widths. . . . .	42
5.1	The domain dimension and boundary conditions for the inclined gas column simulations. . . . .	47
5.2	Initial conditions of total density in the centerline plane (top) and vertical plane (bottom) used for simulations of a shock interacting with a column of dense gas initially inclined at $\alpha_1 = 30^\circ$ . . . . .	50
5.3	Density plots of the centerline and vertical planes at various dimensionless times $\tau$ for a Mach 2.0 shock interacting with an inclined circular column of heavy gas at an initial angle of $\alpha_1 = 30^\circ$ to the plane of the shock. . . . .	51
5.4	Comparison of the Kelvin-Helmholtz waves in the vertical plane of a) the 3D heavy gas column at $\tau = 38$ and b) a quasi-2D heavy gas curtain from chapter 4. at $\tau = 86$ . . . . .	52
5.5	Shock-driven Kelvin-Helmholtz wavelengths as a function of a) Mach number $M_1$ and b) initial column angle $\alpha_1$ . Error bars represent a 90% confidence interval over all measured waves. . . . .	53
5.6	Streamwise extent in the centerline plane for various a) Mach numbers $M_1$ and b) angles $\alpha_1$ . . . . .	54
5.7	SDKHI wavelengths normalized with (5.15). . . . .	55
5.8	a) Domain dimensions and boundary conditions for the inclined gas column simulations, b) illustration of the shock, the gas column, and the key cross-sectional planes. . . . .	58

*List of Figures*

5.9	Initial conditions of the density in the centerline plane (top) and in the vertical plane (bottom) used for simulations of a shock interacting with the gas column initially inclined at $\alpha_1 = 30^\circ$ . . . . .	61
5.10	Density plots of the centerline and vertical planes at various dimensionless times $\tau$ for a Mach 2.0 shock interacting with an inclined circular column of heavy gas at an initial angle of $\alpha_1 = 30^\circ$ to the plane of the shock. . . . .	62
5.11	Vertical plane slice of the cropped density field for a $30^\circ$ column at $\tau = 48.4$ . . . . .	63
5.12	Mean mass fraction and mean velocity profiles for a column with an initial tilt of $\alpha_1 = 30^\circ$ at different times. $\tau$ : — 12.4, - - - 30.4, - · - · 48.4, ····· 66.5. . . . .	65
5.13	R.M.S. velocity and Reynolds shear stress components for a column with an initial tilt of $\alpha_1 = 30^\circ$ at different times, $\tau$ , as indicated in fig. 5.12. . . . .	66
5.14	Anisotropic tensor components in the vertical plane at different times for columns with initial angles of a) $1^\circ$ , b) $5^\circ$ , c) $10^\circ$ and d) $30^\circ$ . The components are: - - - $b_{11}$ , - · - · $b_{22}$ , ····· $b_{33}$ . . . . .	68
5.15	Volume mean molecular mixidness ratio of $\text{SF}_6$ over time for different initial column angles. . . . .	69
6.1	Boundary conditions and domain dimensions. . . . .	74
6.2	Location of pressure sensors in experiments of Theofanous et al. (2016). . . . .	74
6.3	Upstream and downstream edges of the particle curtain over time compared to experiments (Theofanous et al., 2016). . . . .	81

*List of Figures*

6.4	Pressure traces at volume fractions of a) $\alpha_d = 1\%$ b) $\alpha_d = 5\%$ c) $\alpha_d = 10\%$ . . . . .	82
6.5	The GPU speedups for various particle counts. . . . .	83
6.6	Execution time for CPU and GPU simulations vs. number of particles.	84

# List of Tables

4.1	Values of post-shock angle, Kelvin-Helmholtz wavelength and the wavelength at the curtain foot for different initial curtain angles. . .	38
4.2	Values of post-shock angle, Kelvin-Helmholtz wavelength and the wavelength at the curtain foot for different initial angles. . . . .	39
4.3	Values of post-shock angle, Kelvin-Helmholtz wavelength and the wavelength at the curtain foot for different initial curtain widths. . .	41
6.1	Comparison of the reflected shock pressure ratio at different volume fractions obtained from simulations and experiments (Theofanous et al., 2016). . . . .	81

# Glossary

$L_x, L_y, L_z$	Domain dimensions.
$d_x, d_y, d_z$	Grid spacings.
$dt$	Timestep size.
$u, v, w$	Velocity components.
$\rho$	Total density.
$\rho_a, \rho_s$	Air and sulfur-hexafluoride densities.
$Y$	Mass fraction.
$e_t$	Specific total energy.
$e_i$	Specific internal energy.
$e_{KE}$	Specific kinetic energy.
$P$	Pressure.
$T$	Temperature.
$T_{amb}, p_{amb}$	Ambient temperature and pressure, respectively.
$R$	Gas constant.

## Glossary

$M_a, M_s$	Molecular weight of air and SF <sub>6</sub> , respectively.
$M_1, M_2$	Pre-shock and post-shock Mach numbers, respectively.
$C_p$	Specific heat at constant pressure.
$C_v$	Specific heat at constant volume.
$\gamma$	Ratio of specific heats.
$A$	Atwood number.
$\tau$	Dimensionless time.
$\alpha_1$	Initial inclination angle of column/curtain before shock interaction.
$\alpha_2$	Angle of column/curtain immediately after shock-transmission.
$\delta_1$	Initial diameter/width of gas column/curtain before shock interaction.
$\delta_2$	Compressed diameter/width of gas column/curtain immediately after shock transmission.
$\lambda_{KH}$	Mean wavelength of Kelvin-Helmholtz instability.
$\sigma_{KH}$	Standard deviation of Kelvin-Helmholtz instability wavelengths.
$\lambda_F$	Mean wavelength of curtain foot instability.
$BC_{IO}, BC_W$	Inflow/outflow and reflective wall boundary conditions, respectively.
TKE	Turbulent kinetic energy.
CFL	Courant–Friedrichs–Lewy number.
$\theta$	Mixidness.

## Glossary

$\alpha_d$	Particle volume fraction.
$\sigma^*$	Normalized width of circular gas cloud evolution.
$\mathbf{u}$	Velocity vector.
$\boldsymbol{\tau}$	Viscous stress tensor.
$\delta$	Dirac delta
$\mathbf{q}$	Conductive heat flux vector.
$S$	Strain-rate tensor.
$D_d$	Particle diameter.
$\mathbf{x}_d$	Particle position
$\mathbf{u}_d$	Particle velocity vector.
$\mathbf{F}$	Particle force Vector
$m_d$	Particle mass.
$T_d$	Particle temperature.
$Q$	Particle heat flux.
$C_d$	Particle drag coefficient.
$Nu$	Nusselt number.
$\kappa$	Fluid thermal conductivity.
$\mathbf{S}_m$	Cell local particle momentum.
$\beta$	Compressed (packed) particle volume fraction.

## *Glossary*

$(\cdot)_a$	Air.
$(\cdot)_s$	Sulphur hexafluoride SF <sub>6</sub> .
$(\cdot)_1$	Pre-shock.
$(\cdot)_2$	Post-shock.
$(\cdot)_d$	Particle (discrete) phase.

# Chapter 1

## Introduction

### 1.1 Background

The Richtmyer-Meshkov instability (RMI) (Richtmyer, 1960; Meshkov, 1972) is generated when a shock passes through a perturbed interface separating two gases with different densities. The instability is formed by misalignment of the pressure-gradient across the shock and the density-gradient across the interface. This misalignment results in the formation of baroclinic vorticity, which then leads to the growth of perturbations at the interface. As these perturbations grow, secondary, shear driven instabilities develop which cause smaller scale mixing (Vorobieff et al., 2004).

This process of shock-driven mixing by RMI occurs in flows at a range of scales. At the largest scales, shocks from supernova explosions propagate through gas and cosmic dust (Mendis and Rosenberg, 1994; Bocchio et al., 2014; Woitke, 2006), leading to formation of structures on the scale of light-years (Chevalier et al., 1992; Kane et al., 1999). The mixing of interstellar gases caused by these supernovae explosions are important for the creation of heavy elements. In contrast, inertial confinement fusion experiments produce flows on the scale of micrometers. In this case, shock-

## *Chapter 1. Introduction*

driven mixing has the undesirable effect of dissipating laser energy which reduces fuel compression and lowers fusion yield (Lindl et al., 1992). RMI can also be used to enhance the mixing of gaseous or liquid fuels in scramjet engines (Yang et al., 1993) and is essential for the operation of pulse detonation and rotating detonation engines (Huang et al., 2012). The RMI is also useful for blast mitigation through the use of sheets of aqueous foam (Ball and East, 1999).

Marble et al. (1989) proposed to use RMI for enhancing the rate of mixing between air and fuel in the combustion chamber of a scramjet engine. Their proposed mechanism injects gaseous fuel into a co-flowing region of air. This cylindrical jet of gas travels axially through the combustion chamber and passes through an oblique shock emanating from the chamber wall. The authors suggest that a cylindrical jet of gas passing through a standing oblique shock is geometrically equivalent to a moving shock passing through an inclined cylinder at rest. A cross-section of this geometry is then equivalent to the interaction of a shock with a circular bubble of gas, as shown in their two-dimensional (2D) simulations. Marble et al. (1990); Yang et al. (1993, 1994), describe additional 2D simulations and shock tube experiments that were conducted under similar conditions with one and more jets of gas. In particular, it was found that mixing rates produced by shock-bubble interactions were sufficient for sustaining supersonic combustion within a scramjet engine. Based on these results, a scramjet injector, known as the contoured wall injector, was developed in Marble et al. (1990) which utilizes this mixing process. Three-dimensional (3D) simulations of this device (Waitz et al., 1992) confirmed that vorticity generated by the mechanism described above provides sufficient mixing of fuel and air to sustain supersonic combustion. Recent numerical studies of shock-enhanced mixing involving the interaction of jets with oblique shocks are reported in Yang et al. (2014); Maddalena et al. (2014); Yu et al. (2020). These studies also focused on the streamwise vorticity produced by the interaction of a jet of fuel with multiple shocks. See Zhou (2017a,b); Zhou et al. (2019) for comprehensive reviews of RMI and related instabilities.

## Chapter 1. Introduction

Typical experimental studies of RMI have focused on the interaction of a planar shock with a single, sinusoidally perturbed interface. Variations from this configuration include finite-width gas layers, tilted interfaces, shock-bubble interactions, and shock-cylinder interactions (Tomkins et al., 2003; Vorobieff et al., 2003, 2004; Kumar et al., 2005). In particular, recent shocktube experiments were conducted by Olmstead et al. (2017b) to study the interaction of a planar shock with an inclined circular cylinder of heavy gas. This study found that the RMI caused a counter-rotating vortex pair in the cross-sectional plane normal to the cylinder axis. However, on the column surface, it was discovered that the shock caused a Kelvin-Helmholtz instability (KHI) to form. This type of KHI, driven directly by the passage of the shock, has been named the shock-driven Kelvin-Helmholtz instability (SDKHI). Olmstead et al. (2017b) described an apparent correlation between the Mach number and the Kelvin-Helmholtz instability wavelength and proposed a scaling mechanism which could be used to compare experiments at various initial column angles. An additional study by Olmstead et al. (2017a) used the same experimental data to analyze structure functions of scalar intensity maps. The power-law scalings exhibited by these structure functions deviated from those proposed by the Obukhov-Corsin and Kolmogorov theories (Celani et al., 2005; Sreenivasan, 1996; Villermaux et al., 2001). However, in-depth characterization of the effects of SDKHI on the transition to turbulence and mixing was not performed in the previous studies due to limitations of existing experimental techniques caused by the large range of scales involved and the impulsive nature of RMI and SDKHI.

Popular experimental techniques used to study flows exhibiting RMI and SDKHI include planar laser induced fluorescence (PLIF) and particle image velocimetry (PIV). These techniques present challenges to detailed studies of transition and mixing because they are limited to collecting data from a single plane at a given time. Certain important quantities, for example, pressure fields, also cannot be measured. PLIF requires diluting the test gas with a suitable tracer and cannot accurately

## *Chapter 1. Introduction*

measure planar velocity fields (Palmer and Hanson, 1994). PIV can provide velocity measurements but can suffer from particle lag and seeding effects (Martins et al., 2021) and may not capture fine scale fluctuating velocities. The experimental studies of (Olmstead et al., 2017a) in particular could not use PIV at higher Mach numbers due to both particle lag and seeding effects.

Numerical simulations are often used to complement experimental studies by providing additional data inaccessible to experiments. Direct numerical simulations (DNS) can produce detailed flow quantities at all scales of interest, but such simulations are still unfeasible for these types of flows due to their high computational costs. A more reasonable, commonly used alternative are large eddy simulations (LES).

Applicability of LES to the flows with RMI was tested in Thornber et al. (2018), including comparison of the results obtained with different codes. The study found excellent agreement amongst all the codes at high grid resolutions for various considered flow characteristics. Tritschler et al. (2014) determined that gas composition in the mixing layer was accurately predicted with different LES approaches when compared to experiments. Some of the highest resolution LES of RMI to date have been conducted by Wong et al. (2019). In particular, they found that at late times, after re-shock, the flow resembled that of the Batchelor-type decaying turbulence. The early development of RMI was also considered in high-resolution simulations by Groom and Thornber (2019).

However, only a few simulations of RMI arising from in the interaction of a shock with a gas column have been conducted previously (Palekar et al., 2007; Yang et al., 1993). These studies have mostly analyzed large scale flow features such as the interface width and the growth rate for 2D circular gas clouds. In the following work, a new code, FIESTA (Fast, Interface Evolution, Shocks, and Transition in the Atmosphere) is developed to enable very-high resolution LES of the interaction

## Chapter 1. Introduction

between a shock and an inclined column of dense gas as a means to provide further insight into the SDKHI phenomena.

Before moving on to fully 3D simulations, however, 2D simulations are completed in order to obtain a better understanding of how vorticity deposition in two orthogonal planes affects feature formation. The first plane of interest is referred to as the “centerline” plane in experiments Olmstead et al. (2017b): it is parallel to the direction of shock propagation, normal to the plane containing the axis of symmetry of the inclined gas column, and equidistant from the shock tube top and bottom walls as depicted in Fig. 1.1. In this plane, vorticity is initially dominated by a counter-rotating vortex pair, similar to one forming in quasi-2D experiments with gas columns at zero inclination angle. These quasi-2D experimental results, including planar velocity and gas species concentration maps (Vorobieff et al., 2003, 2004; Anderson et al., 2015) have already been used for code validation (Palekar et al., 2007; Anderson et al., 2015) and provide a good understanding of the general trends of the flow evolution. Centerline plane observations for the tilted column at moderate ( $30^\circ$  and below) tilt angles are at least qualitatively similar to those for the quasi-2D column (Olmstead et al., 2017b,a): the counter-rotating vortex pair formation due to the primary Richtmyer-Meshkov instability is similar, while there are some differences in the development of secondary instabilities.

Much less is known about what transpires in the plane containing the axis of the inclined cylinder (referred to as the “vertical” plane in experimental studies (Olmstead et al., 2017b,a), Fig. 1.1). Experiments with gas curtains were conducted earlier, but in a quasi-2D setting without the tilt (Vorobieff et al., 1998; Rightley et al., 1999). Experiments and simulations have also been conducted for quasi-2D tilted, single interfaces (Rasmus et al., 2019; Zhai et al., 2016; McFarland et al., 2011; Hahn et al., 2011), but not for finite-width tilted curtains. The presence of the tilt in the curtain simulation leads to shock-driven deposition of oppositely signed vorticity on

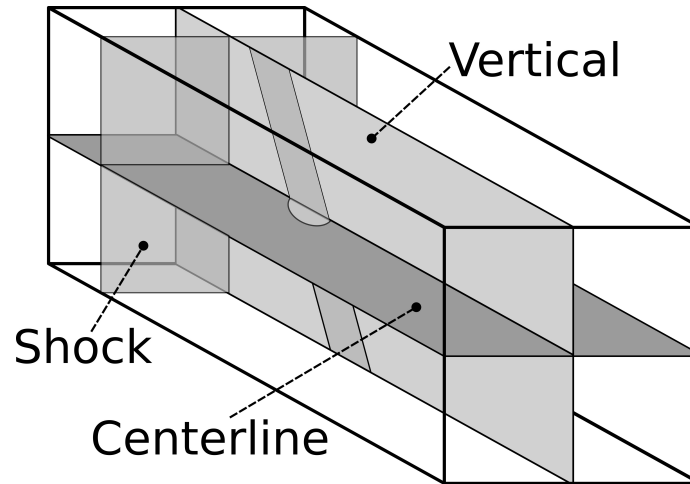


Figure 1.1: Orientation of the centerline and vertical planes in relation to the shock and inclined gas column before interaction.

the upstream and downstream edges of the curtain of dense gas, consistent with the Kelvin-Helmholtz instability observed in experiments with tilted cylinders.

## 1.2 Objectives

The current work intends to conduct very-high resolution simulations of shock driven flows. In order to conduct these simulations, a new computational fluid dynamics code (FIESTA) is developed which is capable of running larger, more efficient multi-phase, compressible large-eddy simulations than are possible with commonly available tools. FIESTA is then validated in 2D and 3D against experimental data from Olmstead et al. (2017a).

Using high-resolution simulation data from FIESTA, the first objective of this work is to numerically confirm SDKHI and to explore the effects of Mach number, initial column angle and column width of the flow morphology for the inviscid 2D case. The second objective is to explore the effects of dimensionality on SDKHI by

## *Chapter 1. Introduction*

comparing the development of the Kelvin-Helmholtz waves and the interface width between the inviscid 2D and 3D cases. For the third objective, 3D simulations are performed at a higher grid resolution and include viscosity modeling in order to investigate the effects of initial angle on mixing efficiency and other turbulent statistics in such a flow.

In many problems of fundamental or practical interest, transition to turbulence may also be effected by non-gaseous inclusions such as solid particles. Therefore, as the fourth objective in the current study, FIESTA is extended to include Lagrangian particle transport capabilities. The FIESTA Particle Extension (FIESTApx) is validated against published experimental data from Theofanous et al. (2016).

# Chapter 2

## FIESTA

### 2.1 Code Description

FIESTA (Fast Interface Evolution, Shocks and Transition in the Atmosphere) is an open-source, computational fluid dynamics code developed at the University of New Mexico. FIESTA is a scalable, exascale-ready, portable code which targets all the current major CPU and GPU platforms. FIESTA is designed to study multi-species and multi-phase compressible fluid flows containing shocks and exhibiting turbulent transition and mixing. FIESTA is capable of carrying out simulations at scales ranging from those characteristic for a laboratory shock tube to large atmospheric scales.

The code is written in the C++ language and takes advantage of object-oriented techniques to improve the code modularity and maintainability. FIESTA is written using the Kokkos C++ Performance Portability Ecosystem (Edwards et al., 2014) in order to target both traditional CPU architectures as well as General Purpose Graphics Processing Units (GPGPUS) while avoiding the code complexity and duplication required when supporting application programming interfaces for multiple compute

environments for different architectures. Output files are formatted using the HDF5 file format (Koranne, 2011). Input files are written in the Lua language (Ierusalimsky, 2016) allowing for easy parameterization of a problem. Multi-GPGPU support is provided by the Message Passing Interface (MPI).

The code has a modular design allowing for different physics and models to be included in a computation. There are currently modules for solving two and three dimensional multi-species Euler equations on generalized curvilinear or uniform rectangular structured grids. The Euler equations are solved using the simplified 5th-order weighted essentially non-oscillatory (WENO) finite difference scheme (Ramani et al., 2019a,b; Jiang and Shu, 1996). The time scheme used is a low storage, second-order explicit Runge-Kutta integrator (Williamson, 1980). The pressure gradient term is approximated using the fourth-order central difference scheme (Ramani et al., 2019a,b).

The FIESTA Kernel Library also provides the Quadratic Upwind Interpolation for Convective Kinematics (QUICK) scheme and a second order centered finite difference scheme. For time integration, FIESTA offers a fourth order Runge-Kutta scheme in addition to the second order scheme described previously. In 2D, FIESTA implements the C-Model for artificial viscosity and wavelet based noise indicator developed by Ramani et al. (2019c,a).

## 2.2 FIESTA Capabilities

FIESTA supports several 2D and 3D grid types for both fluid flows and fluid flows with particles. The following examples showcase these features and demonstrate some of the problems FIESTA can be used to solve.

### 2.2.1 2D Generalized Coordinates.

In 2D, FIESTA supports uniform rectangular grids (see Chapter 4) as well as generalized curvilinear coordinates. Figure 2.1 shows an example of a 2D idealized expansion simulation performed using the generalized grid capabilities in FIESTA. The figure depicts a hot ( $3000\text{K}$ ), dense ( $1000\text{ kg/m}^3$ ) region of air expanding and reflecting off of a sinusoidal surface. The expansion occurs in ambient air at  $300\text{K}$  and  $1\text{ kg/m}^3$  in a domain that is approximately  $1\text{ m}^2$ , discretized with a  $1000 \times 1000$  curvilinear grid. The top and sides employ free-flow boundary conditions while the bottom, perturbed surface is modelled by reflective, slip wall conditions. In this problem the wavelet-based noise indicator and the C-Model at the wall (Ramani et al., 2019a,b) are also implemented in FIESTA.

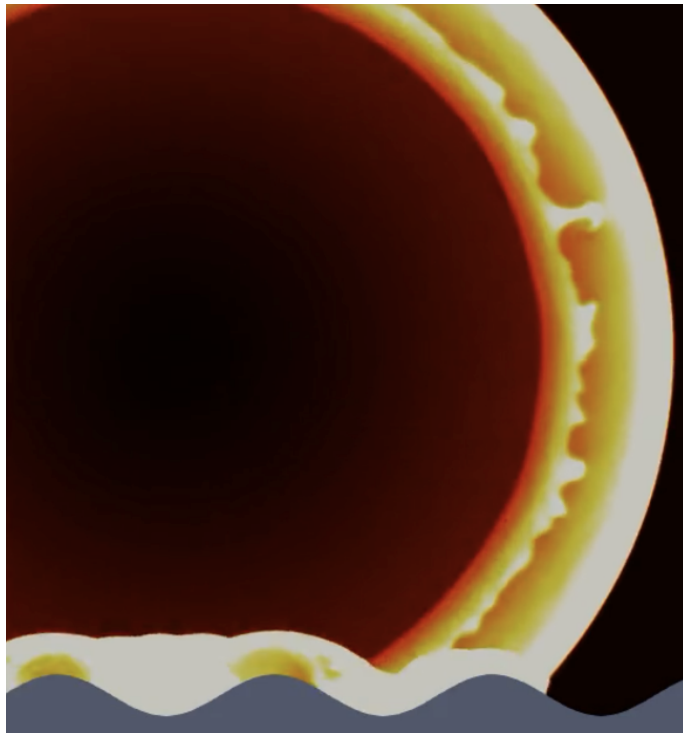


Figure 2.1: 2D idealized expansion over a corrugated surface.

### 2.2.2 3D Terrain Following Coordinates

For 3D flows, FIESTA supports uniform rectangular grids (see Chapter 5) as well as generalized curvilinear grids and terrain following coordinates. The use of terrain following coordinates reduces the memory requirements when modelling surfaces with elevation changes, such as terrain. Figure 2.2 shows an example of a 3D idealized expansion problem performed on a  $512 \times 512 \times 512$  grid using terrain following coordinates. The problem shows a hot ( $3000\text{K}$ ), dense ( $1000 \text{ kg/m}^3$ ) region of air expanding in ambient air at  $300\text{K}$  and  $1 \text{ kg/m}^3$  over artificially generated terrain.

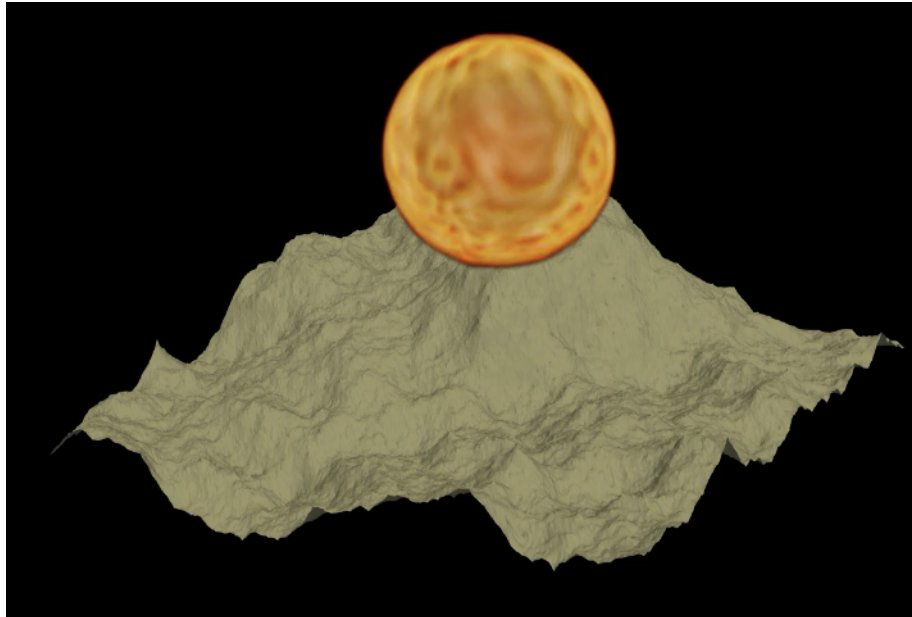


Figure 2.2: 3D idealized expansion over terrain.

### 2.2.3 2D Buoyant Plume

Figure 2.6 shows snapshots of a buoyant plume in a crosswind. This simulation was performed on a uniform rectangular  $400 \times 500$  grid. A constant temperature source is prescribed in a region near the lower boundary. The left side boundary defines

## Chapter 2. FIESTA

a constant velocity inflow condition, while the upper and right sides are freeflow boundaries and the bottom is a reflective wall. This problem demonstrates the flexibility of the boundary condition system employed in FIESTA which is capable of defining inflow conditions and arbitrary sources in the Lua input files.

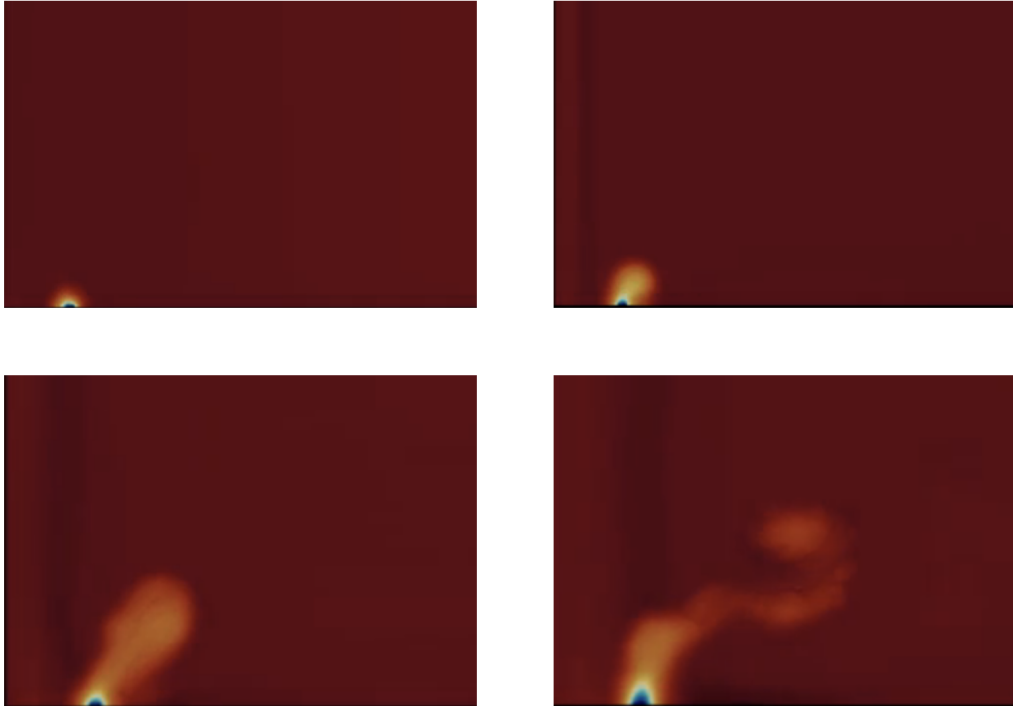


Figure 2.3: 2D rising plume.

### 2.2.4 2D Particle Extension

2D and 3D Lagrangian particle transport capabilities have been added with the FIESTA Particle Extension (FIESTApx). Figure 2.4 shows a 2D idealized expansion taking place within a  $1 \text{ m}^2$  quadrant containing 200,000 1 mm diameter particles. FIESTApx can use both one-way coupling in which the particles have no influence on the fluid, or two-way coupling which utilizes a momentum exchange model (see Chapter 6 for details).

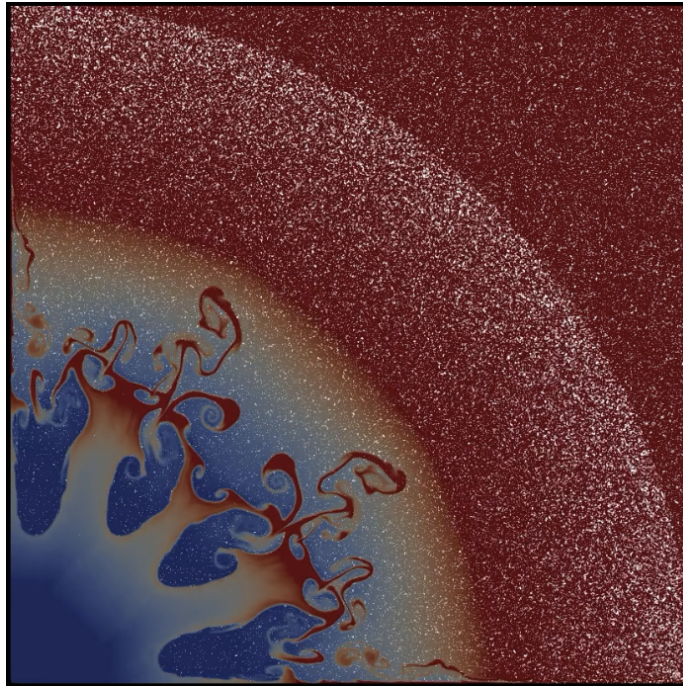


Figure 2.4: Idealized expansion in a particle laden gas.

## 2.3 FIESTA Verification

To verify FIESTA, simulations of a one-dimensional (1D) Sod problem (Sod, 1978) which has an analytical solution were conducted. The Sod problem is a 1D Riemann problem that describes the evolution of density and pressure interfaces on the domain  $0 \leq x \leq 1$ . The pressure and density interfaces cause a shock wave to form, which travels to the right, and a rarefaction wave, which travels to the left.

In the problem, the interface is initially located at  $x = 0.5$  and separates two regions. The initial conditions in the first region  $0 \leq x \leq 0.5$  are:  $p_1 = 1.0$ ,  $\rho_1 = 1.0$ ,  $u_1 = 0.0$ . In the second region  $0.5 < x \leq 1.0$ , the following initial conditions are used:  $p_2 = 0.1$ ,  $\rho_2 = 0.125$ ,  $u_2 = 0.0$ .

This problem was simulated in FIESTA using the 3D Euler equations for an ideal

gas (see section 5.1) on a  $500 \times 10 \times 10$  domain using periodic conditions in the y- and z-directions.

Figure 2.5 compares the simulation results to the analytical solution presented in LeVeque et al. (2002) at time  $t = 0.2$ . The solutions are in excellent agreement with each other.

The simulation was repeated with the domain oriented in the y-direction with periodic conditions in the x- and z-direction on a  $10 \times 500 \times 10$  grid and also with the domain oriented in the z-direction with periodic conditions in the x- and y- directions on a  $10 \times 10 \times 500$  grid. Results from these simulations are identical to the results obtained with the domain oriented in the x-direction.

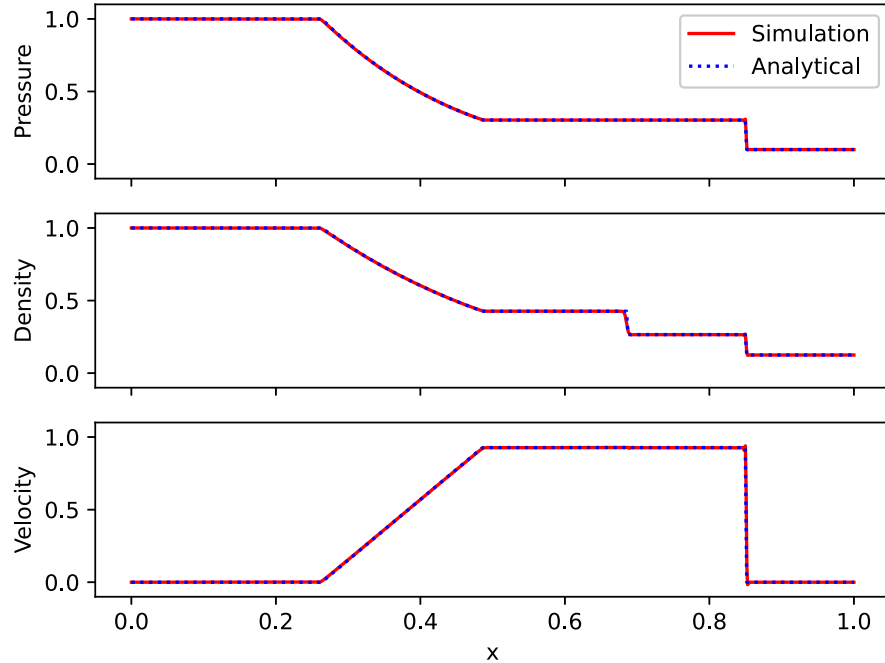


Figure 2.5: Comparison of simulation data with the analytical solution of a 1D Sod problem.

## 2.4 FIESTA Performance

Figure 2.6 compares performance of FIESTA on several platforms. For this test, a 3D idealized expansion problem on a  $512 \times 512 \times 512$  uniform rectangular grid was solved. In the first case, the problem was run on one core of an Intel E5-2695v4 CPU. It took 35 minutes to run the problem for 1000 timesteps. Running the same problem on an NVIDIA K40M GPU took just under 6 minutes for a speedup of about  $6 \times$ . More dramatic speedups were seen with the NVIDIA P100 GPU. The current fastest GPU, the NVIDIA A100, executed the problem in 27 seconds for a speedup of 77 times.

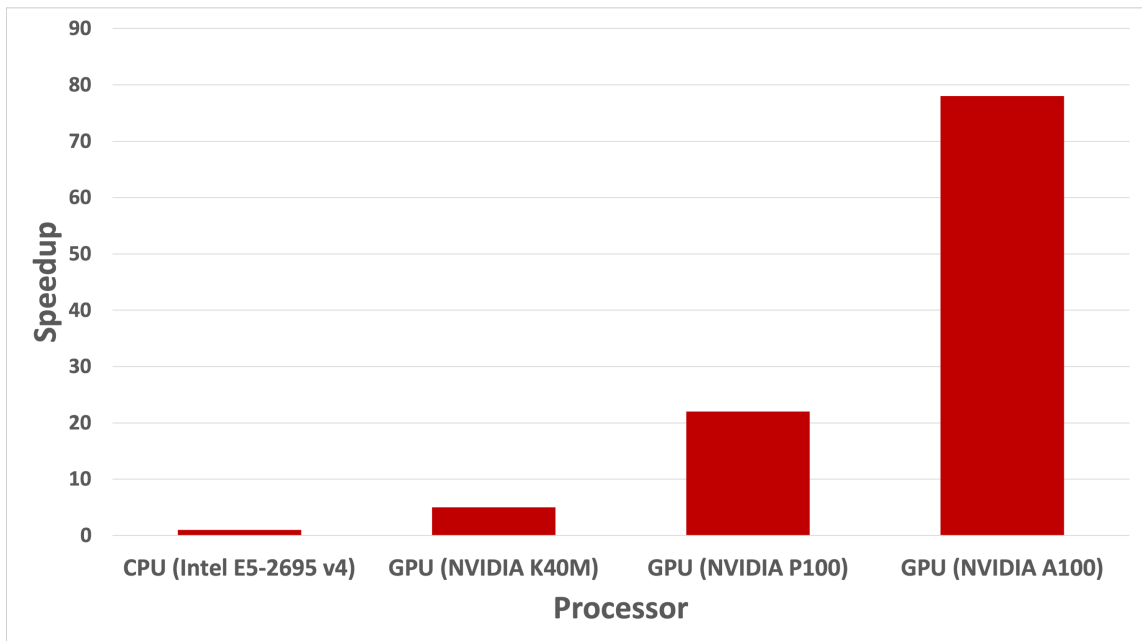


Figure 2.6: Speedups for a  $512^3$  ideal expansion problem on various devices.

# Chapter 3

## Reference Data

Data from the shock-tube experiments of Olmstead et al. (2017b,a) are used as a reference for our simulations. The experiments were conducted at the University of New Mexico tiltable shock tube. Prior to release of the shock, the optically transparent test section of the shock tube is maintained at atmospheric pressure. A cylindrical jet of heavy gas (a mixture of sulfur hexafluoride  $\text{SF}_6$  and acetone with traces of air) is injected downward through the top wall of the test section and exits through a hole in the bottom wall. This jet is surrounded with a co-flowing cylindrical jet of air, so that the flow is laminar and any mixing between the air (density  $\rho_a$ ) and the heavy gas (density  $\rho_s$ ) is diffusive. The entire shock tube can be tilted to an angle  $\alpha_1$  with respect to the horizontal plane. With a column injection system chosen for a specific  $\alpha_1$ , the jet with nominal diameter  $D_{IC}$  flows as shown in Fig. 3.1.

Once these initial conditions are established, the shock tube produces a planar shock wave at a prescribed Mach number  $M_1$ . The shock front propagates from the driver section (not shown in Fig. 3.1) toward the test section. Behind the shock front the air is compressed and moving with piston velocity  $\Delta V$ .

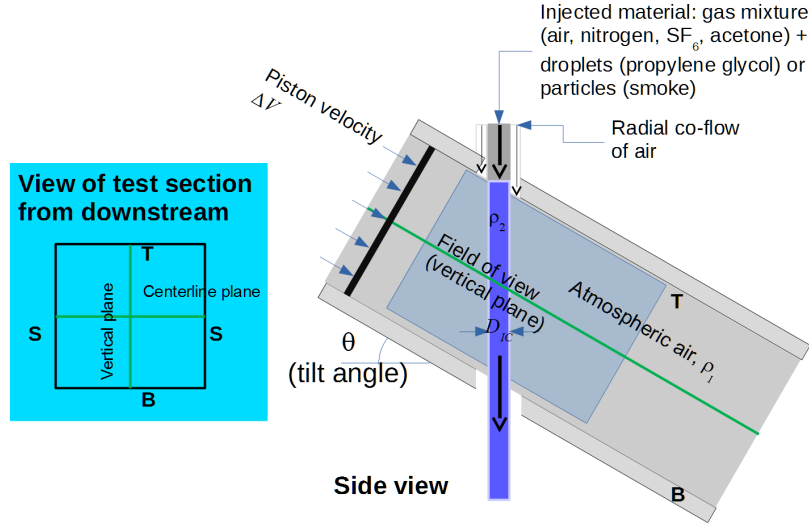


Figure 3.1: The experimental setup for studies of shock interaction with an inclined cylindrical density interface as in Olmstead et al. (2017a,b).

During the experiments, pressure traces are collected at multiple downstream locations to monitor the shock propagation and to trigger the imaging system, which can capture images in two planes. The first visualization plane (vertical plane) is parallel to the shock direction and equidistant from the vertical walls of the test section. The second plane (centerline plane) is parallel to the top and bottom walls and tilted at the same angle  $\alpha_1$  as the shock tube. Each plane can be illuminated with precisely timed, short ( $\sim 5$  ns) pulses of a frequency-quadrupled (wavelength 266 nm) Nd:YAG laser. The laser beam passes through a combination of a cylindrical and a spherical lens, forming a laser sheet that selectively illuminates a narrow (submillimeter) planar cross-section of the flow. The acetone in the injected heavy gas mixture fluoresces in the visible range at 480 nm when lit with the 266-nm laser pulse.

The governing parameters of the flow are  $\delta_1$ ,  $\alpha_1$ ,  $M_1$ , and the Atwood number,

$$A = \frac{\rho_2 - \rho_1}{\rho_2 + \rho_1}. \quad (3.1)$$

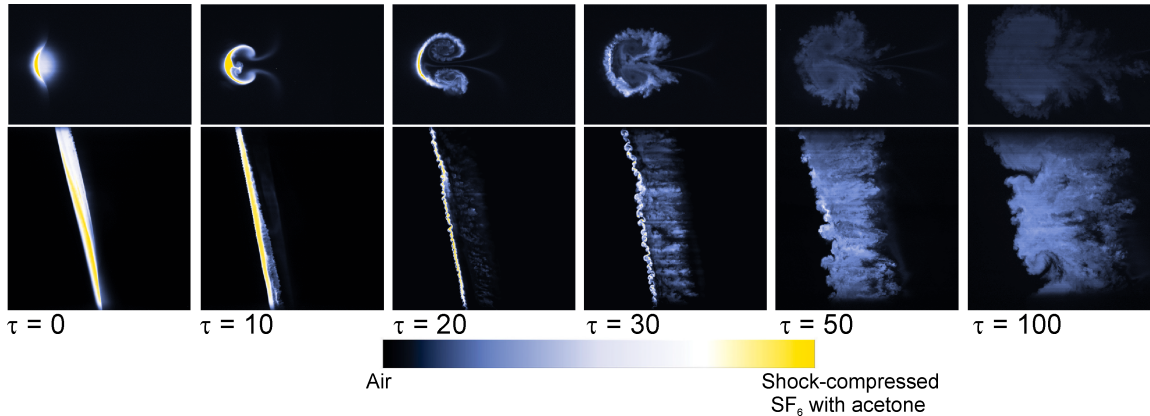


Figure 3.2: Representative experimental image sequence showing shock acceleration of a gas cylinder at a tilt angle  $\alpha_1 = 20^\circ$ ,  $M = 2$ ,  $A = 0.6$  (Olmstead et al., 2017a).  $\tau$  is dimensionless time (refer to text). The top image for each  $\tau$  shows the centerline plane, the bottom image – the vertical plane. Figure reproduced from Olmstead et al. (2017a) with the permission from the authors.

Figure 3.2 shows an example of an image sequence in two planes (Olmstead et al., 2017b,a). Dimensionless time  $\tau$  is defined there in accordance with Richtmyer’s linear theory as

$$\tau = kA\Delta Vt, \quad (3.2)$$

where  $t$  is dimensional time and  $k = 2\pi/D_{IC}$  is the dominant wavenumber of the initial density perturbation. In terms of  $\tau$ , the initial RMI growth rates should remain the same for the same initial condition geometry, not changing with  $A$  or  $M$  (although this assertion is only valid for very early – linear – perturbation growth). The volume in the flow where the perturbed heavy gas mixes with the surrounding lighter gas is commonly referred to as the **mixing zone**, and its streamwise and spanwise extent can serve as quantitative code-validation benchmarks.

In the centerline plane, the dominant flow feature is a pair of counter-rotating vortices that roll up due to RMI. In the vertical plane, however, small-scale vortices form on the leading and trailing edges of the heavy-gas cylinder (Olmstead et al.,

### Chapter 3. Reference Data

2017b). These two types of vortices can be seen in the sequences depicted in Figs. 3.2 and 3.3. Based on the observed morphology, it was suggested that the vortex formation mechanism responsible for these features in the vertical plane (Fig. 3.4) is KHI due to shock-driven vorticity deposition on the inclined density interfaces (Wayne et al., 2015; Olmstead et al., 2017b; Romero et al., 2021b). As the flow evolves, secondary instabilities begin to emerge in both planes, leading to enhanced mixing in increasingly disordered flow. At later times, the flow statistics are consistent with those of turbulent flows (Olmstead et al., 2017a).

The experimental results described above can be used to develop a well-characterized set of quantitative benchmarks for validation of numerical codes modeling shock-driven mixing and /or multiphase flow. We begin with a validation exercise for the case of a single-phase density interface, as described in the next chapter.

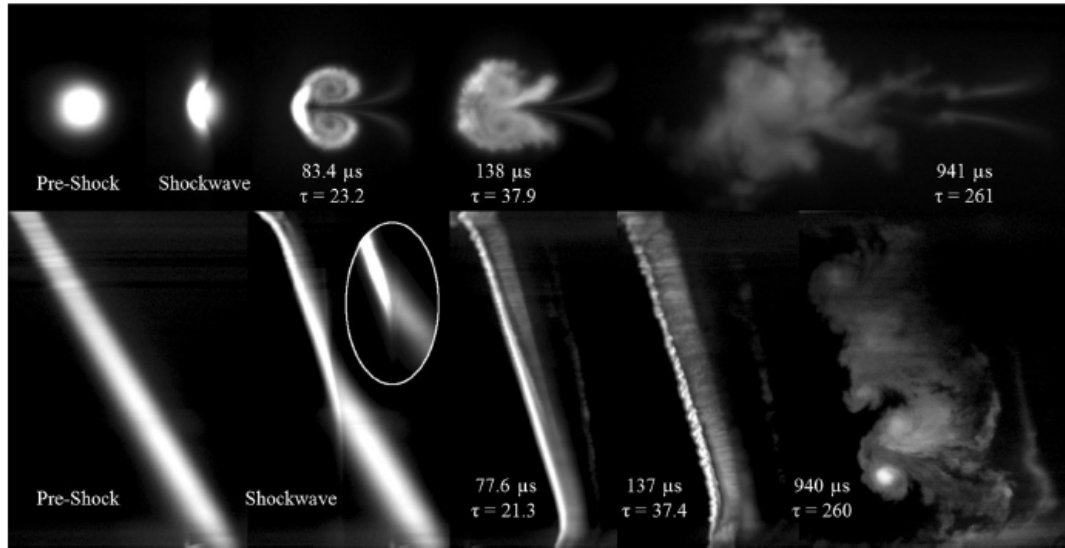


Figure 3.3: Mach 2.0,  $\alpha_1 = 30^\circ$ . Figure reproduced from Olmstead et al. (2017b) with the permission from the authors.

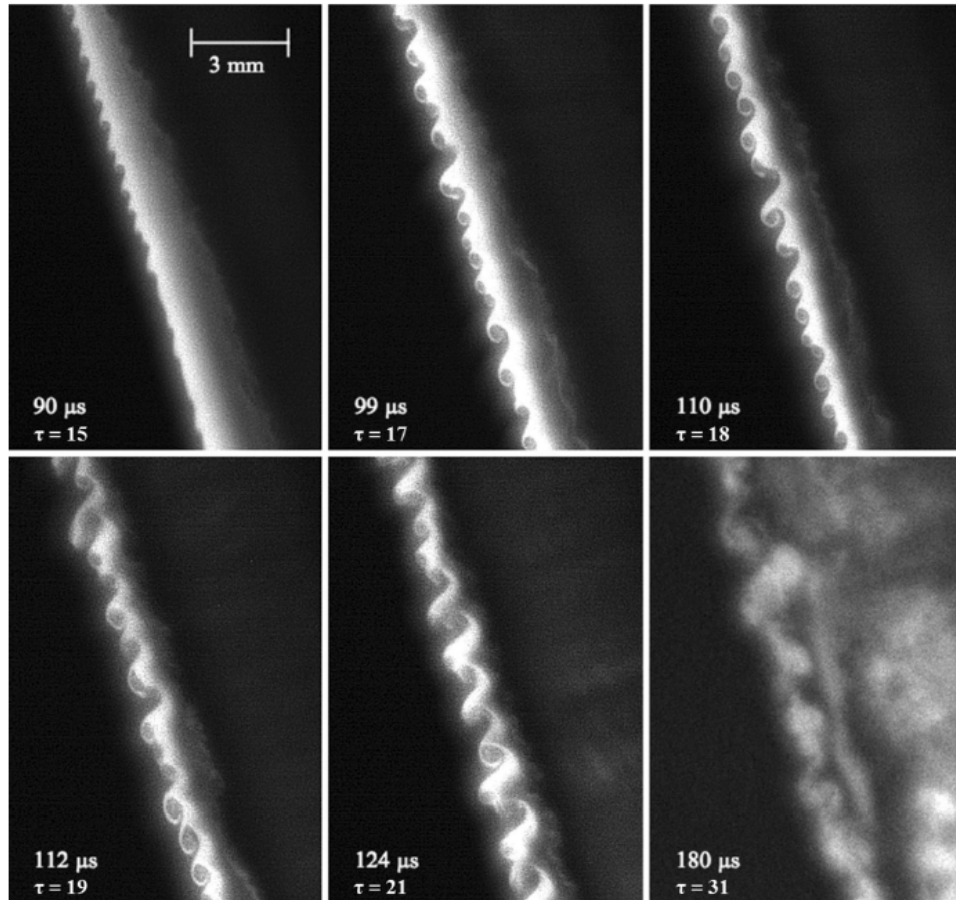


Figure 3.4: Shock-driven Kelvin-Helmholtz instability. Figure reproduced from Olmstead et al. (2017b) with the permission from the authors.

# Chapter 4

## 2D SDKHI Cases

### 4.1 Introduction

In this chapter, 2D simulations are conducted to examine the vorticity deposition and feature formation in the two characteristic planes (Fig. 1.1) of an oblique shock-cylinder interaction. These planes correspond to those for which PLIF data were collected in Olmstead et al. (2017b). The objectives are to confirm numerically the SDKHI phenomenon and to provide data for velocity and vorticity fields to advance our understanding of this phenomenon.

The first of these simulations are used to examine the case of a shock interacting with a 2D, circular cloud of dense gas. This configuration isolates the flow features that develop in the centerline plane (Fig. 1.1) in order to verify that simulations can reproduce the counter-rotating vortex pair.

Simulations are then conducted for a 2D, finite width, inclined curtain, corresponding to the vertical plane in experiments (Fig. 1.1) in order to isolate the KHI development seen in experiments. The initial curtain angles vary as  $\alpha_1 =$

$0^\circ, 10^\circ, 20^\circ, 30^\circ, 40^\circ$  for a fixed Mach number ( $M_1 = 2.0$ ) at the curtain width ( $\delta_1 = 10.4$  mm). Then, for the case of  $\alpha_1 = 30^\circ$ ,  $\delta_1 = 10.4$  mm curtain, Mach numbers  $M_1 = 1.13, 1.4, 1.7, 2.0$  are considered. Finally, for  $M_1 = 2.0$ ,  $\alpha_1 = 30^\circ$  the curtain initial curtain width is varied as  $\delta_1 = 5.2$  mm, 10.4 mm, 15.6 mm, 20.8 mm.

Results include comparison of the flow evolution in the two planes to the experiments of Olmstead et al. (2017b). The effects of the parameters discussed above on the KHI wavelength and curtain growth are analyzed. Grid sensitivity of the KHI wavelength is also evaluated and an additional flow feature developing near the curtain foot is discussed.

## 4.2 2D Governing Equations

For 2D simulations, two-species Euler equations were solved in their conservation form. These equations consist of the continuity equations for each gas species, the equations for each momentum component, and the conservation equation for the specific total energy. The set of equations is provided in the vector form below:

$$\frac{\partial}{\partial t} \begin{bmatrix} \rho \\ \rho u \\ \rho v \\ \rho e_t \\ \rho Y_s \end{bmatrix} + \frac{\partial}{\partial x} \begin{bmatrix} \rho u \\ \rho u^2 + p \\ \rho v u \\ (\rho e_t + p)u \\ \rho u Y_s \end{bmatrix} + \frac{\partial}{\partial y} \begin{bmatrix} \rho v \\ \rho u v \\ \rho v^2 + p \\ (\rho e_t + p)v \\ \rho v Y_s \end{bmatrix} = 0. \quad (4.1)$$

Here,  $\rho$  is the density of the mixture,  $Y_s$  is the mass fraction of sulphur-hexafluoride ( $\text{SF}_6$ ),  $u, v$  are velocity components in the  $x$  and  $y$  directions, respectively, where  $x$  and  $y$  are stream-wise and span-wise directions,  $p$  is static pressure and  $e_t$  is specific total energy.

## Chapter 4. 2D SDKHI Cases

The pressure of the gas mixture is computed with Dalton's mixing law (Dalton, 1802) and assumes ideal gas behavior:

$$p = \rho (Y_s R_s T + (1 - Y_s) R_a T) \quad (4.2)$$

Note that the applicability of ideal gas approximation for the conditions here has been explicitly assessed in White et al. (2020), revealing that the shock should not be strong enough to produce notable non-ideal effects in the mixture, with the compressibility factor  $z$  being close to unity ( $z = 1.02$  in the worst case). While it was recently suggested that Dalton's law itself may produce misleading results for shock-compressed gas mixtures (Wayne et al., 2019), this reported observation only applies to an extreme case of disparities between gas properties in the mixture (sulfur hexafluoride – helium), which is not considered in the present work.

The mixture temperature is obtained from the internal energy as follows:

$$T = \frac{e_t}{C_{v_{\text{mix}}}}, \quad (4.3)$$

where the mixture specific heat  $C_{v_{\text{mix}}}$  is computed from the species specific heats and mass fractions as follows:

$$C_{v_{\text{mix}}} = Y_s C_{v,s} + (1 - Y_s) C_{v,a}. \quad (4.4)$$

Expressions for the specific heats of individual species are

$$C_{v,a} = \frac{R_a}{\gamma_a - 1}, \quad C_{v,s} = \frac{R_s}{\gamma_s - 1}. \quad (4.5)$$

Chapter 4. 2D SDKHI Cases

The gas constants for each individual species are

$$R_a = \frac{R}{M_a}, \quad R_s = \frac{R}{M_s}, \quad (4.6)$$

where  $R$  is the universal gas constant,  $M_a$  is the molecular weight of air and  $M_s$  is the molecular weight of  $\text{SF}_6$ .

The code solves fully dimensional equations. The specific values of parameters utilized in the code are,  $R = 8.314462 \frac{\text{J}}{\text{kg}\cdot\text{mol}}$ ,  $M_a = 0.028966 \frac{\text{kg}}{\text{mol}}$ ,  $M_s = 0.14606 \frac{\text{kg}}{\text{mol}}$ ,  $\gamma_a = 1.402$ , and  $\gamma_s = 1.092$ .

Solution of Eq. 4.1 requires defining pre-shock and post-shock initial states. Initial density distributions for the gas cloud and curtain are described below. The pre-shock state is defined as atmospheric pressure and room temperature similar to the conditions observed in the experiments of Olmstead et al. (2017b). The post-shock conditions are determined from the inviscid normal shock relations:

$$M_2 = \sqrt{\frac{M_1^2 + \frac{2}{\gamma-1}}{\frac{2\gamma}{\gamma-1}M_1^2 - 1}} = 0.577, \quad (4.7)$$

$$\frac{T_2}{T_1} = \frac{1 + \frac{\gamma-1}{2}M_1^2}{1 + \frac{\gamma-1}{2}M_2^2} = 1.614, \quad (4.8)$$

$$\frac{\rho_2}{\rho_1} = \frac{(\gamma+1)M_1^2}{(\gamma-1)M_1^2 + 2} = 2.667. \quad (4.9)$$

In Eqs. 4.7-4.9, ambient, or unshocked conditions are indicated with subscript 1. Conditions behind the shock wave, also known as the post-shock conditions are

## Chapter 4. 2D SDKHI Cases

indicated with subscript 2. The Mach number specified in each simulation is the pre-shocked, or ambient Mach number,  $M_1$ .

From these relations, the post-shock conditions  $\rho_2$  and  $T_2$  can be determined. The post-shock velocity is determined by the Mach number and the speed of sound:

$$u_2 = M_2 a_2 = 433.9m/s, \quad (4.10)$$

$$a_2 = \sqrt{\gamma R T_2} = 752.0. \quad (4.11)$$

Finally, the post-shock total specific energy is related to internal energy and kinetic energy by temperature and velocity as:

$$e_{t2} = e_{i2} + e_{KE2}, \quad (4.12)$$

$$e_{i2} = \rho_2 C_v T_2, \quad (4.13)$$

$$e_{KE2} = \frac{1}{2} \rho_2 u_2^2. \quad (4.14)$$

The distribution of  $\text{SF}_6$  gas concentration,  $w_s = \rho_s/\rho$ , across both the gas cloud and the gas curtain is described by a Gaussian-based distribution with a maximum concentration of 1.0 at  $x = x_0$ :  $w_s = \exp[-(x - x_0)^2/2\sigma^2]$ , where  $x_0$  is the location of the center of the curtain (or the cloud). The value of  $\sigma = 1.71mm = \delta/6.8$  is chosen so that the gas concentration would be similar to that used in experiments. Figure 4.1 compares the gas distribution used in the simulations to that used in the experiments.

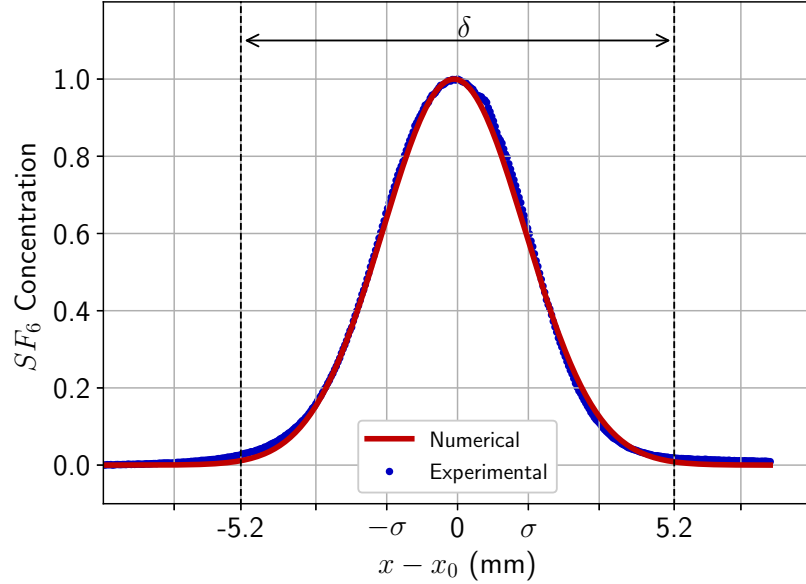


Figure 4.1: Plot comparing the experimental  $\text{SF}_6$  concentration across the gas cloud and curtain with the distribution used in simulations.

## 4.3 2D Circular Gas Cloud

### 4.3.1 Simulation Setup

Fig. 4.2 represents the domain used for the 2D, circular gas cloud simulations. In this domain,  $L_x = 20\delta$  is the length of the domain, and  $L_y = 3\delta_1$  is the width. In simulations,  $\delta_1 = 10.4\text{mm}$  is the circular diameter of the gas cloud measured at the location where the concentration has a value of 1%. All four sides of the domain are inflow/outflow ( $BC_{IO}$ ) boundaries as described below.

The inflow/outflow boundary conditions are defined as:

$$\partial_x \rho(x, t) = 0, \quad \partial_x \rho u(x, t) = 0, \quad \partial_x \rho v(x, t) = 0, \quad \partial_x \rho e_t(x, t) = 0,$$

where  $\partial_x = \frac{\partial}{\partial x}$  and  $\partial_y = \frac{\partial}{\partial y}$  are the derivatives in the x and y directions, respectively.

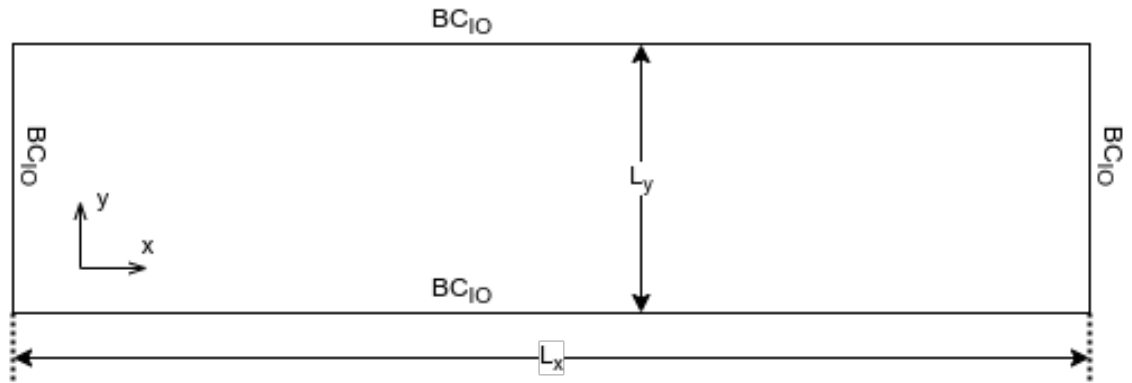


Figure 4.2: Dimensions and boundary conditions for the circular gas cloud simulations.

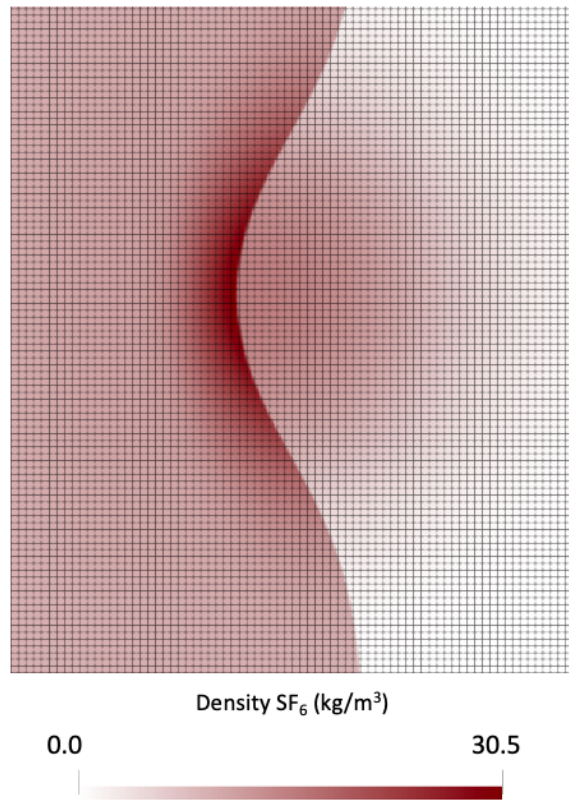


Figure 4.3: Computational grid (every eighth gridline shown) at  $\tau = 0$  for the shock as it passes through a circular gas cloud

## Chapter 4. 2D SDKHI Cases

Simulations use a Cartesian grid with  $dx = dy = 2.5 \times 10^{-5}m \approx \delta/400$ . This resolution exceeds that used in the shock-bubble simulations of Palekar et al. (2007) by a factor of 4. This resolution also allows the shock to be resolved with at least 4 grid cells. A timestep,  $dt = 5 \times 10^{-9}$  is chosen resulting in a CFL number, based on the maximum wave speed of  $CFL = 0.1$ .

The gas cloud simulation used a  $8,000 \times 1,200$  grid and was computed for 100,000 timesteps for a total simulation time of  $0.5ms$ . This simulation duration was long enough for both rollup, and the secondary instabilities described in Vorobieff et al. (2004) to develop. Figure 4.3 shows the grid spacing near the gas cloud during shock passage.

The initial conditions for the simulation in the case of the circular gas cloud configuration is shown in Fig. 4.4, colored according to density level. The post-shock area on the left is seen in crimson, and the ambient, pre-shock conditions are seen in white. The circular cloud of dense gas is located in the pre-shock region. Pressure is uniformly distributed within each of the two regions.

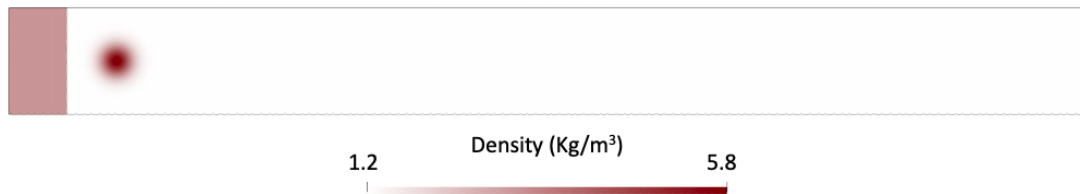


Figure 4.4: Initial conditions used in the simulation of a shock passing through a circular gas cloud.

### 4.3.2 Results

As the simulation progresses, the shock travels to the right through the gas cloud. Figure 4.5 shows the gas cloud shape at two different times from the simulations and the experiments. The dimensionless time is defined as  $\tau = kAu_2(t - t_0)$ . Here

## Chapter 4. 2D SDKHI Cases

$k = 2\pi/\delta_1$  is the wave-number based on the initial cylinder diameter,  $\delta_1$ ,  $A = (\rho_{sf6} - \rho_{air})/(\rho_{sf6} + \rho_{air})$  is the Atwood number,  $u_2$  is the post-shock velocity, and  $t_0$  is the time at which the shock passes through the center of the gas cloud. Similar development of the gas cloud was observed in experiments (Fig. 4.5b,d) including the development of the “mushroom-cap” shape shown in Fig. 4.5c. The shape develops at nearly the same time in the simulation ( $\tau = 23.1$ ) and in the experiment ( $\tau = 23.2$ ).

The width of the gas cloud over time is compared to experiment in Fig. 4.6. The cloud width is measured from the upstream edge where the cloud reaches a concentration of 0.1%, to the downstream edge at the same concentration. The width is then normalized by  $w_0 M_1^{0.5}$  as in Olmstead et al. (2017b), where ( $w_0 = \delta_2 \cos(\alpha_2)$ ) and  $\delta_2$  is the cloud width immediately after the shock passage. The normalized cloud width is represented by  $\sigma^*$ . The figure shows that the streamwise growth of the gas cloud in 2D simulations is similar to the growth of the cloud in the cross sectional plane of the inclined gas column from experiments when scaled in this manner.

## 4.4 2D Gas Curtain

### 4.4.1 Simulation Setup

The domain used for the inclined gas curtain simulations is depicted in Fig. 4.7. In this domain,  $L_x = 0.6m \approx 60\delta$  is the length of the domain, and  $L_y = 0.15 \approx 15\delta$  is the width. The boundaries at  $x = 0$  and  $x = L_x$  are inflow/outflow boundaries ( $BC_{IO}$ ) as defined previously in section 4.3.1. The boundaries at  $y = 0$  and  $y = L_y$  are reflective wall conditions ( $BC_W$ ) defined as follows:

$$\partial_y \rho(x, t) = 0, \quad \partial_y \rho u(x, t) = 0, \quad \rho v(x, t) = 0, \quad \partial_y \rho e_t(x, t) = 0,$$

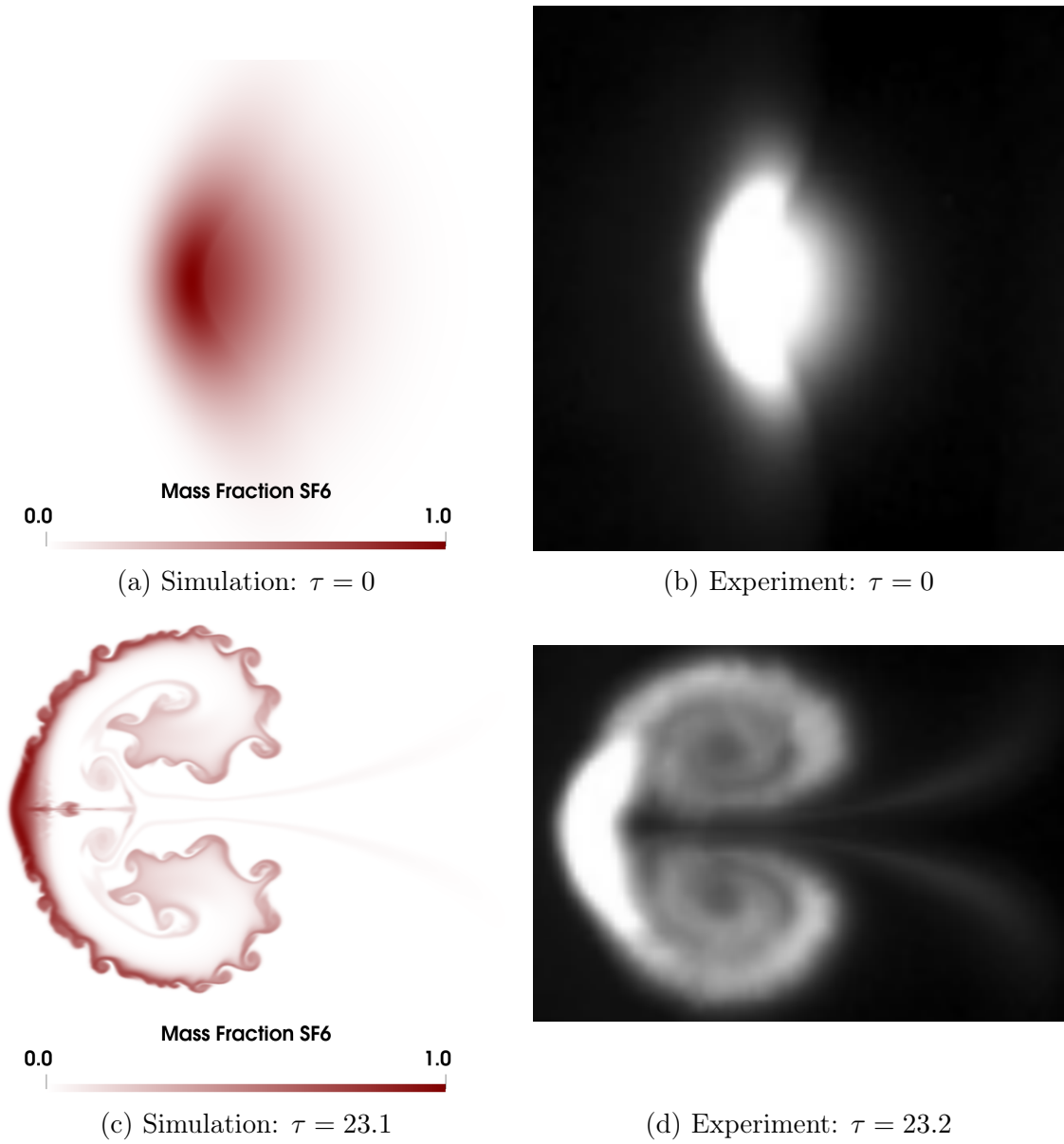


Figure 4.5: Interaction of a shock with a gas cloud at different times.

The simulations use a  $24,000 \times 6,000$  rectangular grid with the same spacing ( $dx = dy = 2.5 \times 10^{-5}m \approx \delta/400$ ) and time step ( $dt = 5 \times 10^{-9}$ ) as the 2D cloud simulations and were computed for 200,000 timesteps. The simulation duration of  $1ms$  was long enough for the shock-driven Kelvin-Helmholtz instability (as seen in

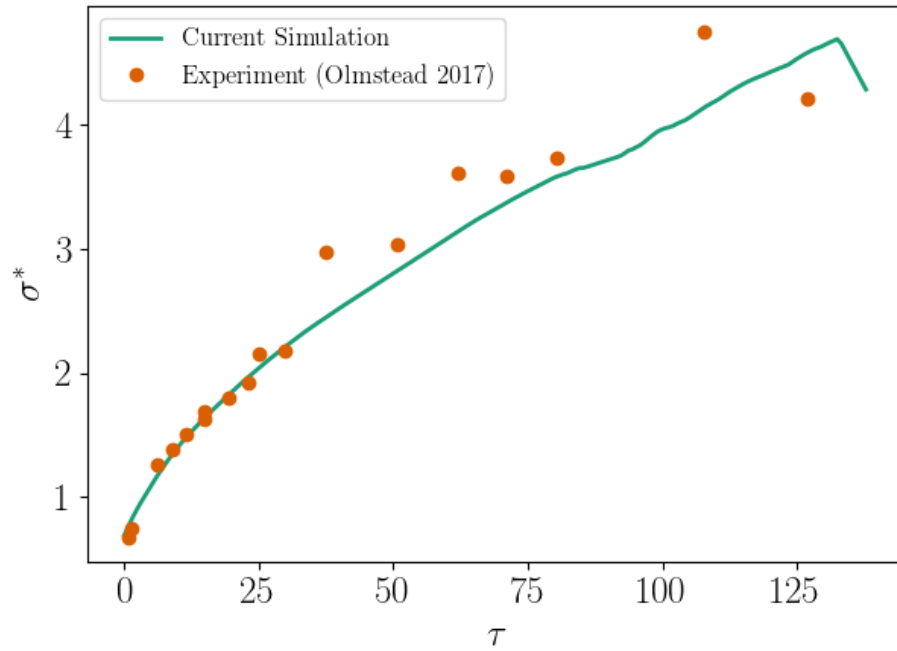


Figure 4.6: Normalized cloud width over time compared to experiment.

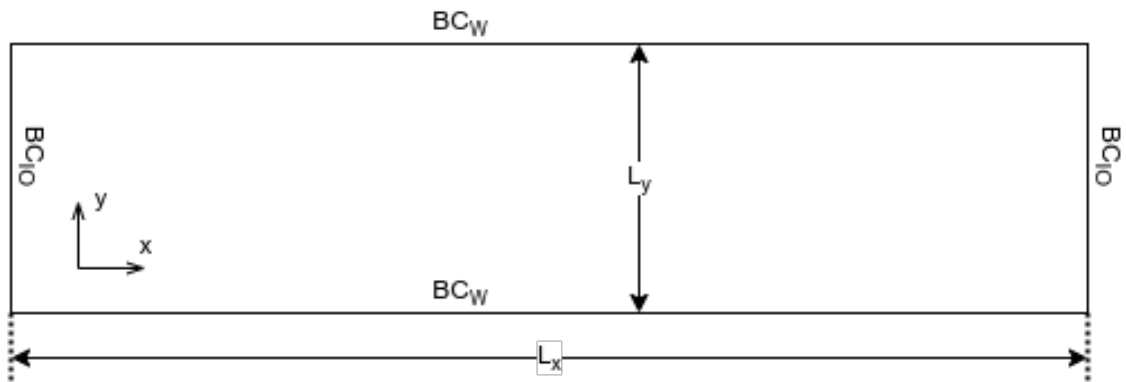


Figure 4.7: Dimensions and boundary conditions for gas curtain simulations.

Olmstead et al. (2017b)) to occur, and for the associated waves to roll-up. Figure 4.8 shows the grid spacing near the gas curtain during the shock passage.

The initial conditions for the simulations in the case of the inclined gas curtain

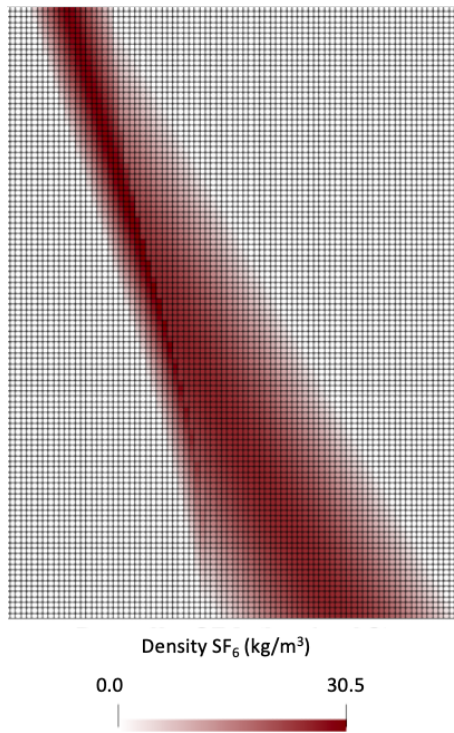


Figure 4.8: Computational grid (every eighth gridline shown) at  $\tau = 0$  for the shock as it passes through an inclined gas curtain.

is shown in Fig. 4.9, colored according to density level. The post-shock area on the left is seen in crimson, and the ambient, pre-shock conditions are seen in white. The curtain of dense gas is located in the pre-shock region. Pressure is uniformly distributed within each of the two regions.

## 4.4.2 Results

### Comparison with the Experiments

Figure 4.10 depicts the interaction of the shock with the gas curtain at various times. The pre-shock curtain is seen in Fig. 4.10a. The time when the shock interaction is halfway down the length of the initial curtain is defined as  $t_0$  which corresponds

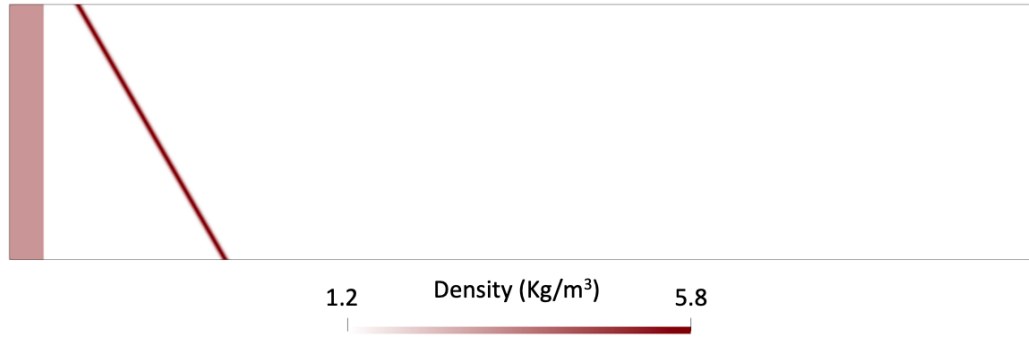


Figure 4.9: Initial conditions used in the simulation of a shock passing through an inclined gas curtain.

to  $\tau = 0$ . At this time (Fig. 4.10b) the shock has begun to change the initial inclination of the curtain. The shock has traveled through the entire curtain by  $\tau = 10.66$  (Fig. 4.10c). The post-shock angle of the curtain is  $\alpha_2 = 13.38^\circ$ . This flow pattern compares well with the pattern seen in the experiments (Fig. 3.3). However, in the experiments at the same Mach number and initial angle, the post-shock angle of the curtain was  $\alpha_2 = 16.91^\circ$ . This discrepancy is mainly due to 3D effects as was found in the 3D simulations and discussed later in chapter 5. Other differences between the simulations and the experiments such as, for example, the approximate representation of the gas concentration, may also contribute.

After the shock has traveled through the entire curtain, an instability can be seen developing near the bottom of the curtain at  $\tau = 25.88$  (Fig. 4.10d). This instability occurs as the curtain is lifted off of the lower wall. The instability continues to propagate upward through the curtain while the foot of the curtain rapidly dissipates. A similar anomaly can be seen at the bottom of the curtain in the experimental study (Fig. 3.3), however, this phenomenon has yet to be investigated in detail experimentally.

At later time  $\tau = 65.46$  a second instability appears in the middle section of the curtain as a group of small-amplitude waves (Fig. 4.10e). In numerical simulations

the onset of this instability occurs later than in experiments, where an instability was observed as early as  $\tau = 15$  (Fig. 3.3). This is also due to 3D effects not present in the current simulations as discussed in chapter 5.

By  $\tau = 88.30$ , both instabilities merge. The combined instability varies in amplitude along the curtain as the wave peaks begin to turn over and roll-up (Fig. 4.10f) similar to what was observed in the experiments (see Fig. 3.4).

### **Additional Flow Features**

Simulations revealed other flow features not observed in the experiments. First, gas from the curtain can be seen spreading horizontally along the upper boundary starting at  $\tau = -7.61$ , immediately after the shock passes the upper part of the curtain. This phenomena was also observed in 3D simulations to a lesser extent.

The vorticity field, which was not observable in experiments, is shown in in Fig. 4.11. The shock deposits positively-signed vorticity on the upstream edge of the gas curtain and negatively-signed vorticity on the downstream edge at early times (Figs. 4.11a and 4.11b). At later times , pairs of oppositely-signed vortices, called dipoles, are seen to form indicating roll-up of the interface (Figs. 4.11c-4.11f). The vorticity pattern along with the growth and roll-up of the center grouping of waves, are consistent with the Kelvin-Helmholtz instability.

### **Effects of Initial Angle**

The effects of initial curtain angle on the resulting wavelength of the instabilities at the interface between  $\text{SF}_6$  and air are discussed in this section. The wavelengths of the Kelvin-Helmholtz instability occurring near the center of the curtain were identified by drawing an axis down the center of the curtain and measuring the half-wavelengths

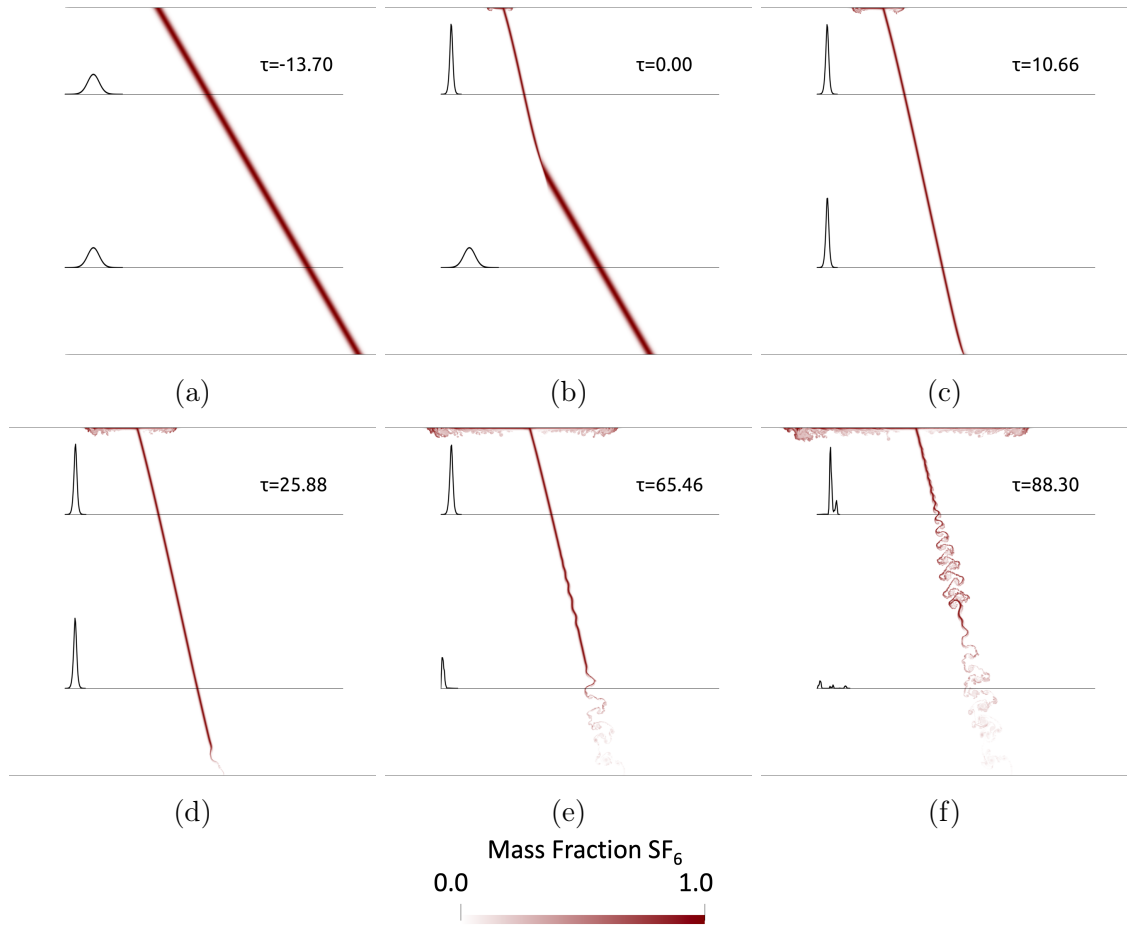


Figure 4.10: Gas curtain concentration at various  $\tau$  with density plots at  $y = 0.25L_x$  and  $y = 0.75L_x$

where the perturbed gas curtain intersected the axis (Fig. 4.12a). Wavelengths were measured at the instant before any additional secondary instabilities appeared on the curtain surface.

Between three and four wavelengths were visible at each curtain angle. The mean wavelength,  $\lambda_{KH}$ , and standard deviation,  $\sigma_{KH}$ , at each curtain angle are shown in Table 4.1 along with the post-shock angle. Figure 4.13a demonstrates that the Kelvin-Helmholtz wavelength does not vary significantly as the initial curtain angle changes.

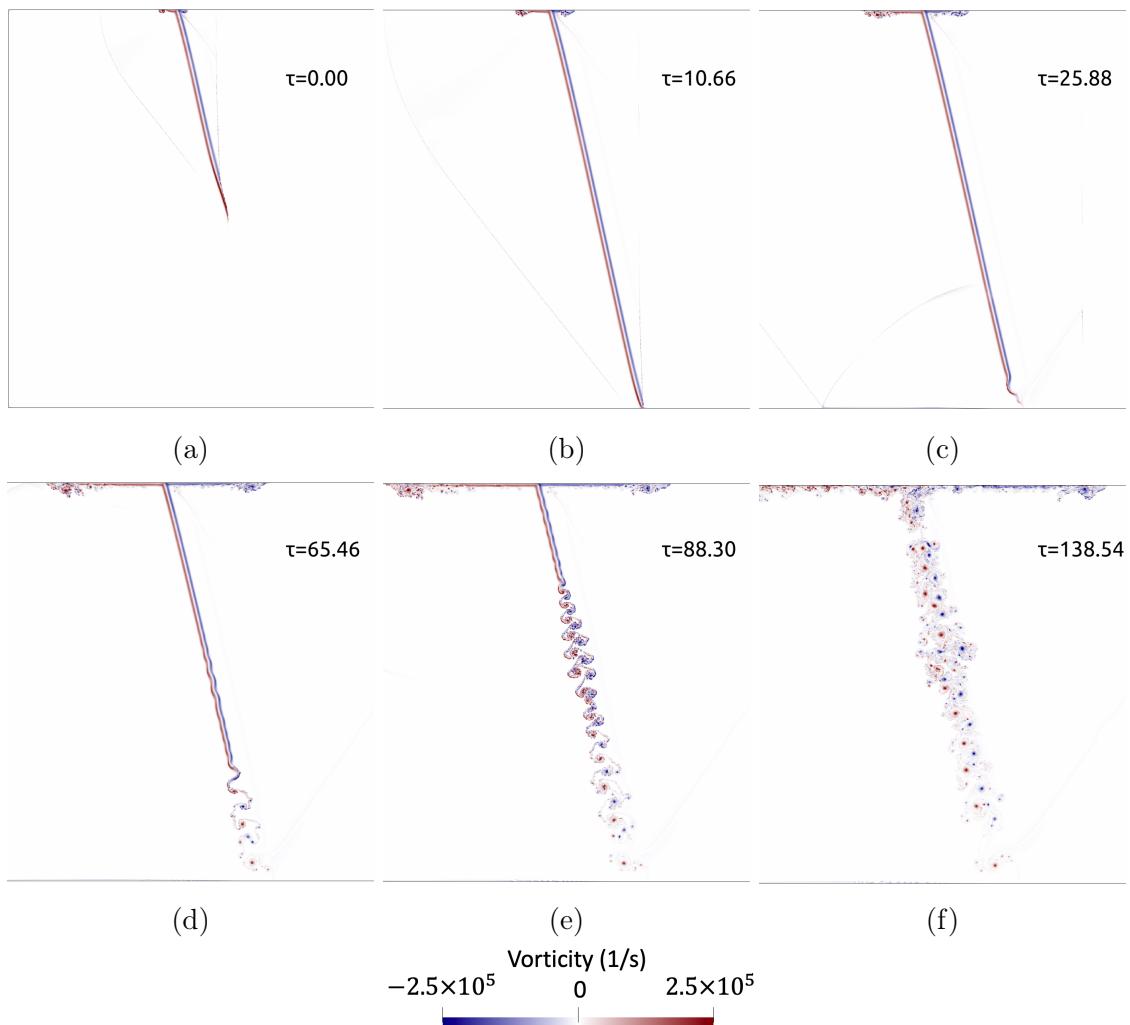


Figure 4.11: Vorticity field at different times with respect to 2D gas curtain evolution.

The wavelength for the instability near the foot of the curtain,  $\lambda_F$  was identified by drawing an axis through the center of the curtain. The size of the first half wave was measured where the gas curtain intersects this axis as shown in Fig. 4.12b. Values of this wavelength are reported in Table 4.1. At each angle, only a single wave near the foot of the curtain was observed due to its rapid dissipation. Similar to the Kelvin-Helmholtz instability, the instability at the foot of the curtain has a weak dependence on the initial curtain angle (Fig. 4.13b).

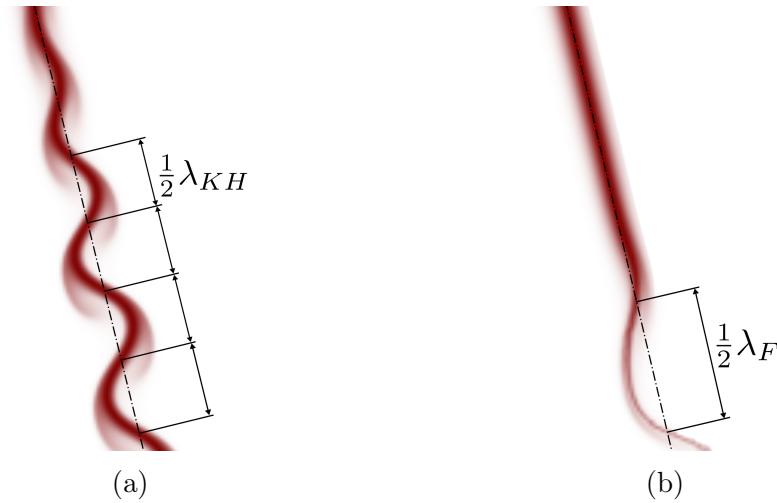


Figure 4.12: Diagram showing the location of (a) The Kelvin-Helmholtz wavelength and (b) the curtain foot wavelength.

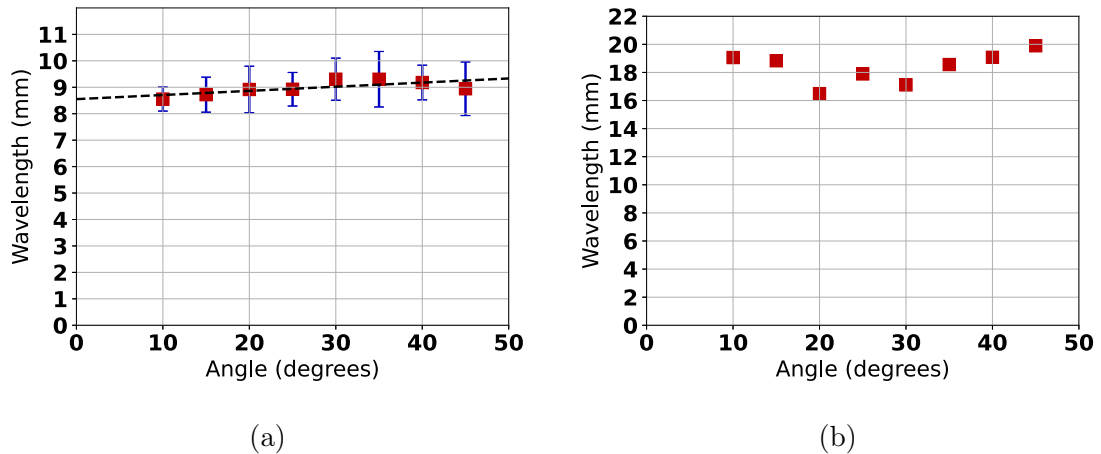


Figure 4.13: Instability wavelength with respect to initial curtain angle for (a) the Kelvin-Helmholtz instability and (b) the instability at the foot of the curtain

### Mach Number Variations

Results of variations in Mach number on the post-shock angle, wavelengths, and the curtain width are presented in this subsection. The mean wavelength,  $\lambda_{KH}$ , and standard deviation,  $\sigma_{KH}$ , at each Mach number are shown in Table 4.2. Data demon-

$\alpha_1$ ( $^\circ$ )	$\alpha_2$ ( $^\circ$ )	$\lambda_{KH}$ (mm)	$\sigma_{KH}$ (mm)	$\lambda_F$ (mm)
10	4.20	8.55	0.45	19.06
15	6.31	8.71	0.61	18.83
20	8.49	8.92	0.88	16.49
25	10.59	8.93	0.63	17.89
30	13.38	9.31	0.80	17.11
35	15.67	9.30	1.05	18.56
40	18.63	9.18	0.66	19.07
45	22.05	8.94	1.01	19.90

Table 4.1: Values of post-shock angle, Kelvin-Helmholtz wavelength and the wavelength at the curtain foot for different initial curtain angles.

strates that the Kelvin-Helmholtz wavelength decreases as Mach number increases, consistent with experimental observations for the tilted gas column (Olmstead et al., 2017b).

Figure 4.14a shows the relationship between Mach number and the ratio of Kelvin-Helmholtz wavelength to initial curtain thickness along with experimental data (Olmstead et al., 2017b). The Kelvin-Helmholtz wavelength is seen to decrease with increasing Mach number and matches closely with the experimental data even at different initial angles.

The wavelength for the perturbation near the foot of the curtain,  $\lambda_F$  was identified by drawing an axis through the middle of the curtain. The size of the first half wave was measured where the gas curtain intersects this axis as shown in Fig. 4.12b. Values of this wavelength are reported in Table 4.2. At each angle, only a single wave near the foot of the curtain was observed due to rapid mixing. The wavelength of the curtain foot perturbation also decreases with the Mach number.

The effect of varying Mach number on the width of the gas curtain over time was also considered. The curtain width  $w$  was measured by fitting a box, inclined to the

$M_1$	$\alpha_2$ ( $^\circ$ )	$\lambda_{KH}$ (mm)	$\sigma_{KH}$ (mm)	$\lambda_F$ (mm)
1.13	25.76	18.61	2.37	37.59
1.40	19.56	12.98	0.84	26.36
1.70	14.86	10.41	0.41	21.28
2.00	13.38	9.31	0.80	17.11

Table 4.2: Values of post-shock angle, Kelvin-Helmholtz wavelength and the wavelength at the curtain foot for different initial angles.

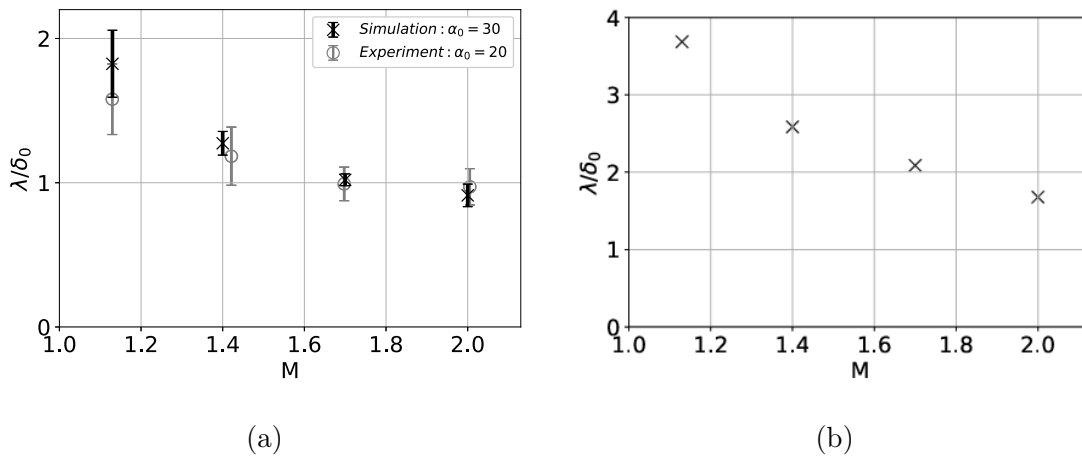


Figure 4.14: Ratio of the wavelength ( $\lambda$ ) to the initial column width ( $\delta_1$ ) with respect to Mach number for (a) the Kelvin-Helmholtz instability and (b) the perturbation at the foot of the curtain. Experimental data in (a) is from Olmstead et al. (2017b).

post-shock angle, around the gas curtain at the location where the Kelvin-Helmholtz instability first appears. Figure 4.15 shows this bounding box for a  $M_1 = 2.0$ ,  $\alpha_1 = 30^\circ$  curtain at  $\tau = 76.88$ .

Figure 4.16 presents the perturbed curtain width evolution over time for different Mach numbers. After the shock passes the curtain at  $\tau = 0$ , the curtain is compressed, with larger Mach numbers compressing the curtain more than smaller Mach numbers. After  $\tau = 60$ , the curtain width begins to grow due to the shock-driven Kelvin-Helmholtz instability. In dimensionless time  $\tau$  the perturbations grow at nearly the same rate, only weakly dependent on the Mach number.

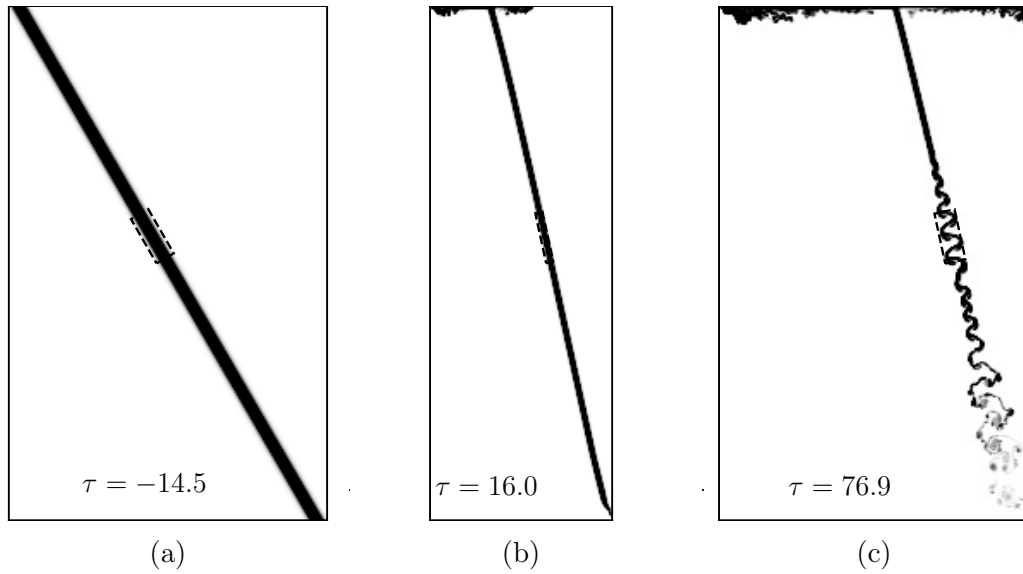


Figure 4.15: Bounding box showing perturbed curtain width at various times for the curtain simulation at  $M_1 = 2.0$ ,  $\alpha_1 = 30^\circ$ : a) the initial uncompressed curtain, b) the compressed curtain after the shock passage, c) perturbations on the curtain surface.

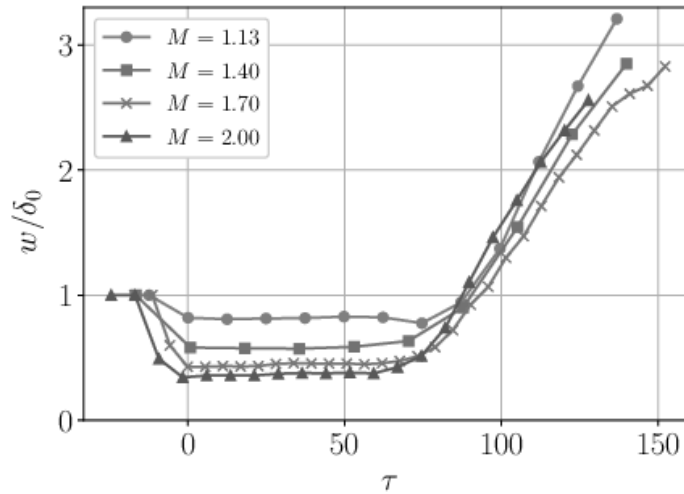


Figure 4.16: SDKHI-induced perturbation width over time for various Mach numbers.

### Effects of Initial curtain Width

Effects of initial curtain width on the post-shock angle, instability wavelengths and post-shock width are discussed in this section. The initial curtain widths were varied from 5.2 mm to 20.8 mm. Table 4.3 shows that values of the post-shock angle remains consistent as initial curtain width changes.

The mean Kelvin-Helmholtz wavelength,  $\lambda_{KH}$ , standard deviation,  $\sigma_{KH}$ , and curtain foot wavelength for each initial width are shown in Table 4.3 along with the post-shock angle  $\alpha_2$ . Both perturbation wavelengths appear to be linearly dependent on initial curtain width. Results are also presented in Fig. 4.17.

Table 4.3: Values of post-shock angle, Kelvin-Helmholtz wavelength and the wavelength at the curtain foot for different initial curtain widths.

$\delta_1$ (mm)	$\alpha_2$ ( $^\circ$ )	$\lambda_{KH}$ (mm)	$\sigma_{KH}$ (mm)	$\lambda_F$ (mm)
5.2	13.38	4.65	0.19	7.55
10.4	13.38	9.31	0.80	17.11
15.6	13.38	12.58	0.75	29.16
20.8	13.38	15.87	2.81	35.82

Figure 4.18 shows the curtain width over time for different Mach numbers. After the shock passes the midpoint of the heavy-gas curtain at  $\tau = 0$ , each curtain is compressed by the same ratio, independent of initial width. The curtains begin to grow at different  $\tau$ , but appear to have similar rates of growth.

## 4.5 Conclusions

The 2D curtain simulations were able to reproduce the Kelvin-Helmholtz instability observed in the experimental study (Olmstead et al., 2017b). A perturbation devel-

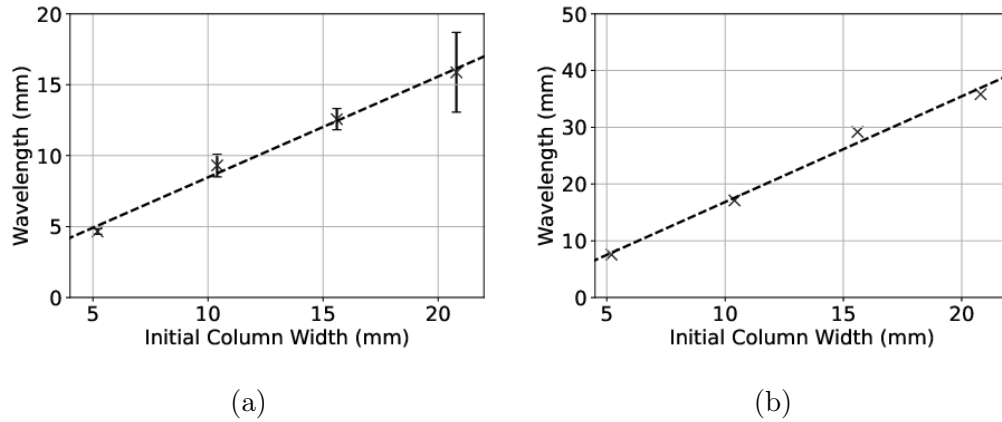


Figure 4.17: Instability wavelength with respect to initial curtain width for (a) the Kelvin-Helmholtz instability and (b) the instability at the foot of the curtain.

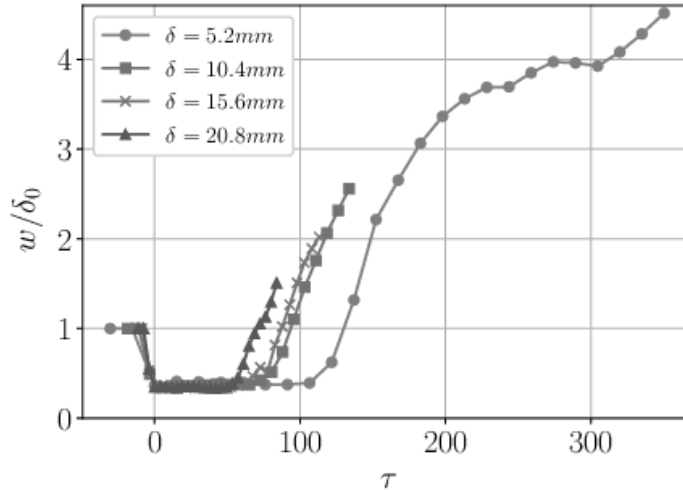


Figure 4.18: Instability width over time for various initial curtain widths.

oping at the foot of the gas curtain after shock passage was also observed which was previously unreported in experiments.

Results from these simulations allowed for the vorticity field to be inspected. The deposition of two lines of oppositely-signed vorticity are consistent with a shear-

#### *Chapter 4. 2D SDKHI Cases*

driven flow like the Kelvin-Helmholtz instability. Wave-like features develop which grow in amplitude at a linear rate and eventually turn over and roll up. This behavior is also consistent with flows that exhibit the Kelvin-Helmholtz instability.

The effects of Mach number, initial angle, and curtain width on the interaction of a shock with an inclined gas curtain were investigated. Changes to the initial curtain angle were found to have no discernible effect on either the Kelvin-Helmholtz wavelength, or the curtain foot instability wavelength. Increasing the Mach number of the shock led to a decrease in the Kelvin-Helmholtz wavelength, consistent with the experimental observations. However, the growth rate of the Kelvin-Helmholtz instability was not affected by variations of Mach number within the considered range of this parameter. The effects of varying curtain width were also studied. Wavelengths of both Kelvin-Helmholtz and curtain foot instabilities were found to be proportional to the initial curtain width, while the post-shock angle of the curtain was constant for different initial curtain widths.

# Chapter 5

## 3D SDKHI Cases

### 5.1 Introduction

This chapter continues the study of SDHKI by conducting and analyzing 3D geometry simulations of a shock interacting with a tilted circular cylinder of dense gas. The goals are to confirm that the code faithfully reproduces experimentally observed flow features in 3D and to gain insight into the flow physics by analyzing numerically modeled features that cannot be tracked with available experimental diagnostics.

Two sets of simulations are performed. The first set of simulations explores the effect of varying Mach number ( $M_1 = 1.4, 1.7, 2.0$ ) and initial column angle ( $\alpha_1 = 10^\circ, 20^\circ, 30^\circ$ ) on the overall flow morphology and the KHI wavelength. Cross-sectional data from the vertical plane (Fig. 1.1) is compared to the 2D shock-curtain simulations in order to study the 3D effects present in the shock-column simulation data. Comparisons are then made to the experimental data of Olmstead et al. (2017b).

The second set of simulations is performed at a higher grid resolution and include

viscosity modeling in order to investigate the effects of initial column angle on the mixing efficiency and other turbulent statistics. These simulations are conducted in a range of initial column angles,  $\alpha_1 = 0^\circ, 1^\circ, 5^\circ, 10^\circ, 30^\circ$  at Mach number equal to 2.0. Energy spectra and anisotropy are also analyzed for each case.

## 5.2 Inviscid Simulations

### 5.2.1 Numerical Setup

The 3D inviscid simulations considered here solve the fully 3D, two-species, Euler equations in their conservation form. These equations consist of the continuity equations for each gas species, equations for each momentum component, and the conservation equation for specific total energy.

$$\frac{\partial}{\partial t} \begin{bmatrix} \rho \\ \rho u \\ \rho v \\ \rho w \\ \rho e_t \\ \rho Y_s \end{bmatrix} + \frac{\partial}{\partial x} \begin{bmatrix} \rho u \\ \rho u^2 + p \\ \rho v u \\ \rho w u \\ (\rho e_t + p)u \\ \rho u Y_s \end{bmatrix} + \frac{\partial}{\partial y} \begin{bmatrix} \rho v \\ \rho v^2 + p \\ \rho w v \\ \rho v w \\ (\rho e_t + p)v \\ \rho v Y_s \end{bmatrix} + \frac{\partial}{\partial z} \begin{bmatrix} \rho w \\ \rho w^2 + p \\ \rho v w \\ \rho w^2 + p \\ (\rho e_t + p)w \\ \rho w Y_s \end{bmatrix} = 0. \quad (5.1)$$

Here,  $\rho$  is the density of the mixture,  $Y_s$  is the mass fraction of  $\text{SF}_6$ ,  $u, v, w$  are velocity components in the  $x, y$ , and  $z$  directions, respectively, where  $x, y$  and  $z$  are the streamwise, spanwise and vertical directions,  $p$  is static pressure, and  $e_t$  is specific total energy.

The pressure of the gas mixture is computed with Dalton's mixing law (Dalton, 1802) and assumes ideal gas behavior:

$$p = \rho (Y_s R_s T + (1 - Y_s) R_a T). \quad (5.2)$$

The mixture temperature is obtained from the internal energy as follows:

$$T = \frac{e_t}{C_{v_{\text{mix}}}}, \quad (5.3)$$

where the mixture specific heat  $C_{v_{\text{mix}}}$  is computed from the species specific heats and mass fractions as:

$$C_{v_{\text{mix}}} = Y_s C_{v,s} + (1 - Y_s) C_{v,a}. \quad (5.4)$$

Expressions for the specific heats of individual species are

$$C_{v,a} = \frac{R_a}{\gamma_a - 1}, \quad C_{v,s} = \frac{R_s}{\gamma_s - 1}. \quad (5.5)$$

The gas constants for each individual species are

$$R_a = \frac{R}{M_a}, \quad R_s = \frac{R}{M_s}, \quad (5.6)$$

where  $R$  is the universal gas constant,  $M_a$  is the molecular weight of air, and  $M_s$  is the molecular weight of  $\text{SF}_6$ .

The code solves fully dimensional equations. The specific values of parameters utilized in the code are,  $R = 8.314462 \frac{\text{J}}{\text{kg}\cdot\text{mol}}$ ,  $M_a = 0.028966 \frac{\text{kg}}{\text{mol}}$ ,  $M_s = 0.14606 \frac{\text{kg}}{\text{mol}}$ ,  $\gamma_a = 1.402$ , and  $\gamma_s = 1.092$ .

## 5.2.2 Domain and Discretization

Figure 5.1 depicts the domain used for the inclined gas column simulations. In this domain,  $L_x = 0.4m \approx 40\delta_1$  is the length of the domain,  $L_y = 0.10m \approx 10\delta_1$  is the height and  $L_z = 0.05m \approx 5\delta_1$  is the width. The heavy-gas column diameter  $\delta_1 = 10.4$  mm is measured at the location where the mass fraction of  $\text{SF}_6$  has a value of 1%. The boundaries at  $x = 0$ ,  $x = L_x$ ,  $z = 0$ ,  $z = L_z$  are inflow/outflow boundaries ( $BC_{IO}$ ). The boundaries at  $y = 0$  and  $y = L_y$  are reflective wall conditions ( $BC_W$ ).

The distribution of  $\text{SF}_6$  gas concentration,  $m_s = \rho_s/\rho$ , across the diameter of the gas column is described by a Gaussian-based distribution with the same parameters as the 2D simulations (see Section 5.2.1).

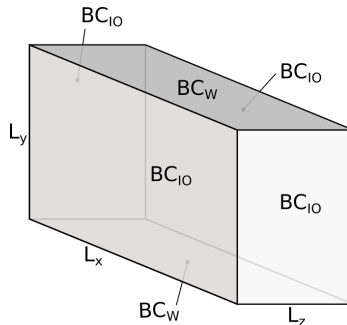


Figure 5.1: The domain dimension and boundary conditions for the inclined gas column simulations.

The simulations use a uniform Cartesian grid with  $dx = dy = dz = 8.0 \times 10^{-5} \text{ m} \approx \delta_1/130$ . This resolution is similar to that used in the shock-cylinder simulations of Palekar et al. (2007). Time step  $dt = 1 \times 10^{-8} \text{ s}$  is chosen resulting in a CFL number  $CFL = 0.1$ , based on the maximum wave speed. The inclined column simulations used a  $5,000 \times 1,250 \times 625$  grid and were computed for 80,000 time steps for a simulation duration of 0.8 ms which was long enough for the shock-driven Kelvin-Helmholtz instability to occur (as seen in Olmstead et al. (2017b)), and for the associated waves to roll-up.

### 5.2.3 Initial Conditions

Solution of Eq. 5.1 requires defining pre-shock and post-shock initial states as well as the initial density distribution in the gas column. In this study, the pre-shock state was defined as atmospheric pressure and room temperature similar to the conditions observed in the experiments of Olmstead et al. (2017b). The post-shock conditions in air were determined from the inviscid normal shock relations:

$$M_2 = \sqrt{\frac{M_1^2 + \frac{2}{\gamma_a - 1}}{\frac{2\gamma_a}{\gamma_a - 1}M_1^2 - 1}}, \quad (5.7)$$

$$\frac{T_2}{T_1} = \frac{1 + \frac{\gamma_a - 1}{2}M_1^2}{1 + \frac{\gamma_a - 1}{2}M_2^2}, \quad (5.8)$$

$$\frac{\rho_2}{\rho_1} = \frac{(\gamma_a + 1)M_1^2}{(\gamma_a - 1)M_1^2 + 2}. \quad (5.9)$$

In Eqs. 5.7-5.9, ambient, or unshocked conditions are indicated with subscript 1. Conditions behind the shock wave, also known as the post-shock conditions are indicated with subscript 2. The Mach number specified in each simulation is the pre-shocked, or ambient Mach number,  $M_1$ .

From these relations, the post-shock conditions  $\rho_2$  and  $T_2$  can be determined. The post-shock velocity is determined by the Mach number and speed of sound;

$$u_2 = M_2 a_2, \quad (5.10)$$

$$a_2 = \sqrt{\gamma RT_2}. \quad (5.11)$$

Finally, the post-shock total specific energy is related to internal energy and kinetic energy by temperature and velocity as:

$$e_{t2} = e_{i2} + e_{KE2}, \quad (5.12)$$

$$e_{i2} = \rho_2 C_v T_2, \quad (5.13)$$

$$e_{KE2} = \frac{1}{2} \rho_2 u_2^2. \quad (5.14)$$

Ambient conditions are  $T_{\text{amb}} = 300\text{K}$  and  $p_{\text{amb}} = 1 \times 10^5\text{Pa}$ .

## 5.2.4 Boundary Conditions

Boundary conditions for Eq. 5.1 include reflective conditions on the top and bottom boundaries of the domain and outflow conditions at the left and right boundaries of the domain.

Inflow/Outflow boundary conditions are defined as:

$$\partial_x \rho(x, t) = 0, \quad \partial_x \rho u(x, t) = 0, \quad \partial_x \rho v(x, t) = 0, \quad \partial_x \rho e_t(x, t) = 0,$$

where  $\partial_x = \frac{\partial}{\partial x}$  and  $\partial_y = \frac{\partial}{\partial y}$  are the derivatives in the x and y directions, respectively.

Reflective boundary conditions are defined as follows:

$$\partial_y \rho(x, t) = 0, \quad \partial_y \rho u(x, t) = 0, \quad \rho v(x, t) = 0, \quad \partial_y \rho e_t(x, t) = 0.$$

## 5.2.5 Results

### Inclined column: Base Case

The initial density distribution in the domain is shown in Fig. 5.2 for the centerline plane and the vertical plane (as defined in Fig. 1.1a). The green region to the left corresponds to the shock wave and post-shock conditions, while the ambient, pre-shock conditions are seen in blue. Pressure is uniformly distributed within each of the two regions. The inclined gas column is seen to the right of the shock in the ambient region. The gas column is inclined at an angle of  $\alpha_1 = 30^\circ$  relative to the shock, similar to the experimental setup in Olmstead et al. (2017b).

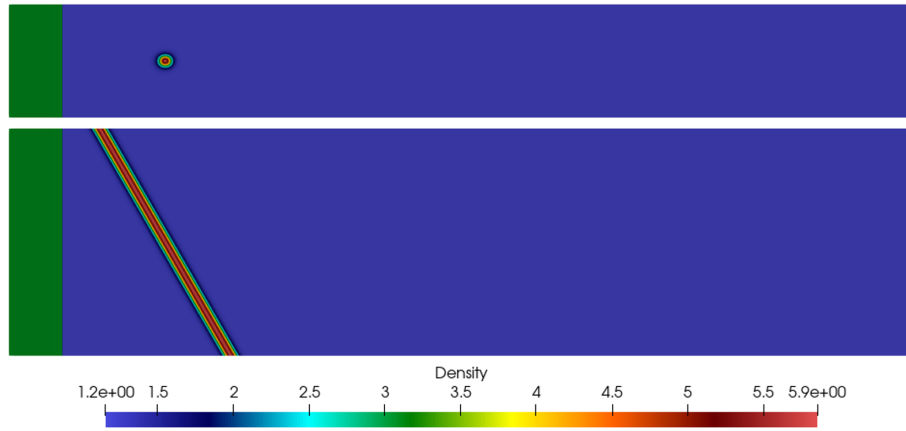


Figure 5.2: Initial conditions of total density in the centerline plane (top) and vertical plane (bottom) used for simulations of a shock interacting with a column of dense gas initially inclined at  $\alpha_1 = 30^\circ$

As the simulation progresses, the shock travels to the right through the heavy-gas cylinder. Figure 5.3 depicts the interaction of the shock with the cylinder at various times. The dimensionless time is defined as  $\tau = kAu_2(t-t_0)$  (Olmstead et al., 2017b). Here  $k = 2\pi/\delta_1$  is the wave number based on the cylinder diameter in experiments

$\delta_1$ ,  $A = (\rho_{sf6} - \rho_{air})/(\rho_{sf6} + \rho_{air})$  is the Atwood number,  $u_2$  is the post-shock velocity, and  $t_0$  is defined as the time when the shock interaction is halfway down the length of the initial column and corresponds to  $\tau = 0$ . At this time the shock has already changed the inclination of the upper half of the column in the plane of the simulation. The shock has traveled through the entire column by  $\tau = 14$ . In addition to the angle change, the gas column starts to move upward along its axis.

At later time,  $\tau = 43$ , perturbations appears near the top of the column. These wavelike perturbations are similar to the Kelvin-Helmholtz waves seen in 2D simulations (Romero et al., 2021a). These perturbations progress down to the foot of the column. As the simulation progresses through  $\tau = 89$ , the wave peaks begin to turn over before the flow undergoes transition ( $\tau = 129$ ).

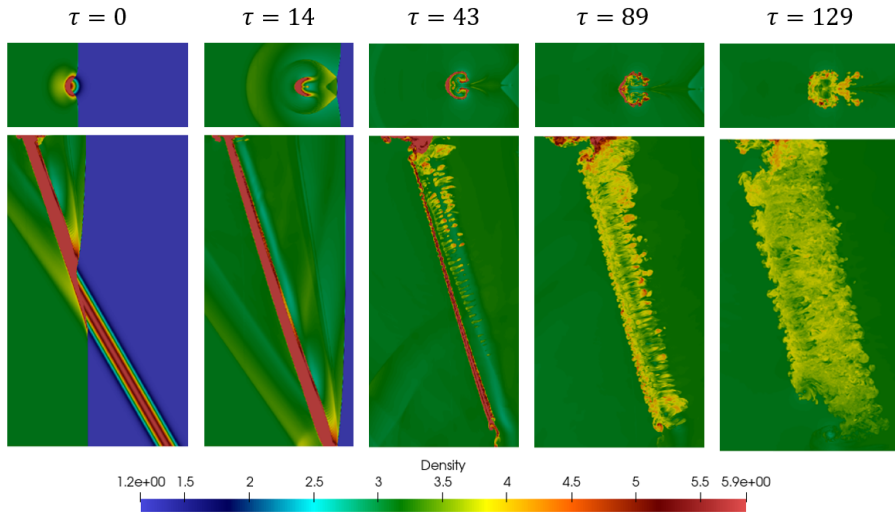


Figure 5.3: Density plots of the centerline and vertical planes at various dimensionless times  $\tau$  for a Mach 2.0 shock interacting with an inclined circular column of heavy gas at an initial angle of  $\alpha_1 = 30^\circ$  to the plane of the shock.

The formation of the Kelvin-Helmholtz waves differs from that of the 2D case presented in chapter 4. The Kelvin-Helmholtz waves are much smaller in length in the 3D case and they form near the top of the column. In the 2D case, the waves

appear first near the column midpoint and at later times (Fig. 5.4). The 3D case also contains flow features downstream of the column. These features are caused by the counter-rotating vortex pair moving material into the vertical plane.

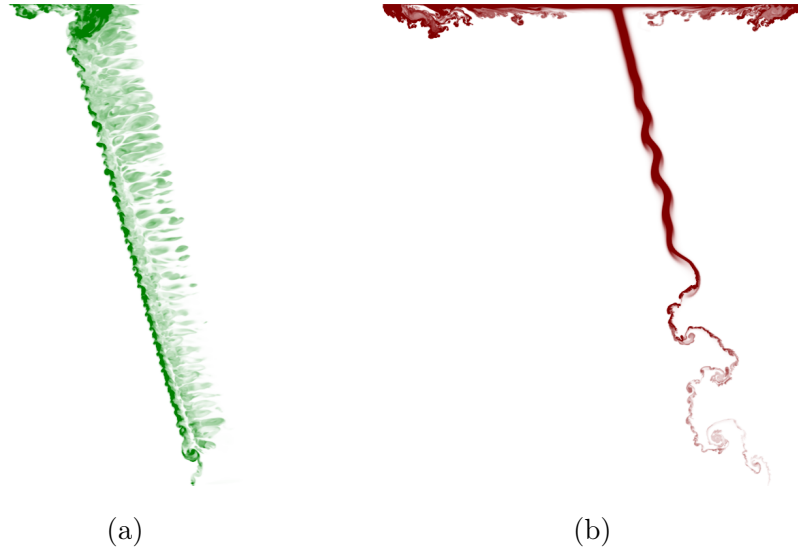


Figure 5.4: Comparison of the Kelvin-Helmholtz waves in the vertical plane of a) the 3D heavy gas column at  $\tau = 38$  and b) a quasi-2D heavy gas curtain from chapter 4. at  $\tau = 86$

### Mach Number and Angle Variations

Results of variations to Mach number and initial column angle are presented in Fig. 5.5. The wavelengths of the Kelvin-Helmholtz instability occurring near the top of the column were identified by measuring the distance between wave peaks. For each case, between five and ten wavelengths were collected. Error bars in the plots below represent one standard deviation in the measured wavelengths. Wavelengths were measured at the latest time before additional secondary perturbations appeared on the column surface. Figure 5.5a shows the relationship between wavelength and Mach number. Just as in the 2D case, wavelength decreases with Mach number. Figure 5.2b depicts the relationship between column angle and wavelength. However, in the

2D case, no relationship was found between initial column angle and the resulting wavelength. In 3D geometry, the wavelength can be seen to decrease with initial column angle, in agreement with experimental data (Fig. 5.5b).

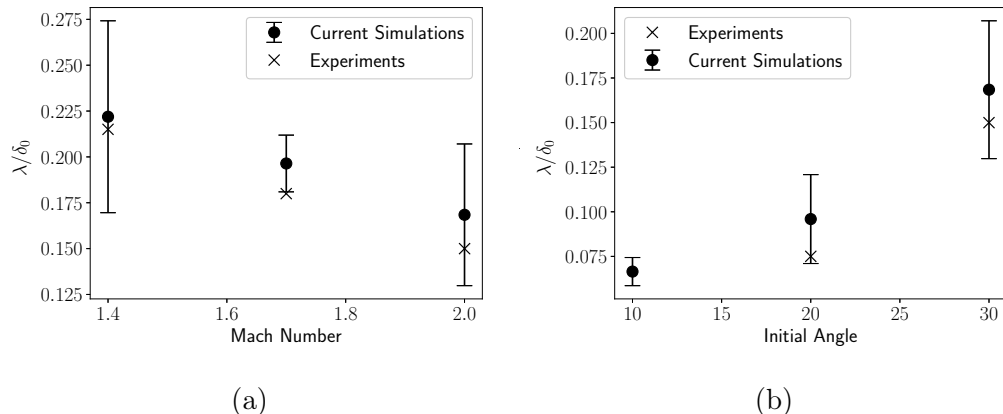


Figure 5.5: Shock-driven Kelvin-Helmholtz wavelengths as a function of a) Mach number  $M_1$  and b) initial column angle  $\alpha_1$ . Error bars represent a 90% confidence interval over all measured waves.

The streamwise extent of the gas column in the centerline plane was also tracked in time. Figure 5.6 depicts the width of the column over the duration of the simulation. Figure 5.6a shows a near linear growth rate in the streamwise extent with higher growth rates for increasing Mach number. Figure 5.6b shows that growth rate does not depend on initial column angle. This growth rate is largely driven by the counter-rotating vortex pair which is established in the centerline plane. The strength of this vortex pair is a function of Mach number only. Thus, the shock-driven Kelvin-Helmholtz instability does not have an effect on the growth rate of the counter-rotating vortex pair.

Figure 5.7 depicts the normalized wavelength using the wavelength selection mechanism theorized in Olmstead et al. (2017b). In their model, Olmstead et al. proposed that the Kelvin-Helmholtz wavelength only depends on the initial column diameter, for a given angle, Mach and Atwood number. Our current simulations

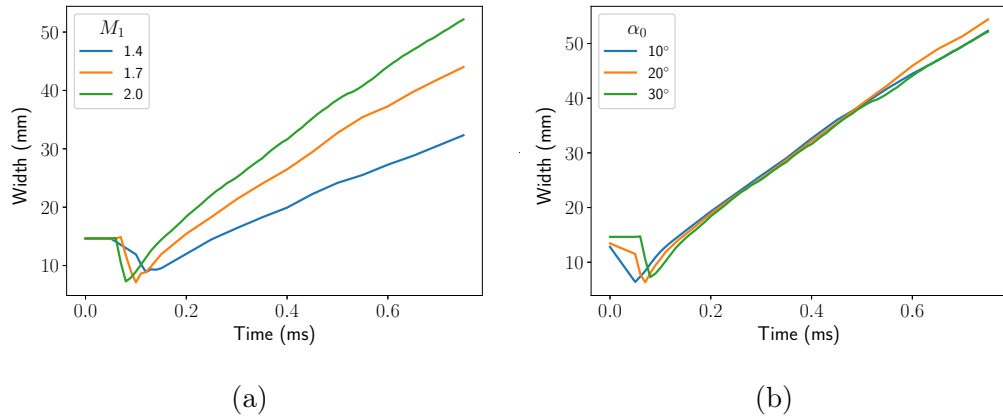


Figure 5.6: Streamwise extent in the centerline plane for various a) Mach numbers  $M_1$  and b) angles  $\alpha_1$ .

support that theory. Using the normalization equation

$$\lambda/[D_c \tan(\alpha_2)M_1^{1/2}A^{1/2}], \quad (5.15)$$

from Olmstead et al. (2017b), where  $\alpha_2$  is the post-shock angle of the column and  $D_c$  is the compressed diameter, produces scaled wavelengths near unity for the each Mach number tested in these simulations. Moreover, the scaled wavelengths match those from experiments.

## 5.2.6 Conclusions

We conducted simulations of the 3D interaction between a planar shock and an inclined cylindrical column of heavy gas. Effects of several parameters (Mach number, column angle) on the growth of the shock-driven Kelvin-Helmholtz instability (SDKHI) were investigated. In particular, the Kelvin-Helmholtz wavelength was found to decrease with increasing Mach number, as suggested by experimental ob-

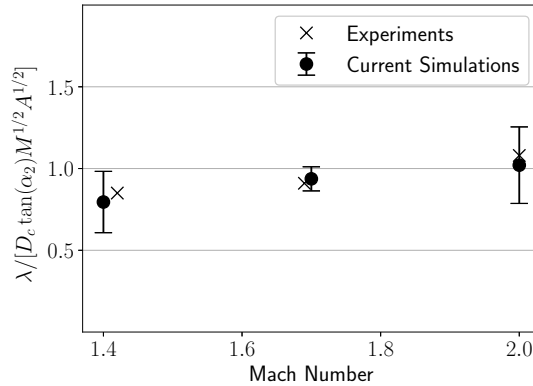


Figure 5.7: SDKHI wavelengths normalized with (5.15).

servations and previous 2D simulations. The effects of varying column angles were also studied. In the 2D case, changes to the initial column angle had no discernible impact on the resulting Kelvin-Helmholtz wavelength. However, in the 3D case, wavelength was found to increase with the angle.

The growth rate of the streamwise extent of the column in the centerline plane was found to increase with Mach number while the initial column angle had no effect. These simulations also support the wavelength-selection mechanism proposed by Olmstead et al. (2017b).

## 5.3 Viscous Simulation

### 5.3.1 Numerical Setup

In this study, results were obtained using the 3D, two-species, compressible, viscous transport equations in their conservation form. These equations consist of the continuity equations for each gas species, equations for each momentum component, and the conservation equation for specific total energy. The resulting system is repre-

sented by the following three equations:

$$\frac{\partial \rho Y_i}{\partial t} + \nabla \cdot (\rho \mathbf{u} Y_i) = 0, \quad (5.16)$$

$$\frac{\partial \rho \mathbf{u}}{\partial t} + \nabla \cdot (\rho \mathbf{u} \mathbf{u} + p \boldsymbol{\delta}) = \nabla \cdot \boldsymbol{\tau}, \quad (5.17)$$

$$\frac{\partial \rho e_t}{\partial t} + \nabla \cdot [(\rho e_t + p) \mathbf{u}] = \nabla \cdot (\boldsymbol{\tau} \cdot \mathbf{u} - \mathbf{q}). \quad (5.18)$$

Here,  $\rho$  is the density of the mixture,  $Y_i$  is the mass fraction of species  $i$  where  $Y_i$  is  $Y_a$  for air and  $Y_s$  for SF<sub>6</sub>,  $\mathbf{u}$  is the 3D velocity vector,  $\mathbf{u} = [u_x, u_y, u_z]$ , where  $x$ ,  $y$  and  $z$  are the streamwise, spanwise, and vertical directions, respectively,  $p$  is static pressure,  $e_t$  is specific total energy,  $\boldsymbol{\tau}$  is the viscous stress tensor, and  $\mathbf{q}$  is the conductive heat flux vector.

The pressure of the gas mixture is computed with Dalton's mixing law (Dalton, 1802) assuming ideal gas behavior:

$$p = \rho (Y_s R_s T + (1 - Y_s) R_a T). \quad (5.19)$$

The mixture temperature is obtained from the internal energy as follows:

$$T = \frac{e_t}{C_{v_{\text{mix}}}}, \quad (5.20)$$

where the mixture specific heat  $C_{v_{\text{mix}}}$  is computed from the species specific heats and mass fractions as:

$$C_{v,\text{mix}} = Y_s C_{v,s} + (1 - Y_s) C_{v,a}. \quad (5.21)$$

Expressions for the specific heats of individual species are

$$C_{v,a} = \frac{R_a}{\gamma_a - 1}, \quad C_{v,s} = \frac{R_s}{\gamma_s - 1}. \quad (5.22)$$

The gas constants for each individual species are

$$R_a = \frac{R}{M_a}, \quad R_s = \frac{R}{M_s}, \quad (5.23)$$

where  $R$  is the universal gas constant,  $M_a$  is the molecular weight of air, and  $M_s$  is the molecular weight of  $\text{SF}_6$ .

The viscous stress tensor  $\boldsymbol{\tau}$  is

$$\boldsymbol{\tau} = 2\mu\mathbf{S} + \frac{1}{3}\boldsymbol{\delta}(\nabla \cdot \mathbf{u}), \quad (5.24)$$

where  $\mu$  is the mixture viscosity computed as  $\mu = Y_a\mu_a + Y_s\mu_s$  and the strain-rate tensor is given by

$$\mathbf{S} = \frac{1}{2} [\nabla\mathbf{u} + (\nabla\mathbf{u})^T]. \quad (5.25)$$

The code solves fully dimensional equations. The specific values of parameters utilized in the code are,  $R = 8.314462 \frac{\text{J}}{\text{kg}\cdot\text{mol}}$ ,  $M_a = 0.028966 \frac{\text{kg}}{\text{mol}}$ ,  $M_s = 0.14606 \frac{\text{kg}}{\text{mol}}$ ,  $\mu_a = 2.928 \times 10^{-5} \frac{\text{kg}}{\text{m}\cdot\text{s}}$ ,  $\mu_s = 1.610 \times 10^{-5} \frac{\text{kg}}{\text{m}\cdot\text{s}}$ ,  $\gamma_a = 1.402$ ,  $\gamma_s = 1.092$ .

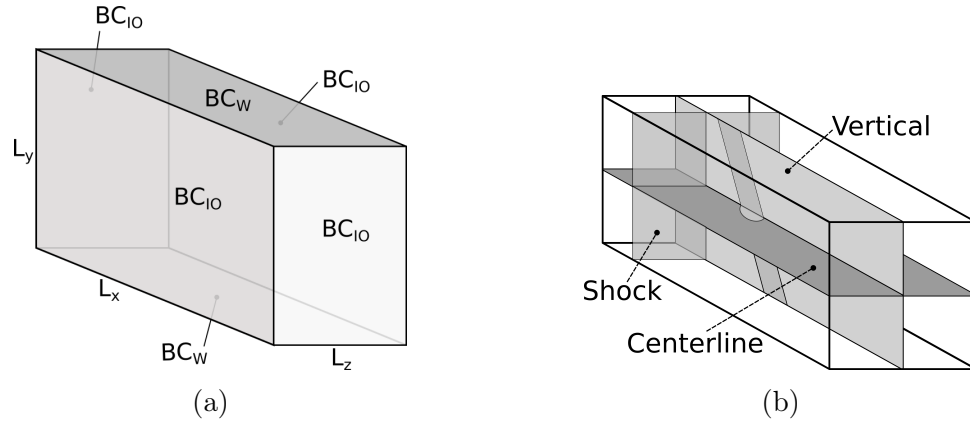


Figure 5.8: a) Domain dimensions and boundary conditions for the inclined gas column simulations, b) illustration of the shock, the gas column, and the key cross-sectional planes.

### 5.3.2 Domain and Discretization

Figure 5.8a depicts the computational domain used for the inclined gas column simulations. In the figure,  $L_x = 0.4m$  is the length of the domain,  $L_y = 0.08m$  is the domain height, and  $L_z = 0.05m$  is its width.

The simulations used a uniform  $10,000 \times 2,000 \times 1,250$  Cartesian grid with  $dx = dy = dz = 4.0 \times 10^{-5}$  m. This resolution exceeds that of the simulations of Palekar et al. (2007) and is similar to those used in Wong et al. (2019) and Groom and Thornber (2019).

The time step  $dt = 1 \times 10^{-8}$  s was chosen so that the CFL number, based on the maximum wave speed, did not exceed 0.1. Simulations were conducted for 80,000 time steps, which is equivalent to 0.8 ms, similar to the experiments of Olmstead et al. (2017b).

### 5.3.3 Initial Conditions

Solution of Eqs. 5.16-5.18 requires defining pre-shock and post-shock initial states. In this study, the pre-shock state was defined as atmospheric pressure and room temperature similar to the conditions observed in the experiments (Olmstead et al., 2017b). The post-shock conditions in air were determined from the inviscid normal shock relations:

$$M_2 = \sqrt{\frac{M_1^2 + \frac{2}{\gamma_a - 1}}{\frac{2\gamma_a}{\gamma_a - 1}M_1^2 - 1}}, \quad (5.26)$$

$$\frac{T_2}{T_1} = \frac{1 + \frac{\gamma_a - 1}{2}M_1^2}{1 + \frac{\gamma_a - 1}{2}M_2^2}, \quad (5.27)$$

$$\frac{\rho_2}{\rho_1} = \frac{(\gamma_a + 1)M_1^2}{(\gamma_a - 1)M_1^2 + 2}. \quad (5.28)$$

In Eqs. 5.26-5.28, ambient, or unshocked conditions are indicated with subscript 1. Conditions behind the shock wave, also known as the post-shock conditions are indicated with subscript 2. The Mach number specified in each simulation is the pre-shocked, or ambient Mach number,  $M_1$ .

From these relations, the post-shock conditions  $\rho_2$  and  $T_2$  can be determined. The post-shock velocity is determined by the Mach number and the speed of sound:

$$u_2 = M_2 a_2, \quad (5.29)$$

$$a_2 = \sqrt{\gamma RT_2}. \quad (5.30)$$

Finally, the post-shock total specific energy is related to the internal energy and the kinetic energy by the temperature and the velocity as:

$$e_{t2} = e_{i2} + e_{KE2}, \quad (5.31)$$

$$e_{i2} = \rho_2 C_v T_2, \quad (5.32)$$

$$e_{KE2} = \frac{1}{2} \rho_2 u_2^2. \quad (5.33)$$

The gas column is positioned ahead of the shock at the angle  $\alpha_1$  to the shock.

The distribution of SF<sub>6</sub> gas concentration,  $m_s = \rho_s/\rho$ , across the diameter of the gas column is described by a Gaussian-based distribution with the same parameters as the 2D simulations (see 5.2.1).

### 5.3.4 Boundary Conditions

Boundary conditions for Eqs. 5.16-5.18 include inflow/outflow boundaries ( $BC_{IO}$ ) at  $x = 0$ ,  $x = L_x$ ,  $z = 0$ ,  $z = L_z$  and the reflective wall conditions ( $BC_W$ ) at  $y = 0$  and  $y = L_y$  as seen in Fig. 5.8a.

$BC_{IO}$  conditions are defined as:

$$\partial_x \rho(x, t) = 0, \quad \partial_x \rho u(x, t) = 0, \quad \partial_x \rho v(x, t) = 0, \quad \partial_x \rho e_t(x, t) = 0.$$

where  $\partial_x = \frac{\partial}{\partial x}$  and  $\partial_y = \frac{\partial}{\partial y}$ .

$BC_W$  conditions are defined as follows:

$$\partial_y \rho(x, t) = 0, \quad \partial_y \rho u(x, t) = 0, \quad \rho v(x, t) = 0, \quad \partial_y \rho e_t(x, t) = 0.$$

### 5.3.5 Results

The initial density distribution in the domain is shown in Fig. 5.9 for the centerline plane and vertical plane (as defined in Fig. (a)). The green region to the left corresponds to the shock wave and post-shock conditions, while the ambient, pre-shock conditions are seen in blue. Pressure is uniformly distributed within each of the two regions. The inclined gas column is seen to the right of the shock in the ambient region. The gas column is inclined at an angle of  $\alpha_1 = 30^\circ$  relative to the shock, similar to the experimental setup in Olmstead et al. (2017b).

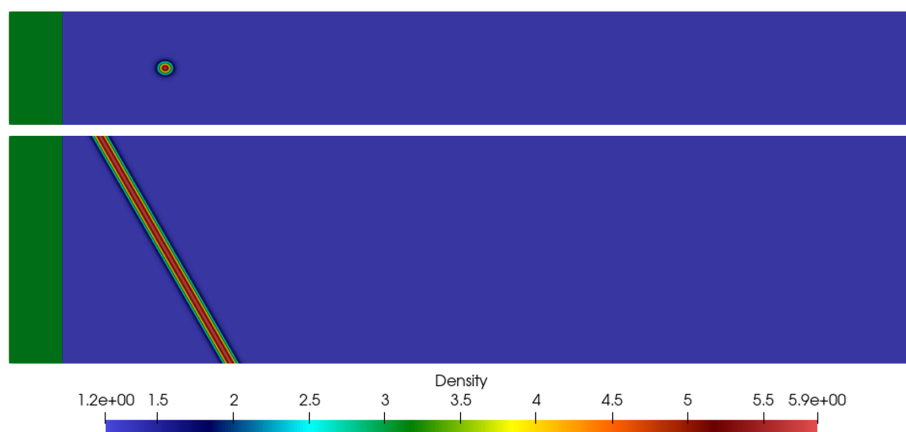


Figure 5.9: Initial conditions of the density in the centerline plane (top) and in the vertical plane (bottom) used for simulations of a shock interacting with the gas column initially inclined at  $\alpha_1 = 30^\circ$

The simulation progresses in the same manner as in the inviscid, low-resolution

simulations described in section 5.2.5. Figure 5.10 shows the flow development over time for the  $\alpha_1 = 30^\circ$  case.

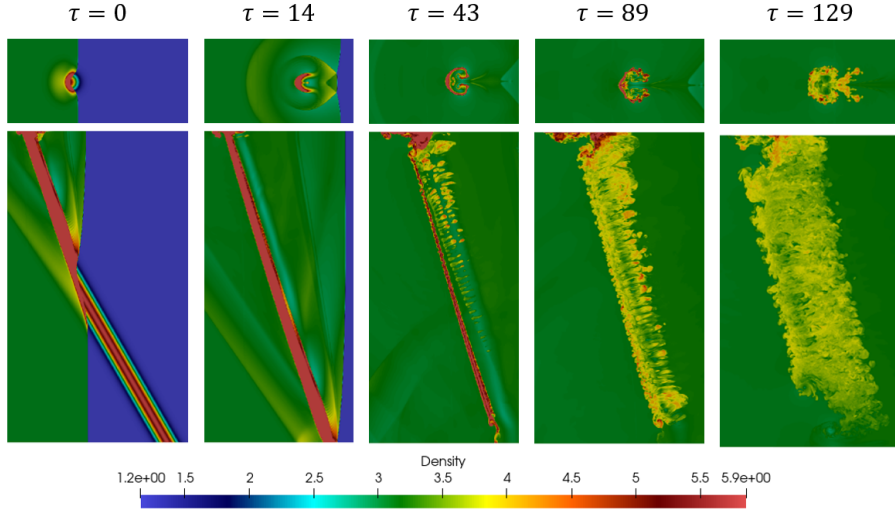


Figure 5.10: Density plots of the centerline and vertical planes at various dimensionless times  $\tau$  for a Mach 2.0 shock interacting with an inclined circular column of heavy gas at an initial angle of  $\alpha_1 = 30^\circ$  to the plane of the shock.

In order to perform a statistical analysis of this flow, a homogeneous sample set is required. There is no flow periodicity in this case. However, the center portion of the column can be assumed to be homogeneous in the direction of the column tilt. For the analysis below, the flowfield was cropped vertically to retain the center third of the column. Horizontally, the domain was cropped to include the area where  $\text{SF}_6$  mass fraction exceeds 0.1%. Figure 5.11 shows the cropped flowfield in the vertical plane for the  $30^\circ$  column at  $\tau = 48.4$ .

The Favre averaging (Favre, 1976) is used when extracting statistics. In this flow representation, the velocity field is decomposed into the mean and fluctuating components:  $u_i = \tilde{u}_i + u_i''$ , where  $\tilde{u}_i = \frac{\langle \rho u_i \rangle}{\langle \rho \rangle}$  is the Favre-averaged mean velocity, and  $u_i''$  is the Favre-averaged velocity fluctuation. The spatial average of a variable  $\phi$  is defined by:

$$\langle \phi \rangle = \frac{1}{N} \sum_i \phi_i, \quad (5.34)$$

where  $N$  is the number of computational cells in the direction of the column tilt, and  $\phi_i$  is the  $i$ th value the variable  $\phi$ . For these simulations,  $N = 650$ .

Profiles are normalized in the streamwise direction as:

$$x^* = \frac{x - x_0}{w}, \quad (5.35)$$

where  $x_0$  is the location of the leading edge of the column and  $w$  is the width of the column defined in section 4.3.2. The statistics below are sampled from the vertical plane as shown in figure 1.1.

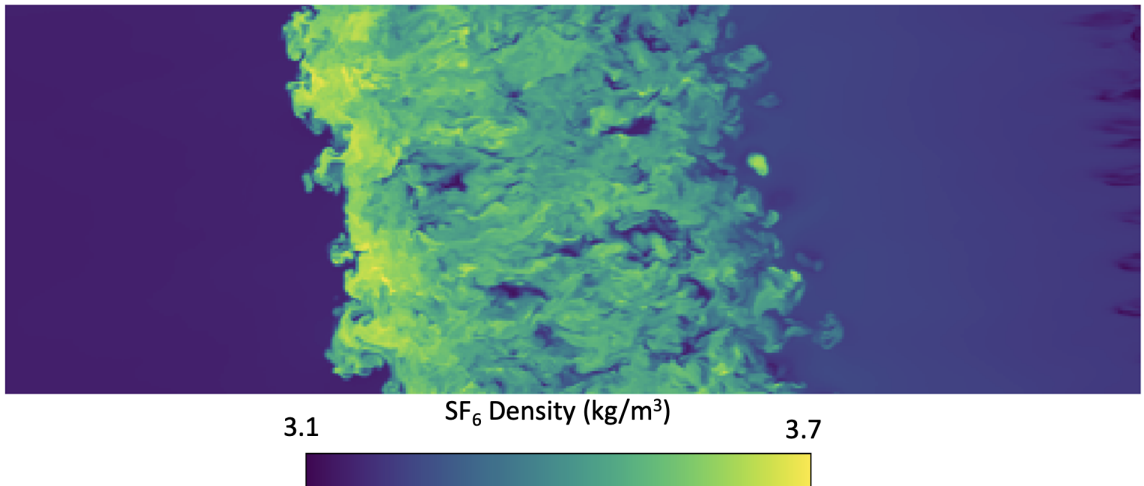


Figure 5.11: Vertical plane slice of the cropped density field for a 30° column at  $\tau = 48.4$ .

### Mean Profiles

Profiles of the mean mass fraction,  $\langle Y_s \rangle$ , and of the mean velocity components,  $\tilde{u}_i$ , were computed at different times in the streamwise direction and are shown in Fig. 5.12. In the figure, the mean velocity components are normalized by the post-shock velocity  $u_{post}$ , defined in section 5.3.3.

Figure 5.12a shows that there is a concentration of SF<sub>6</sub> on the leading edge of the column at early times, which very quickly dissipates as time progresses.

Initially, the streamwise velocity,  $u_1$ , has a lower value in the interior of the column as seen in fig 5.12b. With time, this minimum reduces and shifts towards the leading edge of the column.

The vertical component of velocity,  $u_2$ , behaves in a similar way, with the initial minimum magnitude near the center of the column being reduced and shifted toward the column leading edge. At all x-locations within the column, the values of this velocity component tends to zero with time.

The third velocity component,  $u_3$ , shown in Fig. 5.12d, is close to zero at all locations within the column and at all times. This is due to the column cross-sectional symmetry being preserved with time.

R.M.S. velocity fluctuations and Reynolds shear stresses,  $\frac{\sqrt{R_{ii}}}{u_{post}}$  are presented in Fig. 5.13 where the Favre averaged Reynolds stresses are:

$$\tilde{R}_{ij} = \frac{\langle \rho u_i'' u_j'' \rangle}{\langle \rho \rangle}. \quad (5.36)$$

These figures show that initially, the intensity of all fluctuating velocities and of the shear stresses have the maximum near the center of the column. Over time the peak values of all Reynolds stresses move toward the leading edge of the column

( $x^* = 0$ ). These values at the latest time exceed values at the beginning of the flow development. The trailing edge of the column does not experience significant velocity fluctuations at any time.

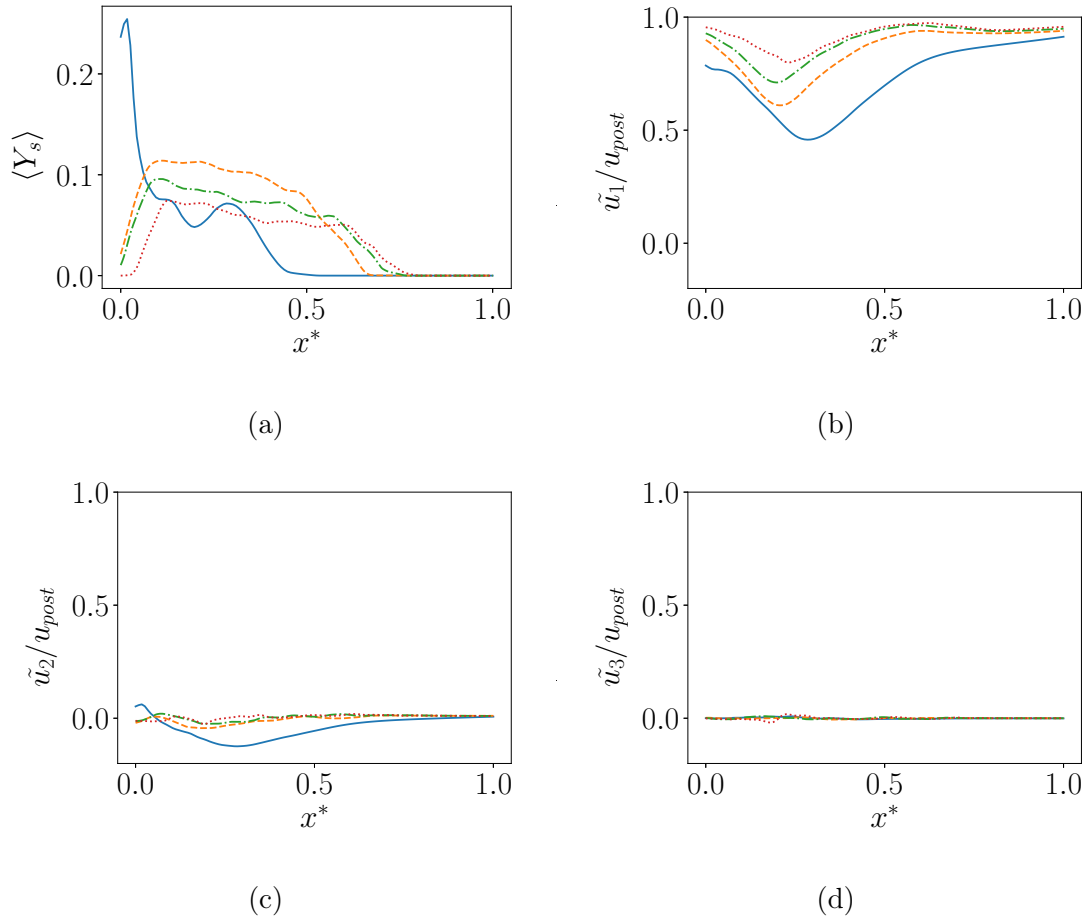


Figure 5.12: Mean mass fraction and mean velocity profiles for a column with an initial tilt of  $\alpha_1 = 30^\circ$  at different times.  $\tau$ : — 12.4, - - 30.4, - · - 48.4, ··· 66.5.

### Anisotropy

In this subsection, the flow anisotropy is studied. For this purpose, the anisotropy tensor is defined as

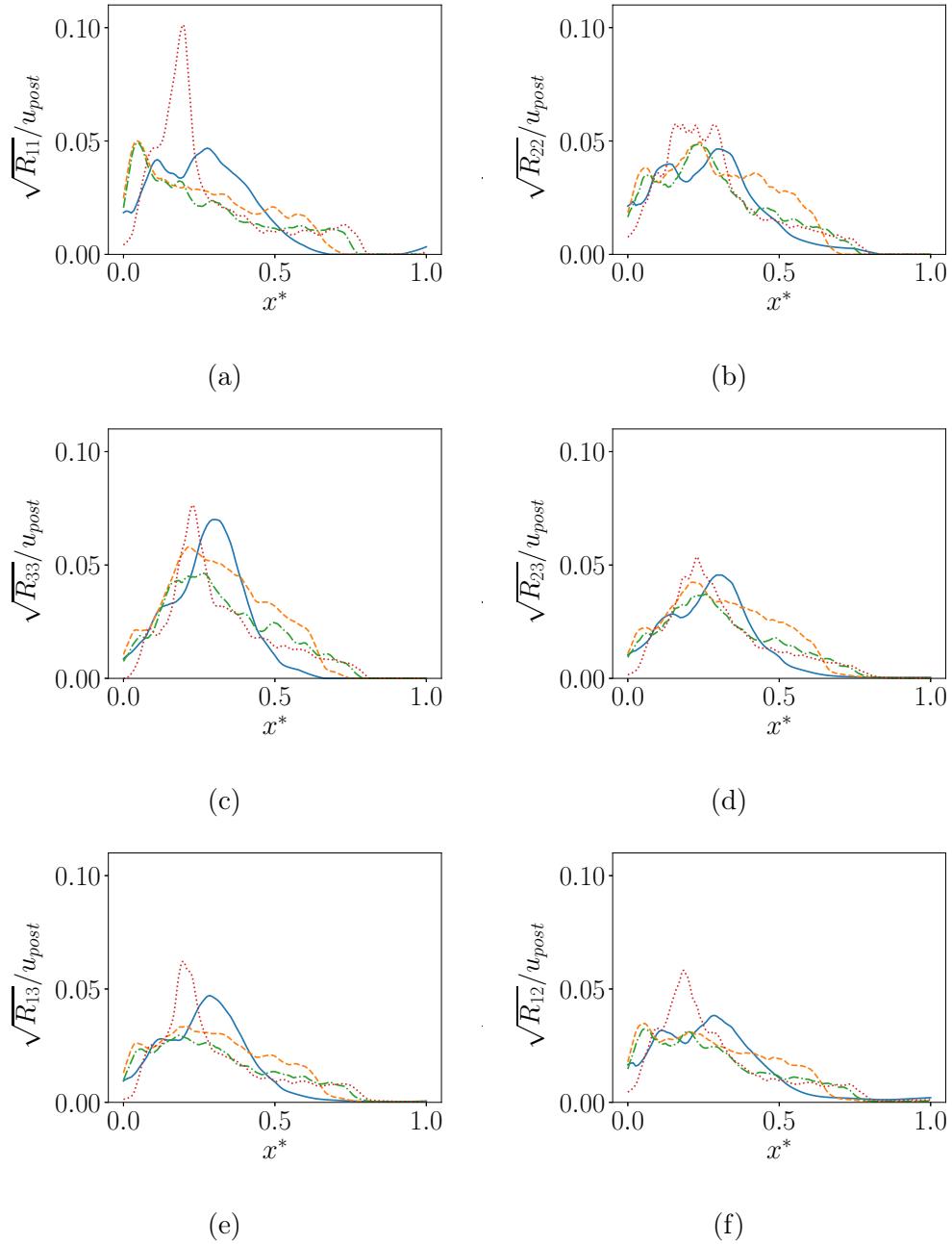


Figure 5.13: R.M.S. velocity and Reynolds shear stress components for a column with an initial tilt of  $\alpha_1 = 30^\circ$  at different times,  $\tau$ , as indicated in fig. 5.12.

$$b_{ij} = \frac{\tilde{R}_{ij}}{\tilde{R}_{kk}} - \frac{1}{3}\delta_{ij}, \quad (5.37)$$

where  $\delta_{ij}$  is the Kronecker delta and  $\tilde{R}_{ij}$  is the Favre-averaged Reynolds stress tensor defined above.

The diagonal components of the anisotropy tensor give an estimate of the contribution of each fluctuating velocity component to turbulent kinetic energy. These values range from  $-1/3$ , corresponding to zero energy from that component to  $2/3$  corresponding to all energy coming from that component. If all three diagonal components of the anisotropy tensor  $b_{ij}$  are zero, then the flow is isotropic.

Figure 5.14 shows diagonal components of the anisotropy tensor for different initial column angles around the same time near the end of the simulation. Turbulent energy is distributed non-uniformly through the column at each angle. For the smaller angles ( $\leq 10^\circ$ ), the flow is anisotropic throughout, dominated by the streamwise component of velocity near the leading and trailing edges of the column, and by the spanwise component in the column interior.

For the  $30^\circ$  column, the energy distribution in the streamwise direction does not change much. However, the vertical component provides most of the turbulent kinetic energy near the column leading edge. The flow becomes more isotropic in the interior of the column, with the transverse and vertical components dominating the turbulent kinetic energy contribution.

### Mixidness

The molecular mixidness ratio over time can also be compared for columns with different initial angles. Molecular mixidness is defined as

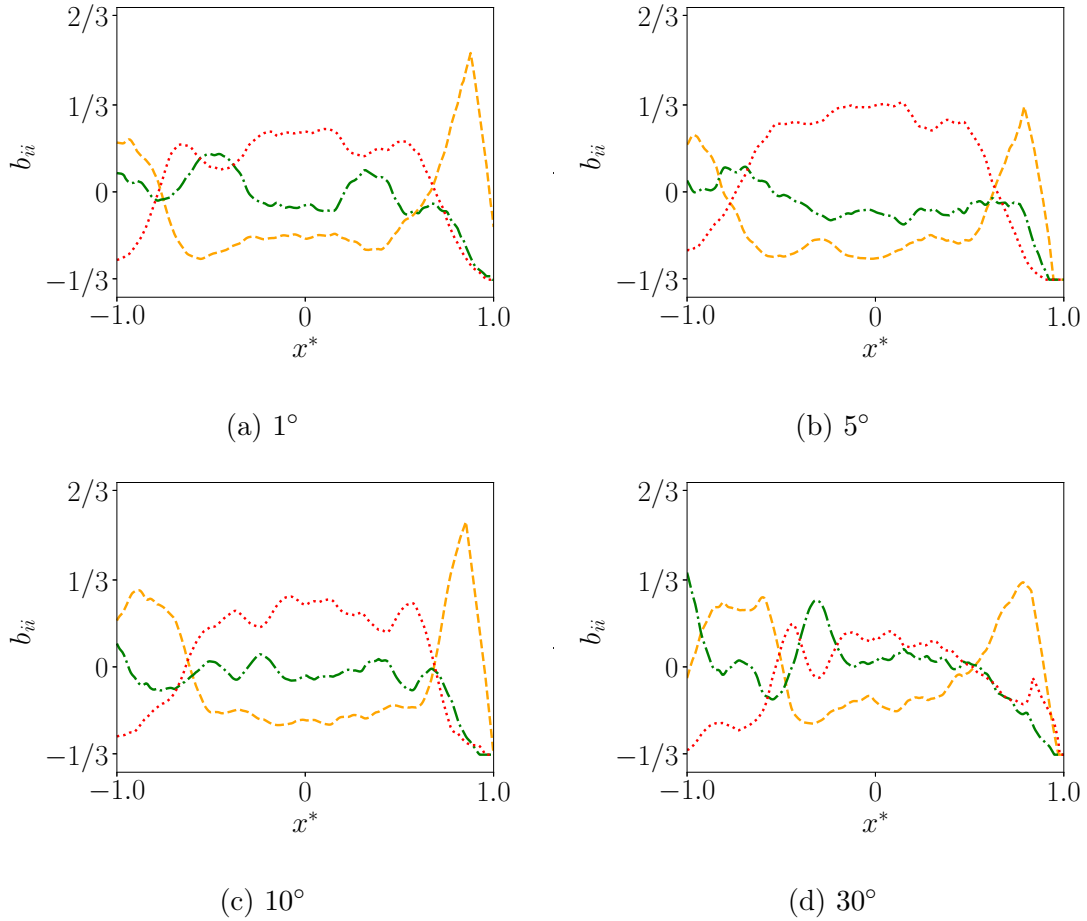


Figure 5.14: Anisotropic tensor components in the vertical plane at different times for columns with initial angles of a)  $1^\circ$ , b)  $5^\circ$ , c)  $10^\circ$  and d)  $30^\circ$ . The components are:  $\text{---} b_{11}$ ,  $\text{-}\cdot\text{---} b_{22}$ ,  $\text{...} b_{33}$ .

$$\theta = \frac{\langle \chi_s(1 - \chi_s) \rangle_V}{\langle \chi_s \rangle_V \langle (1 - \chi_s) \rangle_V}, \quad (5.38)$$

where  $\langle \cdot \rangle_V$  is the volumetric mean defined below, and  $\chi_s$  is the mole fraction of  $\text{SF}_6$ . The mole fraction is given by  $\chi_s = \frac{n_s}{n_s + n_a}$ , where  $n_i = \frac{\rho Y_i}{M_i}$  is the molar count of species ‘ $i$ ’ in a given grid cell with mass fraction  $Y_i$  and molecular mass  $M_i$ . The volumetric mean is defined as

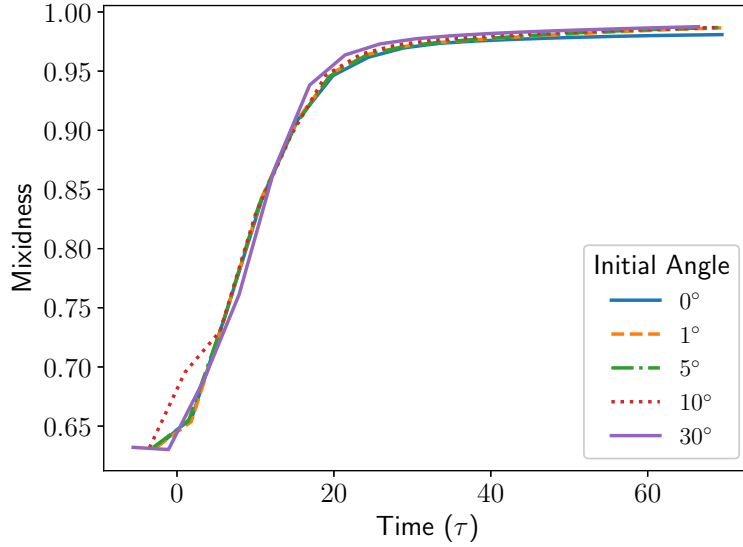


Figure 5.15: Volume mean molecular mixidness ratio of  $\text{SF}_6$  over time for different initial column angles.

$$\langle \phi \rangle_V = \frac{1}{N_x N_y N_z} \sum_i \sum_j \sum_k \phi_{ijk}, \quad (5.39)$$

where  $N_x$ ,  $N_y$  and  $N_z$  are the numbers of grid cells in the x-, y-, and z-directions, respectively,  $\phi_{ijk}$  is the value at the grid cell with coordinates  $(i, j, k)$ .

A value of  $\theta = 1$  means that the flow is completely mixed over the volume, which means that the  $\text{SF}_6$  is uniformly distributed throughout the region.

Figure 5.15 shows the molecular mixidness ratio over time for different initial column angles. For each angle, the column has an initial molecular mixidness of about 0.62 due to the diffuse interface across the column defined by the initial conditions (see fig. 4.1). Over time the mixedness approaches a value of 1 for each initial angle while the initial angle has very little effect on the mixing rate.

### 5.3.6 Conclusions

High-resolution viscous simulations were conducted of the 3D interaction between a planar shock and an inclined cylindrical column of heavy gas. The overall flow morphology was identical to the inviscid case presented in section 5.2. The increased resolution however, allowed more detailed statistics to be collected. Effects of initial column angle on statistical properties of the flow were considered.

The analysis of mean velocity profiles showed that the streamwise velocity component is at maximum near the column edges at all times. The magnitude of the vertical component initially has a maximum in the center of the column, but approaches zero everywhere over time. The spanwise component is close to zero at all times everywhere due to the symmetry of the cross-sectional plane.

The intensity of all fluctuating velocities and of the shear stresses have initially the maximum near the center of the column. Over time, the peak values of all Reynolds stresses move toward the leading edge of the column. These values at the latest time exceed values at the beginning of the flow development. The trailing edge of the column does not experience significant velocity fluctuations at any time.

Analysis of the anisotropy tensor shows that turbulent kinetic energy is non-uniformly distributed through the column. At larger column angles, turbulence tends towards to isotropy in the column interior in the  $y$ - and  $z$ -directions mainly.

Analysis of the mixidness over time showed that the initial angle has very little effect on the mixing rate of the flow and that with time, the mixidness tends to a value of 1, that is, to uniform distribution of the gas in the column.

# Chapter 6

## The FIESTA Particle Extension

### 6.1 Introduction

In this section, the interaction of a shock wave with a curtain of solid particles is examined in 3D simulations. Such flows are of interest for many practical applications. For example, spacecraft (Poovathingal and Chen, 2021) and hypersonic aircraft (Mehta and Levin, 2019) travelling at supersonic speeds create a bow shock interacting with dust particles in the atmosphere. Industrial applications and safety measures such as thermal spray coating (Dolatabadi et al., 2004) and blast mitigation techniques (Hadjadj and Sadot, 2013) also utilize shock-particle interactions. These interactions occur in natural phenomena as well including volcanic eruptions (Woods et al., 1996) and astrophysical processes such as the ejection of stellar dust from supernovae (Silvia et al., 2012).

Multi-phase compressible flows, including those that involve shock-particle interactions can be simulated using either Euler-Euler or Euler-Lagrange approaches. With the Euler-Euler approaches, the particle phase is modelled as an additional continuous phase similar to the base gas (Ching et al., 2020; Dolatabadi et al., 2004).

This poses difficulties for flows with a low-volume fraction of particles or flows with large diameter particles. The discrete element method (DEM) (Tavarez and Plesha, 2007) is a more accurate Euler-Lagrange approach in which the particle geometry is taken into account. With this method, the boundary layer over the particle can be resolved and additional effects can be considered including the rotational degrees of freedom and surface roughness. However, this method is impractical for systems with a large number of small particles. Another Euler-Lagrange method, the point-particle method (PPM) (Herrmann, 2010), represents the particles as point masses which are transported through the flow. This method more efficiently describes the behavior of a large number of particles compared to DEM. However, PPM requires closure models to account for the sub-grid interaction of the particle-phase with the Eulerian fluid phase. Sub-grid coupling models can be developed from experimental studies (Boiko et al., 1997) or from the particle-resolved simulations with a small numbers of particles (Akiki et al., 2017; Sen et al., 2018).

Recent advances in GPU computing combined with PPM make it possible to simulate shock-particle interactions with highly resolved base flows and with a large number of particles (Stantchev et al., 2008; Bird et al., 2021). This is the approach used in the current work to study 3D effects of shock interaction with a finite-width ( $w_d = 22.7\text{mm}$ ) curtain of particles. In this approach (hereafter, the PPM/WENO method), a fifth-order WENO scheme (Jiang and Shu, 1996) for particle transport is coupled with a simple momentum exchange model for two-way fluid coupling (Ching et al., 2020).

To examine the computational efficiency and accuracy of this method, three dimensional simulations have been conducted with a Mach 2.5 shock propagating through a finite-width curtain of particles with volume fractions  $\alpha_d = 1\%, 5\%, 10\%$ . Results of simulations are then compared with experimental data from Theofanous et al. (2016).

Performance and scaling data are also collected for one- and two-way coupled schemes on CPU and GPU architectures to compare execution time and speedup for various numbers of particles.

Section 6.2 describes the problem geometry and initial conditions followed by the code description and numerical methodology in sections 6.4 and 6.3, respectively. Numerical results are compared against experimental data in section 6.5 and computational performance metrics are presented in section 6.6.

## 6.2 Numerical Setup

### 6.2.1 Domain

The following simulations are conducted on a domain with a square cross-section ( $200\text{mm}\times 200\text{mm}$ ) identical to the shock-tube facility used in Theofanous et al. (2016). The length of the domain (as depicted in Fig. 6.1) is chosen to be 4m in order to sample pressure at the same locations as the pressure transducers are placed in Theofanous et al. (2016) (Fig. 6.2). This domain length also prevents spurious reflections from the upstream and downstream boundaries over the duration of the simulations. The upstream and downstream boundaries are modelled as free-flow conditions ( $BC_{IO}$  in Fig. 6.1) using an odd extension of the flow parameters into a set of ghost cells outside the physical domain. The remaining four boundaries are modelled as reflective slip-wall conditions ( $BC_W$  in Fig. 6.1) to represent the shock-tube surfaces. Figure 6.1 also shows the relative locations of the initial shock and particle curtain.

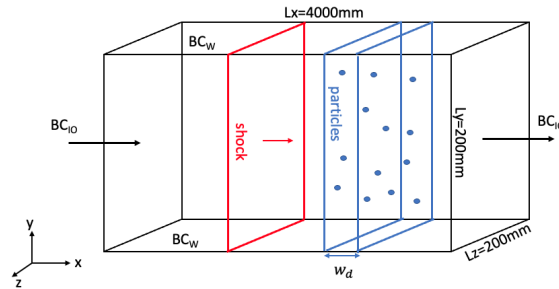


Figure 6.1: Boundary conditions and domain dimensions.

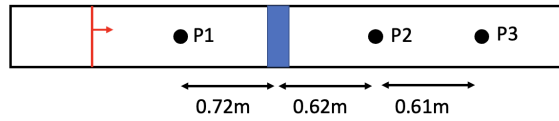


Figure 6.2: Location of pressure sensors in experiments of Theofanous et al. (2016).

## 6.2.2 Spatial and Temporal Discretization

Simulations used a uniform Cartesian grid. It was observed that a packed particle volume ratio of  $\beta > 0.3$  produced numerical instabilities in the Eulerian fluid solver. The packed particle volume ratio is defined as  $\beta = V_c/V_d$ , where  $V_c$  is the cell volume and  $V_d$  is the total volume of all particles in that cell. By limiting the initial particle volume fraction to  $\alpha_d = 10\%$  and the cell dimensions to  $dx = dy = dz = 1mm$  the packed particle volume ratio did not exceed this limit. The total number of grid cells was therefore  $4,000 \times 200 \times 200$ . A timestep of  $dt = 1 \times 10^{-7}$  was chosen such that the CFL number based on the maximum wave speed is  $CFL = 0.1$ .

## 6.2.3 Initial Conditions

Initial conditions for this problem require defining the pre-shock and post-shock states as well as the initial particle distribution throughout the curtain. Ambient, or unshocked conditions are indicated with subscript 1 while conditions behind the

Chapter 6. The FIESTA Particle Extension

shock wave, also known as the piston conditions or shocked conditions, are indicated with subscript 2. The pre-shock state is defined as Helium gas at standard temperature and pressure of  $P_1 = 1$  bar and  $T_1 = 298.15$  K. The Mach number specified in each simulation is the pre-shock, or ambient Mach number,  $M_1$ . The post-shock conditions were determined from the inviscid normal shock relations as follows:

$$M_2 = \sqrt{\frac{M_1^2 + \frac{2}{\gamma-1}}{\frac{2\gamma}{\gamma-1}M_1^2 - 1}}, \quad (6.1)$$

$$\frac{T_2}{T_1} = \frac{1 + \frac{\gamma-1}{2}M_1^2}{1 + \frac{\gamma-1}{2}M_2^2}, \quad (6.2)$$

$$\frac{\rho_2}{\rho_1} = \frac{(\gamma + 1)M_1^2}{(\gamma - 1)M_1^2 + 2}. \quad (6.3)$$

From these relations, the post-shock conditions can be determined by  $\rho_2 = \frac{\rho_2}{\rho_1}\rho_1$  and  $T_2 = \frac{T_2}{T_1}T_1$ . The momentum components can be computed from the velocity,  $\rho u$ , where velocity is determined by the Mach number and the speed of sound:

$$u_2 = M_2 a_2, \quad (6.4)$$

$$a_2 = \sqrt{\gamma R T_2}. \quad (6.5)$$

Finally, total specific energy in the post-shock region is related to internal energy

and kinetic energy by temperature and velocity:

$$e_t = e_i + e_{\text{KE}}, \quad (6.6)$$

$$e_i = \rho C_v T, \quad (6.7)$$

$$e_{\text{KE}} = \frac{1}{2} \rho u^2. \quad (6.8)$$

The particles are distributed uniformly throughout the volume of the curtain. The particle diameters are also distributed uniformly with a minimum diameter of 0.86mm and a maximum diameter of 0.96mm as in Theofanous et al. (2016). The number of particles is computed by dividing the particle volume fraction by the average diameter of the particles such that

$$n_d = \frac{L_y L_z w_d \alpha_d}{4/3 \pi r_d^3}, \quad (6.9)$$

where  $r_d = D_d/2$  is the particle radius. The particle count  $n_d$  is rounded down to the nearest integer.

## 6.3 Governing Equations

### 6.3.1 Fluid Phase Euler Solver

The current study employs a coupled Euler-Lagrange solver for particle laden flows. The Euler solver comprises the 3D two-species, inviscid Euler equations in their

Chapter 6. The FIESTA Particle Extension

conservative form with a source term to couple the momentum and energy equations to the Lagrangian particle solver. These equations consist of the continuity equations for each gas species, equations for each momentum component, and the conservation equation for specific total energy. The resulting system is represented by the following vector equation:

$$\frac{\partial}{\partial t} \begin{bmatrix} \rho \\ \rho u \\ \rho v \\ \rho w \\ \rho e_t \end{bmatrix} + \frac{\partial}{\partial x} \begin{bmatrix} \rho u \\ \rho u^2 + p \\ \rho v u \\ \rho w u \\ (\rho e_t + p)u \end{bmatrix} + \frac{\partial}{\partial y} \begin{bmatrix} \rho v \\ \rho v u \\ \rho v^2 + p \\ \rho w v \\ (\rho e_t + p)v \end{bmatrix} + \frac{\partial}{\partial z} \begin{bmatrix} \rho w \\ \rho w u \\ \rho v w \\ \rho w^2 + p \\ (\rho e_t + p)w \end{bmatrix} = \begin{bmatrix} 0 \\ S_1 \\ S_2 \\ S_3 \\ S_e \end{bmatrix} \quad (6.10)$$

Here,  $\rho$  is the density,  $u, v, w$  are velocity components in the  $x, y$ , and  $z$  directions, respectively, where  $x$  and  $y$  are stream-wise and span-wise directions,  $p$  is static pressure and  $e_t$  is specific total energy. The momentum and energy source terms are obtained from the Lagrangian particle solver and denoted as  $S_m$  and  $S_e$ , where  $m = 1, 2, 3$ . Pressure is computed assuming the ideal gas behavior:

$$p = \rho R_h T. \quad (6.11)$$

Temperature is obtained from the internal energy with the expression,

$$T = \frac{e_t}{C_v}. \quad (6.12)$$

The specific heat  $C_v$  and gas constant are computed as follows:

$$C_v = \frac{R_h}{\gamma_h - 1}, \quad (6.13)$$

$$R_h = \frac{R}{M_h}, \quad (6.14)$$

where  $R$  is the universal gas constant and  $M_h$  is the molecular weight of helium.

### 6.3.2 Particle Phase Lagrangian Solver

The Lagrangian particle solver implements a point-particle method similar to the method described in Ching et al. (2020). Particles are modelled as smooth, solid spheres of constant diameter  $D$ . Only translational degrees of freedom are considered and the effects from particle-particle collisions and rotation are not modelled. The following equations define the particle position  $\mathbf{X} = (x, y, z)$ , momentum  $m_d \mathbf{u}_d$  and temperature  $T_d$ , where  $\mathbf{u}_d = (u_d, v_d, w_d)$  is the particle velocity:

$$\frac{d\mathbf{x}_d}{dt} = \mathbf{u}_d, \quad (6.15a)$$

$$m_d \frac{d\mathbf{u}_d}{dt} = \mathbf{F}, \quad (6.15b)$$

$$m_d c_d \frac{dT_d}{dt} = Q, \quad (6.15c)$$

Particle quantities are denoted with the subscript "d" while the base flow properties do not have subscripts.

Chapter 6. The FIESTA Particle Extension

The particle velocity  $\mathbf{u}_d$  is computed by interpolating the base flow velocity field to the particle position  $\mathbf{x}_d$  with a cubic interpolation scheme. The drag force on the particle  $\mathbf{F}_d$  and heat transfer  $Q_d$  are computed with the following expressions:

$$\mathbf{F} = \frac{1}{8}\pi D_d^2 \rho (\mathbf{u} - \mathbf{u}_d) |\mathbf{u} - \mathbf{u}_d| C_D, \quad (6.16a)$$

$$Q = \pi D_d \kappa (T - T_d) Nu, \quad (6.16b)$$

where  $D_d$  is the particle diameter,  $C_D$  is the particle drag coefficient,  $\kappa$  is the thermal conductivity of the base fluid and  $Nu$  is the Nusselt number.

The particle quantities can then be used to construct the source terms for the base flow with the following expressions for momentum and energy:

$$\mathbf{S}_m = - \sum_{p=1}^{N_d} \mathbf{F}_i \mathbf{x}_{d,i}, \quad (6.17a)$$

$$S_e = - \sum_{i=1}^{N_d} (Q_i + \mathbf{u}_{d,i} \cdot \mathbf{F}_i) \mathbf{x}_{d,i}. \quad (6.17b)$$

Advective terms in the base flow equations are approximated with the simplified 5th-order weighted essentially non-oscillatory (WENO5) finite difference scheme (Ramani et al., 2019a,b; Jiang and Shu, 1996). The pressure gradient term is approximated using a fourth-order central difference (Ramani et al., 2019a,b). The Eulerian and Lagrangian regimes are solved simultaneously with a low-storage, second-order, explicit Runge-Kutta integrator (Williamson, 1980).

## 6.4 Code Description

The FIESTA Particle Extension (FIESTApx) is a modular extension to FIESTA developed at Los Alamos National Laboratories which provides Lagrangian particle transport and fluid-particle coupling functionality within the FIESTA framework. FIESTApx uses a second-order interpolation scheme to map the Eulerian velocity field to the Lagrangian particles. The Henderson drag model (Henderson, 1976) is then used to compute particle drag coefficients. The particle equations of motion 6.15 are solved with a second-order Runge-Kutta solver along with the fluid equations 6.10.

## 6.5 Validation Results

Figure 6.3 compares the upstream and downstream fronts of the particle curtain to the experimental data from Theofanous et al. (2016). In their experiments, particle curtain volume fractions of 40% were measured. This particle volume fraction could not be achieved in the current simulations because it was observed that a packed particle volume ratio of  $\beta > 0.3$  produced numerical instabilities in the Eulerian fluid solver. For this reason, the maximum packed particle volume ratio  $\beta$  is restricted in our simulations by limiting the initial particle volume fraction to  $\alpha_d = 10\%$ .

Regardless these differences in the experiments and the simulations, the curtain fronts obtained in the simulations closely match those in the experiments as demonstrated in Fig. 6.3.

Figure 6.4 shows the pressure traces for each volume fraction over the simulation duration. Pressure traces are labeled as P1, P2 and P3 and their locations are depicted in fig. 6.2. Pressure trace P1 is the upstream pressure trace and shows the pressure history of the initial and reflected shocks. Pressure traces P2 and P3 are

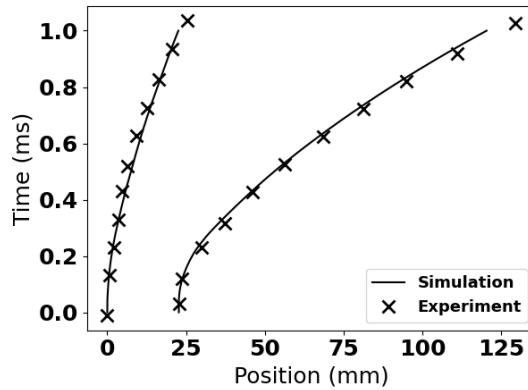


Figure 6.3: Upstream and downstream edges of the particle curtain over time compared to experiments (Theofanous et al., 2016).

located downstream of the curtain and show pressure traces of the transmitted shock. The  $\alpha_d = 1\%$  volume fraction pressure trace (Fig. 6.4a) shows a weak reflected shock, while volume fractions of 5% and 10% (Figs. 6.4b and 6.4c) more closely reproduce the pressure ratios observed in experiments.

The reflected shock strength can be measured by taking the maximum value of the pressure trace recorded at P1 in fig. 6.4. The strength of the reflected shock obtained in this way closely match those observed in the experiments despite the lower volume fractions used in the simulations. Table 6.1 shows the reflected shock pressure ratio achieved for each of the volume fractions considered in this study compared to the pressure ratio observed in experiments. The pressure ratio  $P/P_1$  is the ratio of the pressure behind the reflected shock and the pre-shock pressure.

1%	5%	10%	40% (Experiment)
12.3	15.1	17.3	18.1

Table 6.1: Comparison of the reflected shock pressure ratio at different volume fractions obtained from simulations and experiments (Theofanous et al., 2016).

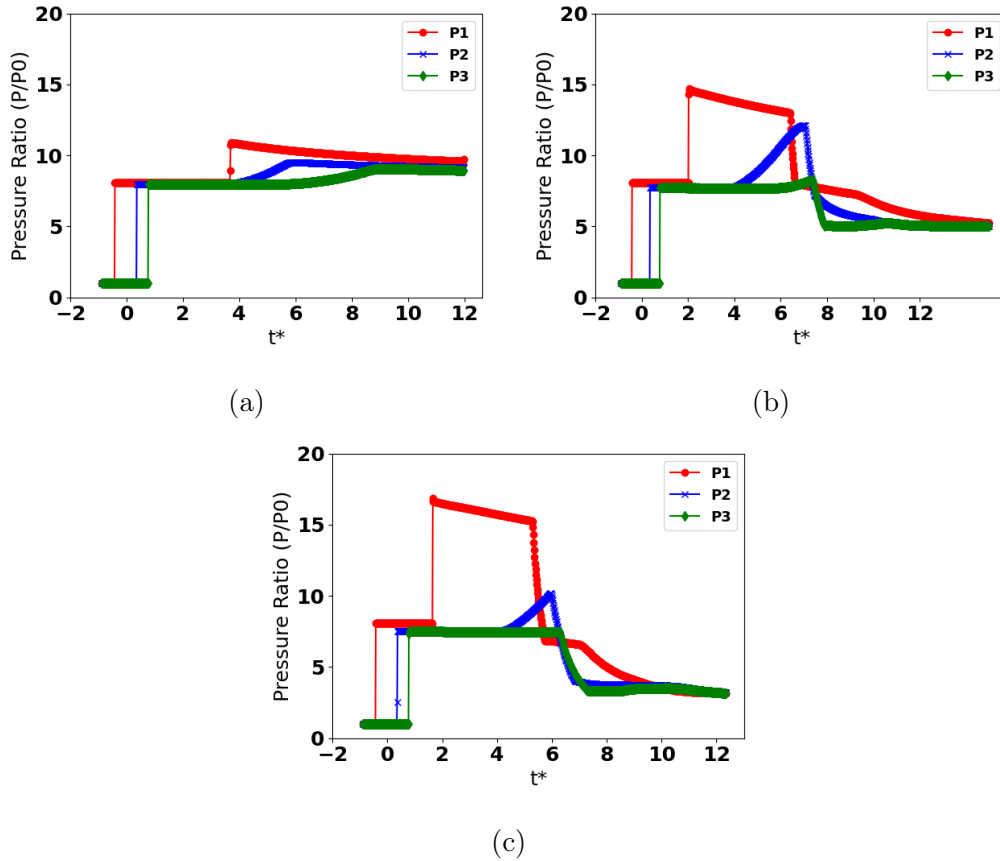


Figure 6.4: Pressure traces at volume fractions of a)  $\alpha_d = 1\%$  b)  $\alpha_d = 5\%$  c)  $\alpha_d = 10\%$ .

## 6.6 Computational Performance

Additional simulations were conducted for a variety of particle counts to compare the scaling and performance on both CPU and GPU architectures. To allow for the larger number of particles while maintaining volume fractions less than 10%, simulations were run with a larger curtain width of  $w_d = 0.5m$  and smaller particle diameters of  $D_d = 10\mu m$ . Simulations were run with particle counts ranging from  $1 \times 10^3$  to  $5 \times 10^7$ .

All simulations were run on the Chicoma cluster at Los Alamos National Labs.

Chapter 6. The FIESTA Particle Extension

Simulations were executed on a single node consisting of 128 CPU cores and four GPUs. The Kokkos framework allows the code to be executed unaltered on either the CPU cores or the GPU. For the simulations that targeted the CPU it was found that the particle simulations had the best performance when 64 CPU cores were used instead of the available 128 due to memory bandwidth limitations on the CPU. Therefore, all CPU results reported below were run using 64 cores. The GPU simulations were run on only one of the four GPUs available on the node because the current PPM/WENO implementation in FIESTApx does not support multiple GPUs.

Figure 6.5 depicts the ratio of computational time on the GPU versus CPU architectures defined as the GPU speedup:  $S = t_{CPU}/t_{GPU}$ , where  $t_{CPU}$  and  $t_{GPU}$  are the execution times for a particular total particle count. The figure shows that computations on the GPU architecture is 23 times faster than those on the CPU one for systems with 1,000 particles. For larger numbers of particles, up to  $5 \times 10^7$ , the simulations are still faster on the GPU architectures with a speedup of  $5\times$ .

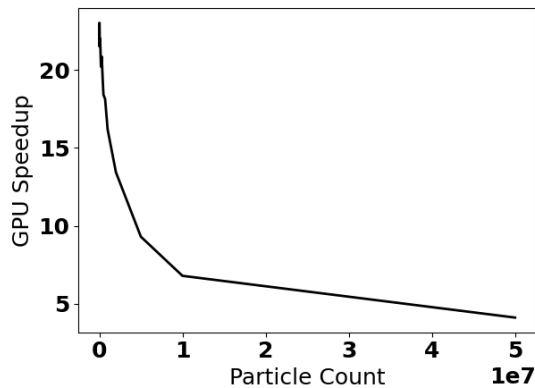


Figure 6.5: The GPU speedups for various particle counts.

The absolute execution time on each architecture is shown in figure 6.6. In each case it can be seen that the execution time increases linearly as a function of the particle count. The rate of increase in the execution time is smaller for the GPU

architecture to compare with that of the CPU one.

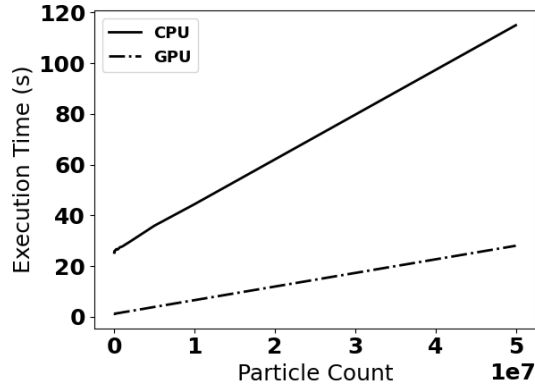


Figure 6.6: Execution time for CPU and GPU simulations vs. number of particles.

## 6.7 Conclusions

This chapter presents results of 3D simulations of the interaction between a planar shock and a finite-width curtain of solid particles. Results confirm the solver capability to reproduce realistic flow features observed in experiments (Theofanous et al., 2016) such as the growth of a shock accelerated particle curtain and the reflected shock strength. This is in spite of simulations being conducted with a lower initial volume fraction of particles than reported in the experiments.

Computational performance of the code on the GPU and CPU architectures was also compared. The code performance on the GPU architecture was found to be up to 23 times faster than on the CPU one for small numbers of particles and 5 times faster for large numbers of particles. The execution time scales linearly with particle count on both CPU and GPU architectures.

# Chapter 7

## Conclusions

A portable, GPU capable, compressible flow solver, FIESTA, was developed. Sample problems were conducted to demonstrate the capability of FIESTA to simulate different types of flows. FIESTA performance was demonstrated on various GPU devices, achieving speedups up to  $77\times$ . Computational performance the particle extension on GPU and CPU architectures was also compared. Simulations performed on GPU architecture demonstrated a  $23\times$  speedup for low volume fractions and a  $5\times$  speedup for the highest volume fractions tested. Execution time scaled linearly with particle count on both CPU and GPU architectures.

2D and 3D simulations were performed with FIESTA to compliment the experimental studies conducted by Olmstead et al. (2017b). Numerical results were successfully validated PLIF data from the experiments. Simulation results were also able to provide flow quantities not accessible in the experiments, namely velocity, vorticity and pressure fields. Vorticity fields for example, showed that the passage of a shock through an inclined gas curtain deposits oppositely signed vorticity on both sides of the gas curtain which leads to development of the Kelvin-Helmholtz instability (KHI) similar to that observed in the experiments.

## Chapter 7. Conclusions

There are notable differences between 2D and 3D simulations. In particular, changes to initial column angle did not have an effect on the SDKHI wavelength in 2D simulations but increasing initial angle increased SDKHI wavelength in 3D simulations. 3D simulations also more accurately reproduced column growth rates and post-shock angles when compared to the experiments. Additionally, flow features were prominent in 2D simulations which were not reported in experiments. Specifically, the gas curtain was seen spreading along the top boundary and an instability was observed near the column foot. Both these phenomena were observed in 3D simulations, but to a significantly lesser extent. This implies that 3D effects, in this case the counter-rotating vortex pair, are important for the development of such flows and must be accounted for in order to accurately reproduce experimental data.

However, 3D simulations are more computationally expensive than 2D simulations. The use of FIESTA on GPU architectures increases the accessibility of 3D simulations. The largest 3D simulations performed in this work used grids with over 100 billion computational cells and were performed in less than 10 hours on 256 GPUs.

FIESTA was also validated for shock-particle curtain interactions and accurately reproduced particle curtain growth rates and reflected shock strength when compared with experiments. The addition of Lagrangian transport capabilities represents an additional computational cost for the code. The ability to utilize GPU architectures resulted in improved computational times for particle laden flows as well.

# References

- G. Akiki, W. Moore, and S. Balachandar. Pairwise-interaction extended point-particle model for particle-laden flows. *Journal of Computational Physics*, 351:329–357, 2017.
- M. Anderson, P. Vorobieff, C. Truman, C. Corbin, G. Kuehner, P. Wayne, J. Conroy, R. White, and S. Kumar. An experimental and numerical study of shock interaction with a gas column seeded with droplets. *Shock Waves*, 25(2):107–125, 2015.
- G. Ball and R. East. Shock and blast attenuation by aqueous foam barriers: influences of barrier geometry. *Shock Waves*, 9(1):37–47, Feb. 1999. doi:10.1007/s001930050137.
- R. Bird, N. Tan, S. V. Luedtke, S. L. Harrell, M. Taufer, and B. Albright. Vpic 2.0: Next generation particle-in-cell simulations. *IEEE Transactions on Parallel and Distributed Systems*, 33(4):952–963, 2021.
- M. Bocchio, A. P. Jones, and J. D. Slavin. A re-evaluation of dust processing in supernova shock waves. *Astronomy & Astrophysics*, 570:A32, 2014.
- V. Boiko, V. Kiselev, S. Kiselev, A. Papyrin, S. Poplavsky, and V. Fomin. Shock wave interaction with a cloud of particles. *Shock Waves*, 7(5):275–285, 1997.

## REFERENCES

- A. Celani, M. Cencini, M. Vergassola, E. Villermaux, and D. Vincenzi. Shear effects on passive scalar spectra. *Journal of Fluid Mechanics*, 523:99–108, 2005. ISSN 1469-7645. doi: 10.1017/s0022112004002332.
- R. A. Chevalier, J. M. Blondin, and R. T. Emmering. Hydrodynamic instabilities in supernova remnants – Self-similar driven waves. *The Astrophysical Journal*, 392:118–130, 1992.
- E. J. Ching, S. R. Brill, M. Barnhardt, and M. Ihme. A two-way coupled euler-lagrange method for simulating multiphase flows with discontinuous galerkin schemes on arbitrary curved elements. *Journal of Computational Physics*, 405:109096, 3 2020. ISSN 00219991. doi: 10.1016/j.jcp.2019.109096.
- J. Dalton. Essay IV. On the expansion of elastic fluids by heat. *Mem. Proc. Manch. Lit. Philos. Soc.* 5, page 595–602, 1802.
- A. Dolatabadi, J. Mostaghimi, and V. Pershin. Modeling dense suspension of solid particles in highly compressible flows. *International Journal of Computational Fluid Dynamics*, 18:125–131, 2004. ISSN 1029-0257. doi: 10.1080/10618560310001634221.
- H. C. Edwards, C. R. Trott, and D. Sunderland. Kokkos: Enabling manycore performance portability through polymorphic memory access patterns. *Journal of Parallel and Distributed Computing*, 74(12):3202–3216, dec 2014. doi: 10.1016/j.jpdc.2014.07.003.
- A. Favre. Equations fondamentales des fluides à masse volumique variable en écoulements turbulents, 1976.
- M. Groom and B. Thornber. Direct numerical simulation of the multimode narrowband Richtmyer–Meshkov instability. *Computers & Fluids*, 194:104309, 2019. ISSN 0045-7930. doi: 10.1016/j.compfluid.2019.104309.

## REFERENCES

- A. Hadjadj and O. Sadot. Shock and blast waves mitigation. *Shock Waves*, 23, 2 2013. ISSN 0938-1287. doi: 10.1007/s00193-012-0429-0.
- M. Hahn, D. Drikakis, D. L. Youngs, and R. J. R. Williams. Richtmyer–meshkov turbulent mixing arising from an inclined material interface with realistic surface perturbations and reshocked flow. *Physics of Fluids*, 23(4):046101, Apr. 2011. doi: 10.1063/1.3576187.
- C. B. Henderson. Drag Coefficients of Spheres in Continuum and Rarefied Flows. *AIAA Journal*, 14(6):707–708, 1976. ISSN 0001-1452. doi: 10.2514/3.61409.
- M. Herrmann. A parallel Eulerian interface tracking/Lagrangian point particle multi-scale coupling procedure. *Journal of Computational Physics*, 229(3):745–759, 2010. ISSN 0021-9991. doi: 10.1016/j.jcp.2009.10.009.
- Y. Huang, H. Tang, J. Li, and C. Zhang. Studies of DDT enhancement approaches for kerosene-fueled small-scale pulse detonation engines applications. *Shock Waves*, 22(6):615–625, 2012.
- R. Ierusalimsky. *Programming in Lua, fourth edition*. Lua.org, 2016. ISBN 8590379868.
- G.-S. Jiang and C.-W. Shu. Efficient implementation of weighted ENO schemes. *Journal of Computational Physics*, 126(1):202–228, jun 1996. doi: 10.1006/jcph.1996.0130.
- J. Kane, R. Drake, and B. Remington. An evaluation of the Richtmyer-Meshkov instability in supernova remnant formation. *The Astrophysical Journal*, 511(1): 335, 1999.
- S. Koranne. Hierarchical data format 5: HDF5. In *Handbook of Open Source Tools*, pages 191–200. Springer, 2011.

## REFERENCES

- S. Kumar, G. Orlicz, C. Tomkins, C. Goodenough, K. Prestridge, P. Vorobieff, and R. Benjamin. Stretching of material lines in shock-accelerated gaseous flows. *Physics of Fluids*, 17(8):082107, 2005. doi: 10.1063/1.2031347.
- R. LeVeque, L. J, and D. Crighton. *Finite Volume Methods for Hyperbolic Problems*. Cambridge Texts in Applied Mathematics. Cambridge University Press, 2002. ISBN 9780521009249.
- J. D. Lindl, R. L. McCrory, and E. M. Campbell. Progress toward ignition and burn propagation in inertial confinement fusion. *Physics Today*, 45(9):32–40, sep 1992. doi: 10.1063/1.881318.
- L. Maddalena, F. Vergine, and M. Crisanti. Vortex dynamics studies in supersonic flow: Merging of co-rotating streamwise vortices. *Physics of Fluids*, 26(4):046101, apr 2014. doi: 10.1063/1.4871022.
- F. Marble, E. E. Zukoski, J. Jacobs, and G. Hendricks. Shock enhancement and control of hypersonic mixing and combustion. In *26th Joint Propulsion Conference*. American Institute of Aeronautics and Astronautics, jul 1990. doi: 10.2514/6.1990-1981.
- F. E. Marble, G. J. Hendricks, and E. E. Zukoski. Progress toward shock enhancement of supersonic combustion processes. In R. Borghi and S. N. B. Murthy, editors, *Turbulent Reactive Flows*, pages 932–950, New York, NY, 1989. Springer US. ISBN 978-1-4613-9631-4.
- F. J. W. A. Martins, J. Kirchmann, A. Kronenburg, and F. Beyrau. Quantification and mitigation of PIV bias errors caused by intermittent particle seeding and particle lag by means of large eddy simulations. *Measurement Science and Technology*, 32(10):104006, 2021. ISSN 0957-0233. doi: 10.1088/1361-6501/ac07d9.

## REFERENCES

- J. A. McFarland, J. A. Greenough, and D. Ranjan. Computational parametric study of a richtmyer-meshkov instability for an inclined interface. *Physical Review E - Statistical, Nonlinear, and Soft Matter Physics*, 84:026303, 8 2011. ISSN 15393755. doi: 10.1103/PhysRevE.84.026303.
- N. A. Mehta and D. A. Levin. Multiscale modeling of damaged surface topology in a hypersonic boundary. *The Journal of Chemical Physics*, 151, 9 2019. ISSN 0021-9606. doi: 10.1063/1.5117834.
- D. A. Mendis and M. Rosenberg. Cosmic dusty plasma. *Annual Review of Astronomy and Astrophysics*, 32(1):419–463, 1994.
- E. E. Meshkov. Instability of the interface of two gases accelerated by a shock wave. *Fluid Dynamics*, 4(5):101–104, 1972. doi: 10.1007/bf01015969.
- D. Olmstead, P. Wayne, D. Simons, I. T. Monje, J. H. Yoo, S. Kumar, C. R. Truman, and P. Vorobieff. Shock-driven transition to turbulence: Emergence of power-law scaling. *Physical Review Fluids*, 2(5):052601, 2017a.
- D. Olmstead, P. Wayne, J.-H. Yoo, S. Kumar, C. R. Truman, and P. Vorobieff. Experimental study of shock-accelerated inclined heavy gas cylinder. *Experiments in Fluids*, 58(6):71, May 2017b. ISSN 1432-1114. doi: 10.1007/s00348-017-2358-2.
- A. Palekar, P. Vorobieff, and C. R. Truman. Two-dimensional simulation of a shock-accelerated gas cylinder. *Progress in Computational Fluid Dynamics, An International Journal*, 7(8):427, 2007. doi: 10.1504/pcfd.2007.015775.
- J. Palmer and R. Hanson. PLIF measurements of temperature and velocity in a reacting supersonic free jet with OH. *32nd Aerospace Sciences Meeting and Exhibit*, 1994. doi: 10.2514/6.1994-618.
- S. J. Poovathingal and H. Chen. Modeling the damage process of dust particle

## REFERENCES

- impacts at microscale during high-speed entry. *AIAA AVIATION 2021 FORUM*, 8 2021. doi: 10.2514/6.2021-3146.
- R. Ramani, J. Reisner, and S. Shkoller. A space-time smooth artificial viscosity method with wavelet noise indicator and shock collision scheme, part 1: The 1-d case. *Journal of Computational Physics*, 387:81–116, June 2019a. doi: 10.1016/j.jcp.2019.02.049.
- R. Ramani, J. Reisner, and S. Shkoller. A space-time smooth artificial viscosity method with wavelet noise indicator and shock collision scheme, part 2: The 2-d case. *Journal of Computational Physics*, 387:45–80, June 2019b. doi: 10.1016/j.jcp.2019.02.048.
- R. Ramani, J. Reisner, and S. Shkoller. A space-time smooth artificial viscosity method with wavelet noise indicator and shock collision scheme, Part 2: The 2-D case. *Journal of Computational Physics*, 387:45–80, 2019c.
- A. M. Rasmus, C. A. D. Stefano, K. A. Flippo, F. W. Doss, C. F. Kawaguchi, J. L. Kline, E. C. Merritt, T. R. Desjardins, T. Cardenas, D. W. Schmidt, P. M. Donovan, F. Fierro, L. A. Goodwin, J. I. Martinez, T. E. Quintana, J. S. Zingale, and C. C. Kuranz. Shock-driven hydrodynamic instability of a sinusoidally perturbed, high-atwood number, oblique interface. *Physics of Plasmas*, 26:62103, 6 2019. ISSN 10897674. doi: 10.1063/1.5093650.
- R. D. Richtmyer. Taylor instability in shock acceleration of compressible fluids. *Communications on Pure and Applied Mathematics*, 13(2):297–319, may 1960. doi: 10.1002/cpa.3160130207.
- P. Rightley, P. Vorobieff, R. Martin, and R. Benjamin. Experimental observations of the mixing transition in a shock-accelerated gas curtain. *Physics of Fluids*, 11(1):186–200, 1999.

## REFERENCES

- B. Romero, S. Poroseva, P. Vorobieff, and J. Reisner. Simulations of the shock-driven kelvin-helmholtz instability in inclined gas curtains. *Physics of Fluids*, 33, 2021a. doi: 10.1063/5.0051459.
- B. E. Romero, S. Poroseva, P. Vorobieff, and J. Reisner. Shock driven Kelvin-Helmholtz instability. In *AIAA Scitech 2021 Forum*, page 0051, 2021b.
- O. Sen, N. Gaul, S. Davis, K. Choi, G. Jacobs, and H. Udaykumar. Role of pseudo-turbulent stresses in shocked particle clouds and construction of surrogate models for closure. *Shock Waves*, 28(3):579–597, 2018.
- D. W. Silvia, B. D. Smith, and J. M. Shull. Numerical simulations of supernova dust destruction. ii. metal-enriched ejecta knots. *The Astrophysical Journal*, 748(1):12, 2012.
- G. A. Sod. A survey of several finite difference methods for systems of nonlinear hyperbolic conservation laws. *Journal of Computational Physics*, 27(1):1–31, 1978. ISSN 0021-9991. doi: [https://doi.org/10.1016/0021-9991\(78\)90023-2](https://doi.org/10.1016/0021-9991(78)90023-2).
- K. R. Sreenivasan. The passive scalar spectrum and the Obukhov–Corrsin constant. *Physics of Fluids*, 8(1):189–196, 1996. ISSN 1070-6631. doi: 10.1063/1.868826.
- G. Stantchev, W. Dorland, and N. Gumerov. Fast parallel particle-to-grid interpolation for plasma pic simulations on the gpu. *Journal of Parallel and Distributed Computing*, 68(10):1339–1349, 2008.
- F. A. Tavarez and M. E. Plesha. Discrete element method for modelling solid and particulate materials. *International Journal for Numerical Methods in Engineering*, 70(4):379–404, 2007. ISSN 1097-0207. doi: 10.1002/nme.1881.
- T. G. Theofanous, V. Mitkin, and C. H. Chang. The dynamics of dense particle clouds subjected to shock waves. part 1. experiments and scaling laws. *Journal of Fluid Mechanics*, 792:658–681, 3 2016. ISSN 0022-1120. doi: 10.1017/JFM.2016.97.

## REFERENCES

- B. Thornber, M. Groom, and D. Youngs. A five-equation model for the simulation of miscible and viscous compressible fluids. *Journal of Computational Physics*, 372: 256–280, 2018. ISSN 0021-9991. doi: 10.1016/j.jcp.2018.06.028.
- C. Tomkins, K. Prestridge, P. Rightley, M. Marr-Lyon, P. Vorobieff, and R. Benjamin. A quantitative study of the interaction of two richtmyer–meshkov-unstable gas cylinders. *Physics of Fluids*, 15(4):986–1004, apr 2003. doi: 10.1063/1.1555802.
- V. K. Tritschler, B. J. Olson, S. K. Lele, S. Hickel, X. Y. Hu, and N. A. Adams. On the Richtmyer–Meshkov instability evolving from a deterministic multimode planar interface. *Journal of Fluid Mechanics*, 755:429–462, 2014. ISSN 0022-1120. doi: 10.1017/jfm.2014.436.
- E. Villermaux, C. Innocenti, and J. Duplat. Short circuits in the Corrsin–Obukhov cascade. *Physics of Fluids*, 13(1):284–289, 2001. ISSN 1070-6631. doi: 10.1063/1.1324006.
- P. Vorobieff, P. M. Rightley, and R. F. Benjamin. Power-law spectra of incipient gas-curtain turbulence. *Physical review letters*, 81(11):2240, 1998.
- P. Vorobieff, N.-G. Mohamed, C. Tomkins, C. Goodenough, M. Marr-Lyon, and R. F. Benjamin. Scaling evolution in shock-induced transition to turbulence. *Phys. Rev. E*, 68:065301, Dec 2003. doi: 10.1103/PhysRevE.68.065301.
- P. Vorobieff, C. Tomkins, S. Kumar, C. Goodenough, N. Mohamed, and R. Benjamin. Secondary instabilities in shock-induced transition to turbulence. In *Advances in Fluid Mechanics V (Advances in Fluid Mechanics)*, volume 45, page 10. WIT Press / Computational Mechanics, 2004. ISBN 1-85312-704-3.
- I. Waitz, F. Marble, and E. E. Zukoski. Vorticity generation by contoured wall injectors. In *28th Joint Propulsion Conference and Exhibit*. American Institute of Aeronautics and Astronautics, jul 1992. doi: 10.2514/6.1992-3550.

## REFERENCES

- P. Wayne, D. Olmstead, P. Vorobieff, C. Truman, and S. Kumar. Oblique shock interaction with a cylindrical density interface. *WIT Transactions on Engineering Sciences*, 89:161–169, 2015.
- P. Wayne, S. Cooper, D. Simons, I. Trueba-Monje, D. Freelong, G. Vigil, P. Vorobieff, C. R. Truman, V. Vorob’ev, and T. Clark. Dalton’s and Amagat’s laws fail in gas mixtures with shock propagation. *Science Advances*, 5(12):eaax4749, 2019.
- C. White, H. Silva III, and P. Vorobieff. Investigation of Mixing Law Efficacy for Gaseous Hydrodynamic Simulations. *Journal of Thermophysics and Heat Transfer*, pages 1–6, 2020.
- J. Williamson. Low-storage runge-kutta schemes. *Journal of Computational Physics*, 35(1):48–56, mar 1980. doi: 10.1016/0021-9991(80)90033-9.
- P. Woitke. 2D models for dust-driven AGB star winds. *Astronomy & Astrophysics*, 452(2):537–549, 2006.
- M. L. Wong, D. Livescu, and S. K. Lele. High-resolution Navier-Stokes simulations of Richtmyer-Meshkov instability with reshock. *Physical Review Fluids*, 4(10):104609, 2019. doi: 10.1103/physrevfluids.4.104609.
- A. Woods, S. Bower, and M. Bursik. Models of explosive volcanic eruptions. *Non-linear processes in Geophys*, 2(3):269 – 279, 1996.
- J. Yang, T. Kubota, and E. E. Zukoski. Applications of shock-induced mixing to supersonic combustion. *AIAA Journal*, 31(5):854–862, may 1993. doi: 10.2514/3.11696.
- J. Yang, T. Kubota, and E. E. Zukoski. A model for characterization of a vortex pair formed by shock passage over a light-gas inhomogeneity. *Journal of Fluid Mechanics*, 258:217–244, jan 1994. doi: 10.1017/s0022112094003307.

## REFERENCES

- Q. Yang, J. Chang, and W. Bao. Richtmyer-meshkov instability induced mixing enhancement in the scramjet combustor with a central strut. *Advances in Mechanical Engineering*, 6:614189, jan 2014. doi: 10.1155/2014/614189.
- B. Yu, M. He, B. Zhang, and H. Liu. Two-stage growth mode for lift-off mechanism in oblique shock-wave/jet interaction. *Physics of Fluids*, 32(11):116105, Nov. 2020. doi: 10.1063/5.0022449.
- Z. Zhai, P. Dong, T. Si, and X. Luo. The richtmyer-meshkov instability of a "v" shaped air/helium interface subjected to a weak shock. *Physics of Fluids*, 28:82104, 8 2016. ISSN 10897666. doi: 10.1063/1.4961038.
- Y. Zhou. Rayleigh-Taylor and Richtmyer-Meshkov instability induced flow, turbulence, and mixing. I. *Physics Reports*, 720-722:1–136, 2017a.
- Y. Zhou. Rayleigh-Taylor and Richtmyer-Meshkov instability induced flow, turbulence, and mixing. II. *Physics Reports*, 723-725:1–160, 2017b.
- Y. Zhou, T. T. Clark, D. S. Clark, S. G. Glendinning, M. A. Skinner, C. M. Huntington, O. A. Hurricane, A. M. Dimits, and B. A. Remington. Turbulent mixing and transition criteria of flows induced by hydrodynamic instabilities. *Physics of Plasmas*, 26(8):080901, aug 2019. doi: 10.1063/1.5088745.